PHASE TRANSITIONS OF EARLY TRANSITION METAL OXIDES AND IMPLICATIONS FOR FUNCTIONAL THIN FILMS

A Dissertation

by

NATHAN ANDREW FLEER

Submitted to the Office of Graduate and Professional Studies of
Texas A&M University
in partial fulfillment of the requirements for the degree of

DOCTOR OF PHILOSOPHY

Chair of Committee,	Sarbajit Banerjee
Committee Members,	David E. Bergbreiter
	Lei Fang
	Terry S. Creasy
Head of Department,	Simon North

August 2019

Major Subject: Chemistry

Copyright 2019 Nathan Andrew Fleer

ABSTRACT

Solid-to-solid phase transitions induced by external stimuli underpin numerous technological applications and enable the stabilization of metastable polymorphs characterized by atomic connectivities and electronic structure distinct from that of the thermodynamic phase. Some strategies to stabilize metastable polymorphs include size reduction (such that surface energy preferences overcome bulk free energy differences), topochemical modification, application of high pressure, or interfacial strain. The primary focus of this work is on controlling solid-to-solid phase transitions to leverage the benefits afforded by stabilizing these metastable phases.

Utilization of the insulator-to-metal transition in VO_2 for use in thermochromic fenestration will be examined in detail. Briefly, nanocomposite thin films have been prepared containing VO_2 nanocrystals embedded within methacrylic acid-ethyl acrylate copolymer matrices. Control over particle size, refractive index matching, and surface monolayer/surfactant mediated dispersion allows for mitigation of internal scattering mechanisms that negatively impact visible light transmittance and degrade the magnitude of near-infrared modulation. An unprecedented combination of visible light transmittance and solar heat gain modulation is demonstrated for hydrothermally prepared nanocrystals with a size of 44±30 nm encapsulated with a 5 nm thick SiO_2 shell and dispersed within a methacrylic acid-ethyl acrylate copolymer matrix at a loading of 0.6 mg/mL.

Another noteworthy phase transition, cubic HfO_2, a material that is only stable at temperatures >2600°C, can be stabilized as a result of outwards oxygen diffusion and epitaxial matching within core—shell VO_2@HfO_2 structures when annealed at 650°C under an Ar

ambient. The VO_2 is reduced to rhombohedral V_2O_3, which templates the nucleation of cubic HfO_2 as a result of a crystallographic epitaxial relationship that facilitates nucleation of this metastable polymorph over that of the thermodynamically stable monoclinic phase. Free-standing cubic HfO_2 has been stabilized by acid dissolution of the V_2O_3 core. The process to embed these particles in nanocomposite thin films for gate dielectric applications will also be examined. The synthesis of the negative thermal expansion material, cubic HfV_2O_7, through an interdiffusion reaction between VO_2@HfO_2 precursors arranged in a core—shell configuration and ball-milling of HfO_2 and ultrasmall VO_2 in a 1:2 ratio will also be discussed as annealing the solid mixture in air at 600°C yields phase-pure, cubic HfV_2O_7.

DEDICATION

This dissertation is dedicated to my parents and siblings whose love and encouragement kept me going every step of the way. To past advisors, Dr. Jennifer Jamison, Dr. Davis Pritchett, and Dr. David McGinnis, who encouraged me to begin this Ph.D. journey and offered guidance many times. I also thank all other family members and the friends I have made along the way.

ACKNOWLEDGEMENTS

I would like to thank my advisor, Prof. Sarbajit Banerjee. His Patience, guidance, mentorship, and enthusiasm directed me toward success and has instilled in me the motivation and integrity towards science and fostered strong work relationships between group members. He has given me a passion for knowledge and understanding that I will no doubt employ throughout all aspects of life. Without his support, I would not have been successful in my Ph.D. graduate career.

I would like to thank my committee members, Prof. David E. Bergbreiter, Prof. Lei Fang, and Prof. Terry S. Creasy for their guidance and support throughout my graduate career. I also thank Dr. Diane G. Sellers, Dr. Wilson Serem, and Dr. Stanislav V. Verkhoturov for their support and analytical advice in many of my manuscripts.

Special thanks to all of the current and previous Banerjee group members for their support and guidance toward success in my graduate career.

Thanks also go to my friends and colleagues and the department faculty and staff for making my time at Texas A&M University a great experience.

CONTRIBUTORS AND FUNDING SOURCES

Contributors

This work was supervised by a dissertation committee consisting of Professor Sarbajit Banerjee (advisor), Professor David E. Bergbreiter, and Professor Lei Fang of the Department of Chemistry and Terry S. Creasy of the Department of Materials Science and Engineering.

Much of the characterization and data in this dissertation is obtained using instruments in the Materials and Characterization Facilities (MCF) for Scanning Electron Microscopy, Atomic Force Microscopy, Energy Dispersive X-ray Spectroscopy (EDX), and Nanoindentation. The Microscopy and Imaging Center (MIC) and Oak Ridge National Laboratory (ORNL) provided instrumentation for Transmission Electron Microscopy.

Nanoindentation characterization in Chapter III was performed by Dr. Wilson Serem. Chapter IV EDX and TEM was performed partly by Melonie Thomas at Oak Ridge National Lab. HfO_2 film composition analysis in Chapter VI was performed by Dr. Stanislav V. Verkhoturov. Refinements in Chapter IV were conducted by Justin Andrews and refinements in Chapter V were performed by Joseph Handy. Raman peak fitting in Chapter V was performed by Diane G. Sellers.

All other work conducted for the dissertation was completed by the student independently.

Funding Sources

This work was made possible in part by Cenovus Energy, Sherwin Williams, Konica Minolta, Vanitec, and Quanex Building Products.

TABLE OF CONTENTS

LIST OF FIGURES

Page

LIST OF TABLES

Page

CHAPTER I

INTRODUCTION AND MOTIVATION

I.1 Thermochromic Nanocomposite Thin Films Underpinned by Metal—Insulator Transitions of Embedded VO_2 Nanocrystals

With increasing global urbanization, the energy consumed by buildings continues to rise at an alarming pace.[1–3] Much of this energy is consumed for temperature control, specifically, heating and cooling of these structures, which in turn is inextricably linked to lighting of interiors. Indeed, the United Nations recently published a report detailing the global use of energy and a staggering 20—40% of global energy consumption can be attributed to buildings.[1,3,4] According to an estimate from the Department of Energy, the United States expends roughly 41% of its yearly energy consumption on buildings.[3–6] Consequently, curbing the energy consumption of buildings has emerged as an urgent global imperative.[1–3,5,6] The consequences of such burgeoning energy consumption extend beyond a monetary level and have serious implications for the environment given CO_2 emissions associated with increased energy consumption.[2,7] The energy footprint of buildings is largely determined by the building envelope, the boundary between the building and the environment, and more specifically, the fenestration elements, doors, windows, and glazed skylights through which solar irradiance enters the building and introduces solar heat gain.[8–10] Efforts to control solar heat gain often rely on static silver coatings or electrochromic materials; the former encountering issues with visible light transmission and the "always on" concern that results in the reflection of the NIR spectrum in the winter when solar heat gain is desirable. In contrast, the latter requires energy expenditure to save energy and further necessitates considerable capital investments while retrofitting

buildings.[11–13] A major drawback shared amongst these solar control technologies is the reduction of visible light transmittance through said films, which inevitably results in a significant reduction in ambient lighting. One solution to this problem is an intelligent dynamically switchable coating underpinned by an electronic or structural phase transition. One such transition is observed in the binary vanadium oxide, VO_2. VO_2 is characterized by a small band gap of 0.6 eV in its insulating phase, which upon heating, is closed to yield a correlated metal; the high-temperature phase of VO_2 is metallic, resulting in the selective suppression of near-infrared (NIR) transmittance as a function of temperature.[3,14–16] This signature transition occurs at ca. 67°C, in closer proximity to room temperature than analogous transitions, and can be lowered through the incorporation of dopants.[17–21] As a result, VO_2 shows potential to alleviate many of these drawbacks in that it responds dynamically to changes in temperature by rapidly switching to a metallic phase that blocks NIR transmittance under high ambient temperatures. The utilization of VO_2 within thermochromic glazing requires the design of nanocomposite thin films that are readily retrofittable onto existing buildings, can be prepared through scalable manufacturing processes, and show high visible light transmittance.[3,4,22–27] Much of the difficulties with the practical utilization of VO_2 arises from its lack of robustness in thin films and the tendency of oxide films to crack under repeated thermal cycling; however, preparation of nanometer-sized particles, as accessible from hydrothermal methods, alleviates the stresses associated with thermal cycling and considerably overcomes this challenge.[14,28] Additional challenges stem from the need to have well-dispersed ultrasmall nanocrystals with excellent dispersion with a continuous polymeric medium such as to mitigate light scattering.

Three main parameters must be considered when developing dynamic window films: (i) the degree of NIR suppression; (ii) the onset of NIR modulation (which) must be early in the

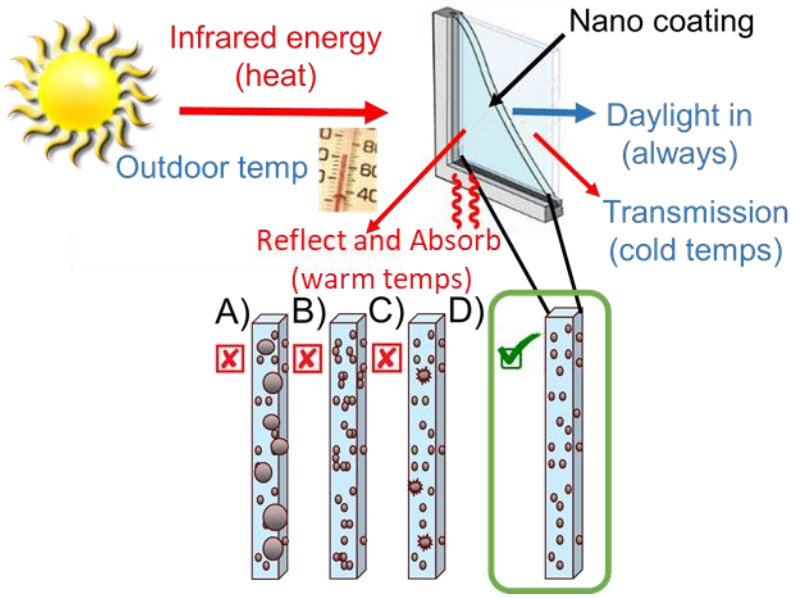

Figure I. 1 Designing the optimal VO_2 nanocomposite glazing. **A)** Large particles scatter light (Mie scattering) and reduce visible light transmittance. **B)** Agglomeration of small particles behaves in much the same way as large particles in A, and thus dispersion of individual particles is necessary. **C)** Small particles are desirable, but over-milling degrades crystal quality. **D)** The ideal case involves small (<50 nm based on optical simulations), individually dispersed particles embedded within a low dielectric constant medium.

solar spectrum to maximize the extent of reflected NIR solar irradiance, but not so early as to introduce visible coloration); and (iii) visible light transmittance (luminous transmittance, which must be maximized). **Figure I. 1** schematically illustrates the challenges associated with the embedding of VO_2 nanoparticles within composite films regarding the three aforementioned metrics. Briefly, large particles cause scattering of light (Mie scattering) and reduce visible light transmittance. Such a scattering background also shifts the onset of NIR suppression further into the NIR region of the electromagnetic spectrum. A top-down milling approach can be used to reduce particle size, but damages the crystallinity of the material, thereby degrading the magnitude of the transition and its efficacy.[3,4] A bottom-up approach we have designed utilizing a more soluble precursor, NH_4VO_3, yields small single crystalline particles, but if these particles

are poorly dispersed, they suffer the same shortcomings of larger particles with regards to agglomeration.[3,4] In Chapters II and III, we outline the synthesis of hybrid nanocomposites wherein VO_2 nanoparticles of optimal dimensions (<50 nm diameter as determined from previous finite element analysis and geometrical optical simulations) are dispersed within a refractive-index-matched transparent medium such as to mitigate Mie scattering, facilitate maximal visible light transmittance, and provide an early onset of NIR suppression to maximize energy efficiency.[3,4,29]

I.2 Stabilization of Metastable Phases of HfO_2 and a Synthetic Route to HfV_2O_7

SiO_2 is ubiquitously used as a gate dielectric material in field-effect transistors (FETs); however, its limitations have led to an extensive search for new dielectrics and indeed amorphous HfO_2 has been widely implemented.[30] With the constant scaling of devices as per Moore's law, the inherent problems with SiO_2 have assumed particular importance.[31–34]

$$C = \frac{\varepsilon_r A}{t} \qquad \textbf{(I. 1)}$$

Equation I. 1 defines capacitance for a dielectric material where ε_r is the dielectric constant, A is the area, and t is the thickness of said material. The thickness of the dielectric layer within a FET is generally manipulated to manage capacitance due to downscaling of device sizes; however, this results in current leakage when scaled to a thickness of below ca. 2 nm.[34–36] For example, the thinning of a SiO_2 gate dielectric (SiO_2 having a dielectric constant of ca. 3.5) in a FET from a thickness of ca. 35 Å to ca. 15 Å at a gate bias of ca. 1 V results in an increase of leakage current from 1×10^{-12} A/cm^2 to 1×10 A/cm^2.[34,37–39] In other words, a twelve orders of magnitude current

leakage is induced for a mere factor of two reduction in thickness, which effectively negates any increase in capacitance.[34] Furthermore, SiO_2 is subject to silicidation and silicate formation at high temperatures, which strongly degrades the performance of the FET.[36,40] Consequently, there is an urgent need for a material that is less chemically reactive and less susceptible to oxide breakdown if FETs are to keep pace with device scaling.[40–42]

An alternative approach for achieving greater capacitance or maintaining a constant capacitance with decreasing area is adjusting the dielectric constant in accordance with Eq. I. 1.[35,36] Amorphous HfO_2 has already started to be used as a replacement for SiO_2 in electronic devices, such as the aforementioned gate dielectrics in FETs, for the following reasons: (i) high melting point (2758°C), (ii) high dielectric constant (up to 70), (iii) wide band gap (up to 6.11 eV), and (iv) resistance to silicidation.[30,31,36,39,40,43] HfO_2 remains crystalline up to 2758°C before melting, as compared to 1713°C for SiO_2.[30,44] Bulk hafnia crystallizes in a low-symmetry monoclinic unit cell (M, space group $P2_1/c$) with seven-coordinated Hf centers and exhibits a transition to an eight-coordinated high-symmetry, tetragonal phase (R, space group $P4_2/nmc$) upon reaching ca. 1720°C.[36,45] The still higher symmetry cubic phase (C, space group $Fm\bar{3}m$) of HfO_2 is stabilized at temperatures of 2600°C or higher.[32,45–47] An alternative phase diagram with the respective crystal structures can be constructed using pressure as a third axis in **Figure I. 2** with the diagram reprinted and adapted from Shin et al. with permission from Elsevier.[48–50] The orthorhombic distortion, orthorhombic I (O1, space group $Pca2_1$) exists in the pressure range from 4.3 GPa—14.5 GPa; at still higher pressures, the orthorhombic II (O2, space group $Pmn2_1$) phase of HfO_2 is observed.[32,51] These phase changes are all diffusionless Martensitic transitions and result from displacive unit cell distortions.[45,52,53]

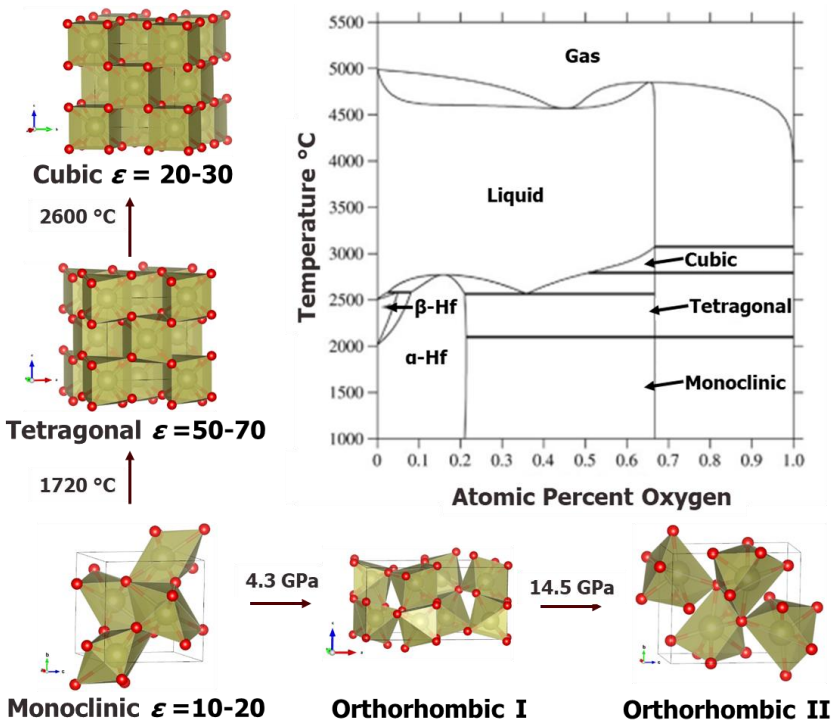

Figure I. 2 Phase diagram of HfO_2 polymorphs and accompanying dielectric constants (ε) where available. The tetragonal and cubic dielectric constants noted here are estimates from first-principles calculations.[30,31,32,36,45,50] Phase diagram component reprinted and adapted from ref. 50 Calphad, **30**, Shin, D; Arróyave, R.; Liu, Z. Thermodynamic modeling of the Hf-Si-O system, 375-386, Copyright 2006, with permission from Elsevier.

A value of ca. 18 is the generally accepted dielectric constant of monoclinic HfO_2, which is higher than that of SiO_2; however, the dielectric constants of the tetragonal and cubic polymorphs, which are predicted to be as high as 70 and 30, respectively, are far more desirable for technological applications.[30,36,45] Soft, low-energy phonon modes in the Hf—O bonds of HfO_2 and a high Born effective charge tensor give rise to the high ε_r values observed for these HfO_2 polymorphs.[30,45] The higher coordination number of the Hf centers of the high-temperature tetragonal and cubic phases of HfO_2 results in the weakening of the Hf—O bond strength, which allows for them to be more readily polarized; the more facile polarization is manifested in a higher dielectric constant.[49] The already substantial band gap of HfO_2 also increases from ca.

5.78 to ca. 6.11 eV upon transitioning from the monoclinic to tetragonal phase, thereby reducing the leakage current when the material is used as a dielectric.[36,54] The cubic, orthorhombic I, and orthorhombic II phases have thus far been impossible to access without substantial doping, and the dielectric properties of these compounds remain largely underexplored. Notably, these two metastable variants have been shown to exhibit ferroelectric behavior when stabilized under ambient conditions through doping (e.g., Si-doped HfO_2); the observed ferroelectric behavior is desirable for applications such as transpolarizers and capacitors.[47,55,56] The measured ferroelectric properties are attributed to the non-centrosymmetric structure of these metastable phases, which results in spontaneous polarization of orthorhombic HfO_2.[47,55] The dielectric and ferroelectric properties afforded by the metastable phases of HfO_2 are noticeably superior to SiO_2 and even superior in many regards to the properties of thermodynamically stable monoclinic HfO_2; however, as explained above, these metastable phases remain largely inaccessible without considerable incorporation of dopants.[36,45,51,57] Chapters III explores the stabilization of cubic HfO_2, a metastable polymorph of HfO_2 that has hitherto been inaccessible without extensive doping. **Figure I. 3** is reprinted from Parija et al. with permission from the American Chemical Society and illustrates the similarities in energy landscape and exemplifies why these phases are difficult to stabilize in the absence of dopants.[58]

HfO_2 and ZrO_2 show close parallels in terms of their physical and chemical properties and thus the more extensively explored phase space of the latter provides insight into the stabilization of metastable polymorphs of the former.[30,32,45,55] The similarities between compounds of hafnium and zirconium can be traced in considerable measure to the lanthanide co ntraction phenomenon (from cerium to lutetium), which stems from electrons filling the poor shielding, inner 4*f* shell of these elements prior to outer shells.[30,59–61] The ionic radii of Zr^{4+},

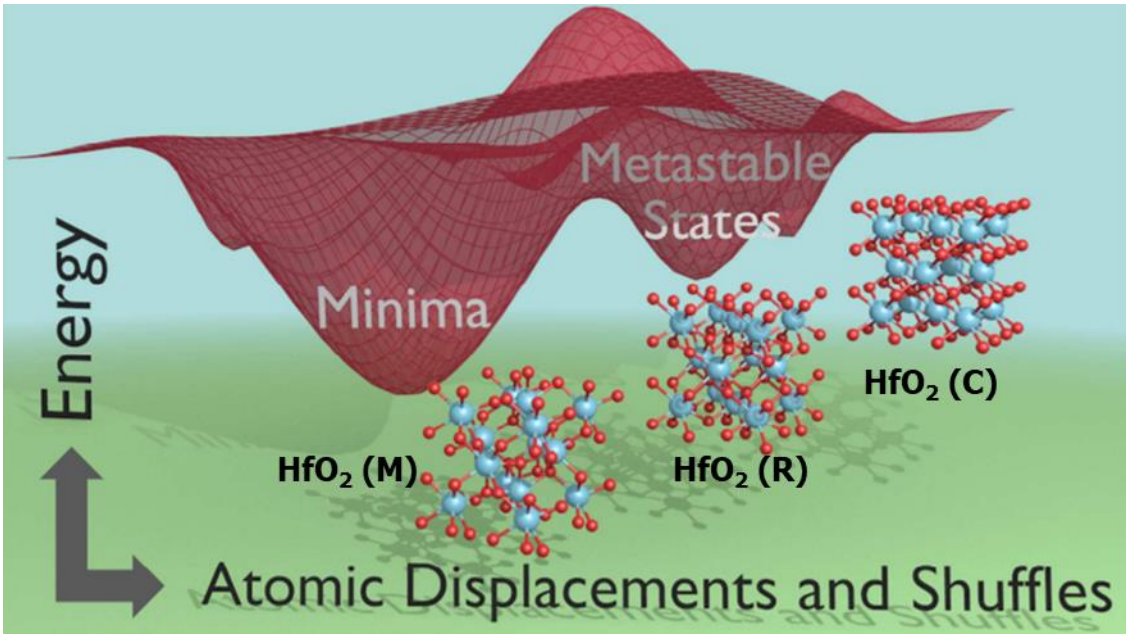

Figure I. 3 Illustration of the energy landscape of HfO_2 showing energy wells and the phase that is thermodynamically stable at each local minima. The overall minima sees the HfO_2 (M) phase as the most thermodynamically favorable phase whereas temperatures of 1720°C and 2600°C are required to reach the HfO_2 (R) and HfO_2 (C) local minima respectively. Figure reprinted with permission from ref. 58 "Parija, A.; Waetzig, G. R.; Andrews, J. L.; Banerjee, S. Traversing Energy Landscapes Away from Equilibrium: Strategies for Accessing and Utilizing Metastable Phase Space. J. Phys. Chem. C 2018, **122**, 25709–25728." Copyright 2018 American Chemical Society.

element 40, is 79 pm and Hf^{4+}, element 72, is 78 pm.[30,59,60] ZrO_2 and HfO_2 crystal systems also show similar lattice parameters for each phase, both exhibit Martensitic transitions, and each phase transition occurs with considerable homology in the sequence of crystal structures adopted with increasing temperature.[45,47,55] Despite these similarities in physical and chemical properties, the temperature ranges at which phase transitions are observed are starkly different in the two compounds, reflecting strongly altered energy barriers between different phases.[36,45,62,63] Bulk ZrO_2 transitions from monoclinic to tetragonal ZrO_2 at temperatures above 1170°C, much lower than the 1720°C transition temperature of HfO_2; tetragonal ZrO_2 transitions to cubic ZrO_2 above 2370°C, which is lower than the 2600°C transition temperature of tetragonal HfO_2.[36,45,46,48,57,63]

The differences stem from several different origins. First, the monoclinic phase of HfO_2 is favored over the tetragonal phase by a bulk free energy of 196 meV, whereas the monoclinic phase of ZrO_2 is only favored by a bulk free energy of 140 meV.[36,46,64] Next, the Zr—O bond length is longer than the equivalent Hf—O bond and it has been proposed that the extent of M—O bond distortion is lower for ZrO_2 as compared to HfO_2 during the monoclinic to tetragonal transition.[45,63–65] Finally, there is a volume increase that accompanies the return transition from tetragonal to monoclinic when these metal oxides are cooled.[36,45,64,66] The volume increase for ZrO_2 is much larger at 4.0% than the 2.7% value for HfO_2, and thus the tetragonal to monoclinic transition is more energetically favorable for HfO_2 and considerable superheating is required to trap tetragonal HfO_2 and prevent the return transition.[36,45,64,66] The tetragonal and monoclinic unit cells are distinguished by only a 9° shear distortion, which further allows both ZrO_2 and HfO_2 to readily revert to the monoclinic polymorph upon cooling and further compounds the difficulties with stabilizing metastable HfO_2 phases.[45,52]

One method to stabilize metastable phases relies on using size confinement to overcome bulk free energy terms with surface free energy terms.[36,53,62,63,67,68] The ceramics industry currently uses this method to stabilize tetragonal ZrO_2 at a critical size <30 nm; the transformation of tetragonal ZrO_2 to monoclinic ZrO_2 provides an effective means of energy dissipation as shown in **Equation I. 2**.[36,46,53,62,63,67,68]

$$\Delta G_{t\rightarrow m} = \Delta G_{\text{bulk}} + \Delta U_{\text{matrix}} + \Delta U_{\text{surface}} + \Delta U_{\text{interfaces}} \qquad \textbf{(I. 2)}$$

ΔG_{bulk} is the free energy difference between tetragonal and monoclinic phases.[36,45,46] The bulk free energy of monoclinic is strongly negative and encourages stabilization of the monoclinic

phase.[36,45,46] ΔU_{matrix} is the elastic strain of the transition and is positive in value as energy is required to complete the transition. $\Delta U_{surface}$ is the change in surface energy and $\Delta U_{interfaces}$ is the energy required to produce new interfaces.[36,45,46] The bulk energy favors monoclinic ZrO_2 by -140 meV and can be counted with an increase in the $\Delta U_{surface}$ parameter by increasing the surface area to volume ratio of particles.[36,45,46]

Several calculations suggest have suggested a critical size of 2—10 nm for stabilization of tetragonal HfO_2 owing to the thermodynamic differences from ZrO_2 described above.[36,46,64] Past work in our research group has led to the development of a non-hydrolytic sol—gel condensation approach for the synthesis of HfO_2 nanocrystals based on the condensation of hafnium(IV) *tert*-butoxide ($Hf(O^tBu)_4$) with $HfCl_4$. The addition of monomers, such as

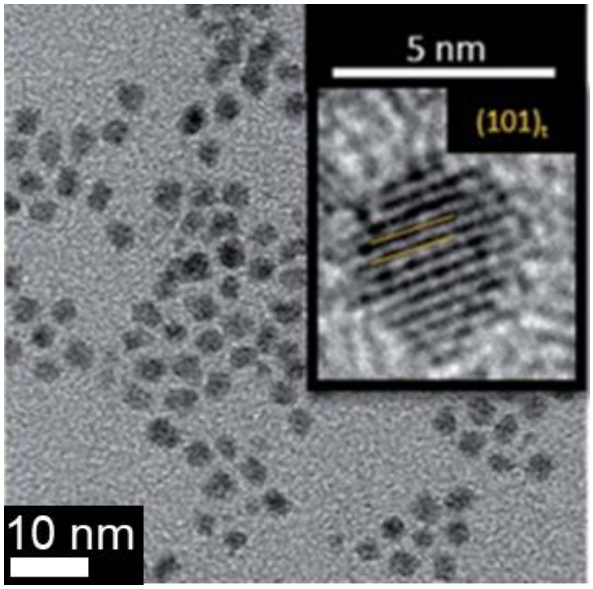

Figure I. 4 Size confinement stabilizes the metastable tetragonal phase of hafnia. Particles shown here are comprised of 97.64 at.% Hf and 2.36 at.% Ce as they were synthesized with 2.0:2.0 mmol of $HfCl_4$:$Ce(O^tBut)_4$ to slow the reaction and obtain 3.1±0.4 nm size particles. Figure reprinted with permission from ref. 36 "Waetzig, G. R.; Depner, S. W.; Asayesh-Ardakani, H., Cultrara, N. D.; Shahbazian-Yassar, R.; Banerjee, S. Stabilizing metastable tetragonal HfO_2 using a non-hydrolytic solution-phase route: ligand exchange as a means of controlling particle size *Chem. Sci.*, 2016, **7**, 4930" Published by The Royal Society of Chemistry.

cerium(IV) *tert*-butoxide and lanthanum(III) isopropoxide retards the condensation rate and enables precise control of nanocrystal size, yielding HfO_2 nanocrystals with dimensions <10 nm.[36] A critical size in the range of 3.6—3.8 nm has been determined as the threshold size for stabilization of tetragonal HfO_2, as illustrated in **Figure I. 4** which has been reprinted from Waetzig et al. from *Chemical Science* published by the Royal Society of Chemistry.[36]

Our group has further demonstrated that strain energy at twinning domains facilitates nucleation of the transition from the monoclinic to tetragonal phase of HfO_2 because the energy at these twin interfaces allows the transition to overcome the 9° lattice cell distortion between the two phases more easily.[45,52] While these synthetic schemes have successfully allowed for stabilization of tetragonal HfO_2, synthesis of the cubic polymorph has been much more challenging. Cubic HfO_2 has been stabilized by incorporation of 8.0 at.% La and exhibits a dielectric constant of 38.[57] This value exceeds the predicted dielectric constant of cubic hafnia and further makes cubic HfO_2 an attractive synthetic target.[30,36,45] Chapters III and IV of this dissertation outline a method to exploit epitaxial relationships between HfO_2 and V_2O_3 (derived from oxygen diffusion away from VO_2(M1)) to minimize the extent of vanadium doping required to stabilize the high-temperature cubic phase of HfO_2 under ambient conditions. Chapter IV further outlines a method for the preparation of dielectric films based on embedding HfO_2 nanocrystals within poly(furfuryl alcohol) matrices.[36,45,69]

VO_2@HfO_2 core—shell structures have the potential to provide a direct solid-state synthetic route to HfV_2O_7, a well-known, yet somewhat difficult to synthesize, negative thermal expansion (NTE) material.[70–72] NTE materials show great potential for deployment in industry as an additive due to their ability to contract when heated, rather than expand as is typical of most materials. Consequently, embedding NTE materials within matrices exhibiting positive thermal

expansion can yield net zero thermal expansion properties.[70–72] NTE materials are especially relevant in electronics, roads, cement, glassware, and many more structural materials.[70–72] MX_2O_7 materials are especially desirable because they exhibit isotropic negative expansion owing to their distinctive bonding motifs and cubic unit cell.[70–72] Isotropic behavior in NTE materials makes them even more useful as they do not suffer damage from microcracking under repeated thermal cycling as is a rampant problem in anisotropic NTE materials.[70] The realization of these materials as an additive at industrial scales has been hampered by the absence of scalable manufacturing processes.[70,71,73] Chapter VI of this dissertation will outline a solid-state synthetic route utilizing VO_2@HfO_2 core—shell nanocrystals to provide a low-temperature, low-pressure, scalable route to synthesize the MX_2O_7 family of materials.

I.3 References

(1) Houvila, P. *UNEP. Buildings and Climate Change: Status, Challenges, and Opportunities*; UNEP/EarthPrint, 2007.

(2) UNEP. Buildings and Climate Change: Summary for Decision Makers. *Program. Sustain. Build. Clim.* 2009,1−62.

(3) Fleer, N. A.; Pelcher, K. E.; Zou, J.; Nieto, K.; Douglas, L. D.; Sellers, D. G.; Banerjee, S. Hybrid Nanocomposite Films Comprising Dispersed VO_2 Nanocrystals: A Scalable Aqueous-Phase Route to Thermochromic Fenestration. *ACS Appl. Mater. Interfaces* **2017**, *9*, 38887–38900.

(4) Fleer, N. A.; Pelcher, K. E.; Nieto, K.; Braham, E. J.; Zou, J.; Horrocks, G. A.; Naoi, Y.; Depner, S. W.; Schultz, B. J.; Amano, J.; Sellers, D. G.; Banerjee, S. Elucidating the Crystallite Size Dependence of the Thermochromic Properties of Nanocomposite VO_2

Thin Films. *ACS Omega* **2018**, *3*, 14280–14293.

(5) Risser, R. *Making Smart Windows Smarter*. U.S. Department of Energy: Washington, DC **2011**.

(6) Omer, A. M. Energy, Environment and Sustainable Development. *Renew. Sustain. Energy Rev.* **2008**, *12*, 2265–2300.

(7) U.S. Department of Energy. *Energy Efficiency Trends in Residential and Commercial Buildings*; U.S. DOE: Washington, DC, **2010**, pp 1–52.

(8) Kanu, S. S.; Binions, R. Thin Films for Solar Control Applications. *Proc. R. Soc. A Math. Phys. Eng. Sci.* **2010**, *466*, 19–44.

(9) Wang, Y.; Runnerstom, E. L.; Milliron, D. J. Switchable Materials for Smart Windows. *Annu. Rev. Chem. Biomol. Eng.* **2016**, *7*, 283–304.

(10) Manning, T. D.; Parkin, I. P.; Pemble, M. E.; Sheel, D.; Vernardou, D. Intelligent Window Coatings: Atmospheric Pressure Chemical Vapor Deposition of Tungsten-Doped Vanadium Dioxide. *Chem. Mater.* **2004**, *16*, 744–749.

(11) Granqvist, C. G. Electrochromic Materials: Out of a Niche. *Nat. Mater.* **2006**, *5*, 89–90.

(12) Barile, C. J.; Slotcavage, D. J.; McGehee, M. D. Polymer-Nanoparticle Electrochromic Materials That Selectively Modulate Visible and Near-Infrared Light. *Chem. Mater.* **2016**, *28*, 1439–1445.

(13) Runnerstrom, E. L.; Llordés, A.; Lounis, S. D.; Milliron, D. J. Nanostructured Electrochromic Smart Windows: Traditional Materials and NIR-Selective Plasmonic Nanocrystals. *Chem. Commun.* **2014**, *50*, 10555–10572.

(14) Horrocks, G. A.; Singh, S.; Likely, M. F.; Sambandamurthy, G.; Banerjee, S. Scalable Hydrothermal Synthesis of Free-Standing VO_2 Nanowires in the M1 Phase. *ACS Appl.*

Mater. Interfaces **2014**, *6*, 15726–15732.

(15) Lopez, R.; Feldman, L. C.; Haglund, R. F. Size-Dependent Optical Properties of VO_2 Nanoparticle Arrays. *Phys. Rev. Lett.* **2004**, *93*, 177403.

(16) Driscoll, T.; Kim, H.-T.; Chae, B.-G.; Kim, B.-J.; Lee, Y.-W.; Jokerst, N. M.; Palit, S.; Smith, D. R.; Di Ventra, M.; Basov, D. N. Memory Metamaterials. *Science.* **2009**, *325*, 1518–1521.

(17) Patridge, C. J.; Whittaker, L.; Ravel, B.; Banerjee, S. Elucidating the Influence of Local Structure Perturbations on the Metal-Insulator Transitions of $V_{1-x}Mo_xO_2$ Nanowires: Mechanistic Insights from an X-Ray Absorption Spectroscopy Study. *J. Phys. Chem. C* **2012**, *116*, 3728–3736.

(18) Wang, N.; Duchamp, M.; Xue, C.; Dunin-Borkowski, R. E.; Liu, G.; Long, Y. Single-Crystalline W-Doped VO_2 Nanobeams with Highly Reversible Electrical and Plasmonic Responses Near Room Temperature. *Adv. Mater. Interfaces* **2016**, *3*, 1600164.

(19) Lee, S.; Cheng, C.; Guo, H.; Hippalgaonkar, K.; Wang, K.; Suh, J.; Liu, K.; Wu, J. Axially Engineered Metal − Insulator Phase Transition by Graded Doping VO_2 Nanowires. *J. Am. Chem. Soc.* **2013**, *135*, 4850–4855.

(20) Manning, T. D.; Parkin, I. P.; Blackman, C.; Qureshi, U. APCVD of Thermochromic Vanadium Dioxide Thin Films - Solid Solutions $V_{2-x}M_xO_2$ (M = Mo, Nb) or Composites VO_2: SnO_2. *J. Mater. Chem.* **2005**, *15*, 4560–4566.

(21) Whittaker, L.; Zhang, H.; Banerjee, S. VO_2 Nanosheets Exhibiting a Well-Defined Metal-Insulator Phase Transition. *J. Mater. Chem.* **2009**, *19*, 2968–2974.

(22) Zhou, J.; Gao, Y.; Zhang, Z.; Luo, H.; Cao, C.; Chen, Z.; Dai, L.; Liu, X. VO_2 Thermochromic Smart Window for Energy Savings and Generation. *Sci. Rep.* **2013**, *3*,

3029.

(23) Zylbersztejn, A.; Mott, N. F. Metal-Insulator Transition in Vanadium Dioxide. *Phys. Rev. B* **1975**, *11*, 4383–4395.

(24) Eyert, V. The Metal-Insulator Transitions of VO_2: A Band Theoretical Approach. *Ann. Phys.* **2002**, *11*, 659–704.

(25) Whittaker, L.; Patridge, C. J.; Banerjee, S. Microscopic and Nanoscale Perspective of the Metal-Insulator Phase Transitions of VO_2: Some New Twists to an Old Tale. *J. Phys. Chem. Lett.* **2011**, *2*, 745–758.

(26) Qazilbash, M. M.; Brehm, M.; Chae, B.-G.; Ho, P.-C.; Andreev, G. O.; Kim, B.-J.; Yun, S. J.; Balatsky, A. V; Maple, M. B.; Keilmann, F.; Kim, H.-T.; Basov, D. N. Mott Transition in VO2 Revealed by Infrared Spectroscopy and Nano-Imaging. *Science.* **2007**, *318*, 1750–1753.

(27) Brito, W. H.; Aguiar, M. C. O.; Haule, K.; Kotliar, G. Metal-Insulator Transition in VO_2: A DFT+DMFT Perspective. *Phys. Rev. Lett.* **2016**, *117*, 056402.

(28) Cao, J.; Ertekin, E.; Srinivasan, V.; Fan, W.; Huang, S.; Zheng, H.; Yim, J. W. L.; Khanal, D. R.; Ogletree, D. F.; Grossman, J. C.; Wu, J. Strain Engineering and One-Dimensional Organization of Metal–Insulator Domains in Single-Crystal Vanadium Dioxide Beams. *Nat. Nanotechnol.* **2009**, *4*, 732–737.

(29) Naoi, Y.; Amano, J. Optimization of VO_2 Nanowire Polymer Composite Thermochromic Films by Optical Simulation. *J. Appl. Phys.* **2016**, *120*, 235301.

(30) Zhao, X.; Vanderbilt, D. First-Principles Study of Structural, Vibrational, and Lattice Dielectric Properties of Hafnium Oxide. *Phys. Rev. B* **2002**, *65*, 233106.

(31) Luo, X.; Demkov, A. A.; Triyoso, D.; Fejes, P.; Gregory, R.; Zollner, S. Combined

Experimental and Theoretical Study of Thin Hafnia Films. *Phys. Rev. B* **2008**, *78*, 245314.

(32) Zhou, B.; Shi, H.; Zhang, X. D.; Su, Q.; Jiang, Z. Y. The Simulated Vibrational Spectra of HfO_2 Polymorphs. *J. Phys. D. Appl. Phys.* **2014**, *47*, 115502.

(33) Frank, D. J.; Dennard, R. H.; Nowak, E.; Solomon, P. M.; Taur, Y.; Wong, H. S. P. Device Scaling Limits of Si MOSFETs and Their Application Dependencies. *Proc. IEEE* **2001**, *89*, 259–287.

(34) Buchanan, D. A. Scaling the Gate Dielectric: Materials, Integration, and Reliability. *IBM J. Res. Dev.* **1999**, *43*, 245–264.

(35) Zhao, X.; Vanderbilt, D. Phonons and Lattice Dielectric Properties of Zirconia. *Phys. Rev. B* **2002**, *65*, 075105.

(36) Waetzig, G. R.; Depner, S. W.; Asayesh-Ardakani, H.; Cultrara, N. D.; Shahbazian-Yassar, R.; Banerjee, S. Stabilizing Metastable Tetragonal HfO_2 Using a Non-Hydrolytic Solution-Phase Route: Ligand Exchange as a Means of Controlling Particle Size. *Chem. Sci.* **2016**, *7*, 4930–4939.

(37) Buchanan, D. A.; Lo, S. H. Growth, characterization and the limits of ultra-thin SiO_2-based dielectrics for future CMOS applications, in *The Physics and Chemistry of SiO_2 and the Si-SiO_2 Interface-3, Electrochemical Society Meeting Proceedings*, Massoud, H. Z.; Poindexter, E. H. and Helms, C. R. Eds. Pennington, NJ: The Electrochemical Society, 1996, pp. 3–14.

(38) Lo, S. H.; Buchanan, D. A.; Taur, Y.; Wang, W. Quantum-Mechanical Modeling of Electron Tunneling Current from the Inversion Layer of Ultra-Thin-Oxide NMOSFET's. *IEEE Electron Device Lett.* **1997**, *18*, 209–211.

(39) Zhao, X.; Vanderbilt, D. First-Principles Study of Electronic and Dielectric Properties of

ZrO_2 and HfO_2. *Mat. Res. Soc. Symp. Proc.* **2003**, *745*, 283.

(40) Wilk, G. D.; Wallace, R. M.; Anthony, J. M. High-k Gate Dielectrics: Current Status and Materials Properties Considerations. *J. Appl. Phys.* **2001**, *89*, 5243–5275.

(41) DiMaria, D. J.; Stathis, J. H. Non-Arrhenius Temperature Dependence of Reliability in Ultrathin Silicon Dioxide Films. *Appl. Phys. Lett.* **1999**, *74*, 1752.

(42) Yeo, Y.-C.; Lu, Q.; Hu, C. MOSFET Gate Oxide Reliability: Anode Hole Injection Model and Its Applications. *International Journal of High Speed Electronics and Systems*. **2001**, *11*, 849–886.

(43) Xu, S.; Jacobs, R. M.; Nguyen, H. M.; Hao, S.; Mahanthappa, M.; Wolverton, C.; Morgan, D. Lithium Transport through Lithium-Ion Battery Cathode Coatings. *J. Mater. Chem. A* **2015**, *3*, 17248–17272.

(44) Kracbk, F. C. The Cristobalite Liquidus in the Alkali Oxide-Silica Systems and the Heat of Fusion of Cristobalite. *J. Am. Chem. Soc.* **1930**, *52*, 1436–1442.

(45) Hudak, B. M.; Depner, S. W.; Waetzig, G. R.; Talapatra, A.; Arroyave, R.; Banerjee, S.; Guiton, B. S. Real-Time Atomistic Observation of Structural Phase Transformations in Individual Hafnia Nanorods. *Nat. Commun.* **2017**, *8*, 15316.

(46) Depner, S. W.; Cultrara, N. D.; Farley, K. E.; Qin, Y.; Banerjee, S. Ferroelastic Domain Organization and Precursor Control of Size in Solution-Grown Hafnium Dioxide Nanorods. *ACS Nano* **2014**, *8*, 4678–4688.

(47) Böscke, T. S.; Müller, J.; Bräuhaus, D.; Schröder, U.; Böttger, U. Ferroelectricity in Hafnium Oxide Thin Films. *Appl. Phys. Lett.* **2011**, *99*, 102903.

(48) Han, W.; Li, M. Thermodynamic Modeling of the Pd-Sb System. *J. Alloys Compd.* **2010**, *507*, 521–525.

(49) Zeng, Q.; Oganov, A. R.; Lyakhov, A. O.; Xie, C.; Zhang, X.; Zhang, J.; Zhu, Q.; Wei, B.; Grigorenko, I.; Zhang, L.; Cheng, L. Evolutionary Search for New High-k Dielectric Materials: Methodology and Applications to Hafnia-Based Oxides. *Acta Crystallogr. Sect. C Struct. Chem.* **2014**, *70*, 76–84.

(50) Shin, D.; Arróyave, R.; Liu, Z. K. Thermodynamic Modeling of the Hf-Si-O System. *Calphad Comput. Coupling Phase Diagrams Thermochem.* **2006**, *30*, 375–386. (Figure I. 2 reprinted and adapted from this source with permission from Elsevier)

(51) Batra, R.; Huan, T. D.; Rossetti, G. A.; Ramprasad, R. Dopants Promoting Ferroelectricity in Hafnia: Insights From A Comprehensive Chemical Space Exploration. *Chem. Mater.* **2017**, *29*, 9102–9109.

(52) Perevalov, T. V.; Gritsenko, V. A.; Erenburg, S. B.; Badalyan, A. M.; Wong, H.; Kim, C. W. Atomic and Electronic Structure of Amorphous and Crystalline Hafnium Oxide: X-Ray Photoelectron Spectroscopy and Density Functional Calculations. *J. Appl. Phys.* **2007**, *101*, 053704.

(53) Tang, J.; Zhang, F.; Zoogman, P.; Fabbri, J.; Chan, S.-W.; Zhu, Y.; Brus, L. E.; Steigerwald, M. L. Martensitic Phase Transformation of Isolated HfO_2, ZrO_2, and $Hf_xZr_{1-x}O_2$ ($0 < x < 1$) Nanocrystals. *Adv. Funct. Mater.* **2005**, *15*, 1595–1602.

(54) Jiang, H.; Gomez-Abal, R. I.; Rinke, P.; Scheffler, M. Electronic Band Structure of Zirconia and Hafnia Polymorphs from the GW Perspective. *Phys. Rev. B Condens. Matter Mater. Phys.* **2010**, *81*, 1–9.

(55) Müller, J.; Böscke, T. S.; Schröder, U.; Mueller, S.; Bräuhaus, D.; Böttger, U.; Frey, L.; Mikolajick, T. Ferroelectricity in Simple Binary ZrO_2 and HfO_2. *Nano Lett.* **2012**, *12*, 4318–4323.

(56) Pulvari, C. F. The Transpolarizer, a Basic Ferroelectric Circuit Element. *IRE Trans. Electron Devices* **1959**, *6*, 248–248.

(57) He, W.; Zhang, L.; Chan, D. S. H.; Cho, B. J. Cubic-Structured HfO_2 with Optimized Doping of Lanthanum for Higher Dielectric Constant. *IEEE Electron Device Lett.* **2009**, *30*, 623–625.

(58) Parija, A.; Waetzig, G. R.; Andrews, J. L.; Banerjee, S. Traversing Energy Landscapes Away from Equilibrium: Strategies for Accessing and Utilizing Metastable Phase Space. *J. Phys. Chem. C* **2018**, *122*, 25709–25728.

(59) Wang, J.; Li, H. P.; Stevens, R. Review Hafnia and Hafnia-Toughened Ceramics. *J. Mater. Sci.* **1992**, *27*, 5397–5430.

(60) Luo, X.; Zhou, W.; Ushakov, S. V; Navrotsky, A.; Demkov, A. A. Monoclinic to Tetragonal Transformations in Hafnia and Zirconia: A Combined Calorimetric and Density Functional Study. *Phys. Rev. B - Condens. Matter Mater. Phys.* **2009**, *80*, 134119.

(61) Seitz, M.; Oliver, A. G.; Raymond, K. N. The Lanthanide Contraction Revisited. *J. Am. Chem. Soc.* **2007**, *129*, 11153–11160.

(62) Garvie, C. The Occurrence of Metastable Tetragonal Zirconia as a Crystallite Size Effect. *J. Phys. Chem.* **1965**, *69*, 1238–1243.

(63) Chevalier, J.; Gremillard, L.; Clarke, D. R.; Clarke, D. R. The Tetragonal-Monoclinic Transformation in Zirconia: Lessons Learned and Future Trends. *J. Am. Ceram. Soc.* **2009**, *92*, 1901–1920.

(64) Iskandarova, I. M.; Knizhnik, A. A.; Rykova, E. A.; Bagatur'yants, A. A.; Potapkin, B. V.; Korkin, A. A. First-Principle Investigation of the Hydroxylation of Zirconia and Hafnia Surfaces. *Microelectron. Eng.* **2003**, *69*, 587–593.

(65) Grain, C. F.; Campbell, W. J. Thermal Expansion and Phase Inversion of Six Refractory Oxides, *U. S. Bur. Mines, Rep. Invest.* **1962**, No. 5982, 21

(66) Zhou, W.; Ushakov, S. V; Wang, T.; Ekerdt, J. G.; Demkov, A. A.; Navrotsky, A.; Zhou, W.; Ushakov, S. V; Wang, T.; Ekerdt, J. G.; Demkov, A. A. Hafnia : Energetics of Thin Films and Nanoparticles. *J. appl. phys.* **2010**, *107*, 123514.

(67) Joo, J.; Yu, T.; Kim, Y. W.; Park, H. M.; Wu, F.; Zhang, J. Z.; Hyeon, T. Multigram Scale Synthesis and Characterization of Monodisperse Tetragonal Zirconia Nanocrystals. *J. Am. Chem. Soc.* **2003**, *125*, 6553–6557.

(68) Tang, J.; Fabbri, J.; Robinson, R. D.; Zhu, Y.; Herman, I. P.; Steigerwald, M. L.; Brus, L. E. Solid-Solution Nanoparticles: Use of a Nonhydrolytic Sol−Gel Synthesis To Prepare HfO_2 and $Hf_x Zr_{1-x} O_2$ Nanocrystals. *Chem. Mater.* **2004**, *16*, 1336–1342.

(69) Turquat, C.; Leroux, C.; Roubin, M.; Nihoul, G. Vanadium-Doped Elaboration and Structural Hafnia: Elaboration and Structural Characterization. *Solid State Sci* **1999**, *1*, 3–13.

(70) Korthuis, V.; Khosrovani, N.; Sleight, A. W.; Roberts, N.; Dupree, R.; Warren, W. W. Negative Thermal Expansion and Phase Transitions in the $ZrV_{2-x}P_xO_7$ Series. *Chem. Mater.* **1995**, *7*, 412–417.

(71) Turquat, C. Structural Investigation of Temperature-Induced Phase Transitions in HfV_2O_7. *Eur. Phys. J. Appl. Phys.* **2000**, *10*, 15–27.

(72) Evans, J. S. O. Negative Thermal Expansion Materials. *J. Chem Soc., Dalt. Trans.*, **1999**, 3317–3326.

(73) Buchanan, R. C.; Wolter, G. W. Properties of Hot-Pressed Zirconium Pyrovanadate Ceramics. *J. Electrochem. Soc.* **1983**, *130*, 1905.

CHAPTER II

ELUCIDATING THE CRYSTALLITE SIZE DEPENDENCE OF THE THERMOCHROMIC PROPERTIES OF NANOCOMPOSITE VO_2 THIN FILMS

II.1 Introduction

Buildings account for an inordinately large amount of energy consumption across the planet and are often static structures that remain unchanging in the face of changing seasons and diurnal temperature variations.[1] A recent report from the United Nations estimates that 30—40% of primary energy usage across the world occurs within buildings.[1] In the United States, the Department of Energy estimates that 41% of the total energy consumption can be attributed to buildings.[2,3] Much of the energy consumed within buildings goes towards space cooling, space heating, lighting, and ventilation. Incorporating responsive elements that can adapt to external stimuli (e.g., external temperature and humidity) within structural elements has been proposed as a potential means of reducing the energy footprint of buildings.[4,5] Fenestration elements such as windows, doors, and skylights, play an important role in determining the solar heat gain of a building. Such elements must balance the competing needs of enabling interiors to be lighted using natural daylight while modulating solar heat gain to acceptable levels. Consequently, there is great interest in the development of spectrally selective thin films that allow for transmission of visible light while enabling dynamical modulation of infrared transmittance in response to the external temperature.[4–10] Such thin films are expected to bring about substantial energy savings by blocking infrared light during periods of high ambient temperature (thereby reducing the need

---

*Reprinted from "Elucidating the Crystallite Size Dependence of the Thermochromic Properties of Nanocomposite VO_2 Thin Films" by Fleer, N. A.[1]; Pelcher, K. E.[1]; Horrocks, G. A.; Braham, E.J.; Zou, J.; Farley, K. E.; Naoi, Y.; Amano, J.; Banerjee, S. *ACS Omega*, **2018**, *3*, 14280-14293 https://pubs.acs.org/doi/10.1021/acsomega.8b02093 © 2018 Amercan Chemical Society. All rights reserved. Further permissions to the material excerpted should be directed to the ACS.

for space cooling) but permitting transmittance of infrared light during periods of low ambient temperature when the solar heat gain can be harnessed to reduce heating costs. Nearly 45% of the total solar energy in the range between 400—2500 nm corresponds to near-infrared radiation (780—2500 nm); consequently, a reduction in the solar flux in the near-infrared region would drastically reduce the transmitted energy associated with solar heat gain.[11]

Dynamically tunable glazing requires stimuli-responsive modulation of optical transmittance, which can be achieved variously by means of thermotropic or lyotropic phase transitions in polymers or hydrogels, electric-field-induced ion intercalation in redox-active host materials, reversible amorphous to crystalline transitions in phase-change materials, electric-field-induced change of polarization of liquid crystals, or electronic solid—solid phase transitions.[5,10,12–16] Thermochromic transitions are particularly important as a facile means of developing dynamically switchable glazing that does not require external voltage control.[17] Compounds that exhibit pronounced modulations of optical transmittance as a result of electronic transitions wherein the intrinsic electronic conductivity (carrier concentration and/or mobility) is dramatically altered are particularly attractive.[14,18–20] However, there exists only a relatively sparse set of compounds characterized by large thermally induced modulations of electrical conductance; such electronic phase transitions are underpinned typically by either electron correlation or electron—phonon coupling.[14,18,19,21–24] The binary vanadium dioxide (VO_2) is notable in having an electronic phase transition that occurs in close proximity to room temperature.[19,25] In the bulk, the metal—insulator transition of VO_2 is observed at ca. 67°C but can be depressed through size control or the incorporation of substitutional/interstitial dopants.[17,26–32] The underlying origin of the transition remains hotly contested given that the transition has both electronic (Mott—Hubbard) and structural (Peierls') attributes.[19,28,33–35]

Regardless of the fundamental origin of the transition, the dramatic modulation of optical transmittance and electrical conductivity observed at the phase transition makes VO_2 a useful material for practical applications.

For deployment of VO_2 within thermochromic thin films, wherein it can be integrated within various parts of the building envelope,[9,10,36] three compelling requirements must be addressed: (a) the luminous transmittance (a quantitative measure of light in the region visible to the human eye) must be maintained as high as possible while maximizing thermochromic modulation in the near-infrared region of the electromagnetic spectrum; this requires mitigation of various light scattering mechanisms (*vide infra*); (b) the thin film must be thermally cyclable without strain-induced cracking; the substantial lattice strain accompanying the structural phase transformation renders the deployment of continuous thin films rather difficult and instead nanostructures embedded within suitable matrices are better able to accommodate such strain;[37–39] (c) the nanocrystallites need to be well dispersed within the host matrix to prevent light scattering and to ensure retention of mechanical integrity of the film across multiple thermal cycles. It is thus expected that a viable thermochromic thin film will comprise high-crystalline-quality VO_2 nanocrystals of the optimal particle size embedded within the appropriate host matrix.[40–43] Some notable efforts in the literature, such as by Chen *et al*., have resulted in ΔT_{sol}, the modulation in transmittance from 400—2500 nm, reaching as high as 19.1% when VO_2 is encapsulated in ZnO.[44] Values of T_{lum}, luminous transmittance in the 400—780 nm range, as high as 62.1% have been demonstrated by Zhang *et al*.[45] through grinding of VO_2 particles. However,

fundamental mechanistic understanding of the influence of different scattering mechanisms on the thermochromic performance of nanocomposite films remains to be elucidated.

Previous work has shown that high-crystalline quality VO_2 nanocrystals are accessible through low-temperature hydrothermal methods.[26,27,46,47] Such methods provide substantial control over particle size and dopant incorporation; the obtained nanostructures can be extensively thermally cycled without cracking. In past work, we have incorporated hydrothermally grown VO_2 nanowires within an amorphous silica matrix utilizing a modified Stöber method.[48] The silica matrix permits adhesion to glass substrates and provides protection against oxidation. VO_2 particles have further been used in other studies to prepare nanocomposite thin films using polymer-assisted deposition and through mixing with an acrylic resin.[49,50] However, the first and third of the problems noted above: optimal particle size and good dispersion remain to be adequately resolved. Here, we contrast the visible light transmittance and infrared modulation obtained for different particle sizes of VO_2 embedded within a commercially available methacrylic acid/ethyl acrylate copolymer, Acrysol ASE-60™. The rheology of this matrix enables the use of draw-down coating for the preparation of nanocomposite VO_2 thin films. Films formulated with four different sizes of VO_2 nanocrystals at various mass loadings have been examined; a detailed evaluation of light scattering mechanisms occurring within the nanocomposite thin films underscores that a combination of both nanometer-sized dimensions and excellent dispersion at the crystallite level (without agglomeration as particles) is imperative to obtain the desired high degrees of visible light transmittance and thermochromic modulation.

II.2 Experimental

Optical Simulations. To simulate the light scattering properties of a single VO_2 nanowire, finite element analysis (FEA) was used. Scattering cross sections, absorption cross sections, and angular distributions of scattered light intensity were obtained based on the FEA simulation. In order to evaluate the optical properties of nanowire composite films using the computed cross section and angular distribution, a conventional geometrical optics calculation (GO) was used. To simplify the calculation, the following assumptions were applied; (1) low fill factor of nanowires with no interactions between the nanowires, (2) nanowires aligned along the composite surface plane (which corresponds to the worst case for optical transmission), and (3) perpendicular incidence of light on the composite surface. A more comprehensive description of the simulation method and geometrical calculation has been published elsewhere.[51]

Synthesis of VO_2 Nanowires. VO_2 nanowires were synthesized through a variation of the one-step hydrothermal method reported in our previous work.[26] The process from synthesis of VO_2 nanocrystals to casting of nanocomposite thin films is schematically outlined in Figure II. 3 (shown later)**.** Briefly, stoichiometric amounts of micron-sized V_2O_5 powder (Sigma-Aldrich, 98%) were placed in a polytetrafluoroethylene receptacle with deionized water (ρ=18.2 M$\Omega \cdot cm^{-1}$, Barnstead Water Purification System) and a reducing agent (either 2-propanol or acetone). The cup was then sealed in an autoclave and heated at 210°C for 18—72 h. The synthesized VO_2 (B) powder was then vacuum filtered and washed with 2-propanol, acetone, and/or water. The powders were subsequently annealed at 550°C under inert Ar atmosphere for several hours to obtain phase-pure VO_2 nanocrystals crystallized in the M1 phase upon cooling.[47]

Milling of VO_2 Nanowires. M1 VO_2 nanowires synthesized hydrothermally *via* reduction with 2-propanol were dry-milled milled using methacrylate polymer beads. Samples

were milled in 100 mg quantities for a total of 150 min at 30 min intervals using three polymer beads per tube in a SPEX SamplePrep 510 Mixer Mill.

Synthesis of VO_2 NS. VO_2 NS were synthesized *via* a two-step reaction based on the modification of a method reported in the literature.[52–54] The first step involved the precipitation of $VO(OH)_2$ from the reaction of NH_4VO_3 and H_2NNH_2 at 80°C in deionized water (ρ=18.2 $M\Omega \cdot cm^{-1}$, Barnstead Water Purification System). The $VO(OH)_2$ precipitate was then placed within a hydrothermal vessel and heated at 210°C for 24—72 h. The product was finally isolated through centrifugation and used without further annealing or milling.

Deposition of a SiO_2 Shell and Preparation of VO_2@SiO_2 Nanocrystals. An amorphous silica shell was deposited onto nanoparticles using a modified Stöber method.[48,54] Briefly, VO_2 nanocrystals (in quantities ranging from 24 to 240 mg) were ultrasonicated in a 4:1 (99.5% alcohol content. 100% non-denatured ethanol) ethanol:deionized water solution to obtain stable colloidal dispersions. For every 24 mg of VO_2 nanocrystals utilized, 400 µL NH_4OH (0.25M aqueous solution) was added as a catalyst followed by addition of 200 µL tetraethylorthosilicate (yielding a final concentration of 0.02 M). The reaction was allowed to proceed for 25 min and the VO_2@SiO_2 nanocrystals were collected by centrifugation. The solid collected *via* centrifugation was subsequently washed with copious amounts of 99.5% ethanol recovered by centrifugation. Three such cycles were performed prior to incorporation of the nanocrystals within the polymer matrices.

Dispersion within Copolymer Matrix. Polymer dispersion was carried out as reported in a previous work and schematically outlined in Figure 3.[54] VO_2@SiO_2 core—shell nanocrystals was dispersed in 10 mL of an alkaline aqueous solution (pH of ca. 11.3 prepared by addition of 2-amino-2-methyl-1-propanol containing 5% added water (Amresco) to deionized water) in a

glass vial by ultrasonication. The dispersion was then gently stirred and methacrylic acid/ethyl acrylate copolymer, Acrysol ASE-60™ (Dow Chemical Company) was introduced at 1 wt.% relative to water (adjusted to account for Acrysol ASE-60's solid content being around 28 wt.%). The solution was stirred more vigorously as the solution thickened to further homogeneously disperse the nanocrystals within the polymeric matrix. Upon dissolution of the methacrylic acid/ethyl acrylate copolymer in the alkaline solution (ca. 20 min), the dispersion was allowed to stand and used for casting thin films.

Film Casting. Films were cast from the polymer dispersions in a manner previously reported.[54] Nanocomposite thin films of VO_2@SiO_2 were cast onto borosilicate glass substrates using 1.25 mL of the methacrylic acid/ethyl acrylate copolymer/VO_2 dispersion with various loadings of VO_2 nanocrystals (4—8 mg of VO_2@SiO_2 dispersed in 10 mL of the acrylate aqueous solution). The dispersion was placed on the glass slide and drawn down using a BYK film casting knife set to a wet thickness of 1 mm. The films were then allowed to dry overnight in an air ambient. The dry thickness of the films was on the order of ca. 1—2 μm.

Characterization. High-resolution transmission electron microscopy (HR-TEM) images of VO_2 and VO_2@SiO_2 nanocrystals were obtained using a JEOL JEM-2010 instrument operated at 200 kV with a beam current of 100 mA and. SAED patterns were acquired using an FEI Tecnai G2 F20 ST field-emission TEM at a 200 kV operating voltage. Samples for HRTEM were prepared by dispersing the VO_2 and VO nanoparticles in 2-propanol or ethanol and dropping the dispersion onto 300 mesh copper grids coated with amorphous carbon. The grid was then allowed to dry under ambient conditions.

Differential scanning calorimetry (DSC) was performed using a Q2000 TA Instrument calorimeter with Al sample pans and lids. A scan rate of 10°C/min was used in the temperature range between 0 to 100°C.

Film thicknesses were determined using a Bruker Dimension Icon atomic force microscope operating in tapping mode. The AFM tip was a Mikromasch USA HQ:NSC35/Al BS three cantilever tapping mode n-type silicon tip with a radius of 8 nm, height of 12—18 μm, and a full tip cone angle of 40°. Powder X-ray diffraction (XRD) patterns were obtained using a Bruker D8 Advance Eco X-ray powder diffractometer utilizing Cu Kα radiation (λ = 1.5418 Å). Transmission spectra of nanocomposite films were obtained using a multi-wavelength Bruker Vertex-70 FTIR spectrometer utilizing a Pike Technologies temperature stage and allowed to equilibrate for 10 min at each temperature. A Perkin Elmer Lambda 950 UV/Vis/NIR Spectrophotometer with a 150 mm integrating sphere equipped with a custom designed and calibrated heating stage was also used for acquisition of transmission and absorptance spectra. Films were allowed to equilibrate for 5 min at each temperature. All transmission spectra were corrected for the transmission of the methacrylic acid/ethyl acrylate copolymer and glass by taking a blank spectra of glass and polymer and adding the reduction in optical transmittance attributed to the glass and copolymer alone; consequently the measured values correspond to the optical properties of the embedded VO_2 nanocrystals.

In order to standardize film performance, the solar (T_{sol}: 400—2500 nm), luminous (T_{lum}: 400—780 nm) and NIR (T_{NIR}: 780—2500nm) transmittance were determined according to the following **Equations II. 1 and II. 2**[55–57]:

$$T_x = \frac{\int \varphi_x(\lambda) T(\lambda) d\lambda}{\int \varphi_x T(\lambda) d\lambda} \text{where } x = sol/lum/NIR \qquad \text{(II. 1)}$$

$$\Delta T_x = T_x(low\ temp) - T_x(high\ temp) \qquad \text{(II. 2)}$$

where $T(\lambda)$ is the recorded film transmittance, and $\varphi_x(\lambda)$ is the solar irradiance spectrum distribution for air mass 1.5 (corresponding to the sun at 37° above the horizon) over the wavelength range specified.[11] The wavelength ranges for the sol, lum, and NIR ranges of the electromagnetic spectrum denoted as subscripts in Equation II. 1 are defined as 400—2500 nm, 400—780 nm, and 780—2500 nm respectively.

An iPhone 5s was acquired from Eigen Imaging Inc. and was used to image the transition in the NIR region of electromagnetic spectrum. Removal of the factory installed 650 nm shortpass filter and utilization of a 850 nm longpass filter acquired from Thorlabs Inc. allowed for exclusion of shorter wavelengths. The sensitivity range of the camera is between 850 nm and 1000 nm owing to the combination of longpass filter and spectral response of the CMOS sensor of the camera. During the imaging experiment shown in **Video A. 1**, a 5 mg/10 mL loading NS nanocomposite VO_2@SiO_2/ methacrylic acid/ethyl acrylate copolymer thin film was heated from 35°C to 90°C with a heat gun. Post-processing of the video was done using Avidemux and Windows Movie Maker. The video is available as a supplementary file to compliment this dissertation.

II.3 Results and Discussion

The use of nanocrystals instead of continuous thin films provides several key advantages. First, as noted above, strain-induced delamination and cracking of continuous thin films resulting from the lattice mismatch at the monoclinic—tetragonal structural phase transition can be

mitigated.[16,26] Secondly, nanocrystals embedded within flexible polymeric thin films serve as retrofittable solutions, providing a means of readily modifying existing solar control films, and thus can be deployed onto existing buildings without requiring replacement of insulating glass units in their entirety. Finally, nanocrystals can be prepared in a highly crystalline form by scalable solution-phase methods and do not require high-vacuum deposition chambers necessary for physical vapor deposition of VO_2.[46] However, the utilization of nanocrystals within optical quality thin films brings its own set of challenges associated with determining the optimal crystallize size and ensuring good dispersion of VO_2 nanocrystals within matrices such as to mitigate light scattering arising from the agglomeration of crystallites.

Li *et al.* have suggested a pronounced size dependence for the optical transmittance and near-infrared modulation of VO_2 nanocrystals embedded within a dielectric matrix.[58] These authors have found that nanocomposite films constituted by dispersing spherical and elliptical shaped VO_2 nanocrystals present several advantages over continuous thin films of VO_2. First, the spectral transmittance of the insulating phase of VO_2 is predicted to be much higher for films with VO_2 nanocrystals dispersed within a matrix as compared to continuous thin films. In addition, the near-infrared modulation for the particulate thin films was further found to be substantially greater than that of the continuous thin films. In order to elucidate the crystallite size dependence of the optical properties, simulations have been performed using effective medium approximation (EMA) and finite element analysis + geometrical optics (FEA+GO) models (**Figure II. 1**). The simple EMA approach assumes that the nanoparticle has a single refractive index (n) and extinction ratio (k), and assumes that the particles are homogeneously distributed throughout a low-n medium (Figure 1A). The simulated spectrum (Figure 1B) predicts a dramatic modulation at a maximum of ca. 40% in the near-IR region of the

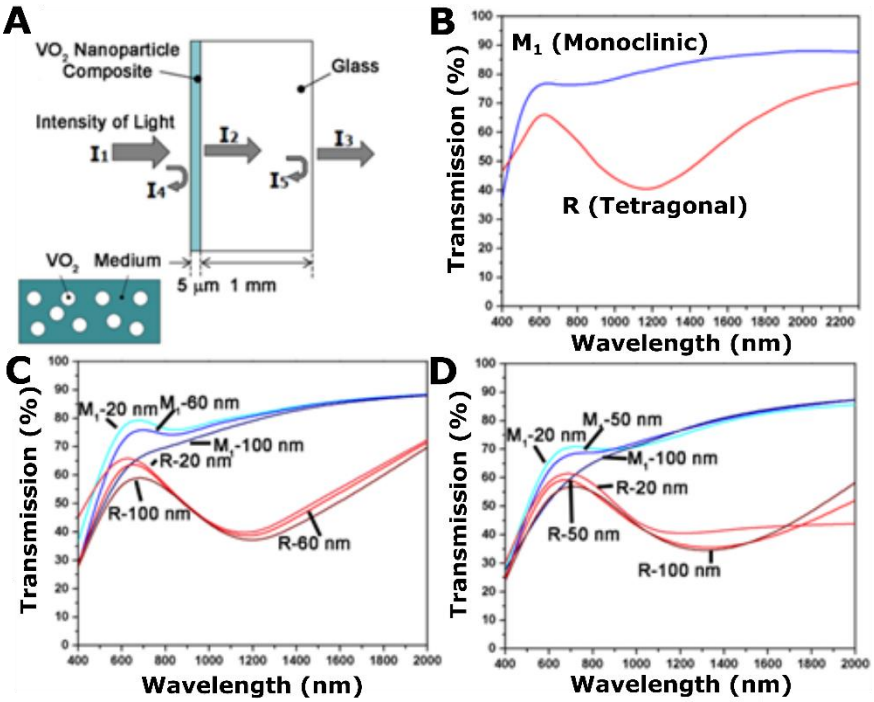

Figure II. 1 A) Schematic depiction of configuration used to model optical spectra of nanocomposite thin films comprising VO_2 nanocrystals embedded within a 5 μm thick polymer film cast onto a 1 mm thick glass substrate. Effective medium approximation (EMA) and FEA+GO methods are used to model the optical response for insulating and metallic phases of VO_2. I_1 is the incident radiation, I_2 is the transmitted intensity at the first plane, and I_4 is the reflected intensity at the first (coated surface). I_3 and I_5 are the transmitted and reflected intensities at the second (uncoated) glass surface, respectively. Bulk optical constants for the insulating and metallic phases of VO_2 are used as described in the text. A fill factor of 3.7 wt.% is assumed for all films. A temperature-invariant refractive index of 1.5 is assumed for the host polymeric matrix.[60] B) Transmittance spectra simulated based on the effective medium approximation model for spherical nanoparticles of insulating and metallic VO_2. C) Transmittance spectra simulated based on the FEA+GO approach for a nanocomposite thin film with spherical VO_2 nanoparticles of varying diameters (as labeled in the plot) in the insulating and metallic phase. D) Transmittance spectra simulated based on the FEA+GO approach for a nanocomposite thin film with 100 nm length VO_2 nanowires of varying diameters (as labeled in the plot) in the insulating and metallic phase.

electromagnetic spectrum when using the optical constants of bulk VO_2 in the monoclinic (M1) and tetragonal phases.[58,59] The simulation assumes a constant *n* of ca. 1.5 for the host matrix, which is typical of polymeric media.[60,61] The FEA+GO simulations allow for a more detailed elucidation of particle-size-dependent optical properties. Spectra have been simulated for a

composite with a fill factor of 3.7 wt.% of spherical VO_2 nanoparticles of varying diameters again assuming a temperature-independent *n* of 1.5 for the polymeric media and the bulk optical constants for the insulating and metallic phases.[60,61] As the diameter increases from 20 to 100 nm, the near-infrared modulation is observed to remain constant at ca. 40% (Figure 1C). However, the maximum visible light transmittance (at 680 nm) decreases from 80% to 68% for the low-temperature phase. When considering a composite of 100 nm long VO_2 nanowires with varying diameters, the 50 and 100 nm diameter nanowires show a maximum modulation of ca. 45% in the near-infrared region of the electromagnetic spectrum, whereas the 20 nm nanowires are predicted to exhibit a maximum modulation of ca. 40% (Figure 1D). Although the NIR modulation is slightly diminished for the 20 nm diameter nanowires, they retain superior visible light transmittance. The substantial diminution in visible light transmittance with increasing particle is derived from the scattering background contributed by larger particles. Agglomeration of particles will to first order mimic the effects of having larger particles. A reduction in *n* from 3.0 to 2.2 at 700 nm when transitioning from an insulator (M1) to metal (R) is also responsible for an increase in visible transmission in the metal phase, but this change is constant between films and has little impact on variations in film performance.[62,63] These simulations indicate that the viability of utilizing VO_2 nanocrystals for effective thermochromic modulation will depend sensitively on their dimensions and extent of dispersion within the host matrix.

In order to experimentally study the effects of particle size on the optical spectra of the nanocomposite films, VO_2 nanocrystals have been synthesized using different hydrothermal methods, as detailed in the experimental section.[26,52,53] Four different particle size are examined here: Sample I are nanowires prepared by the hydrothermal reduction of V_2O_5 by 2-propanol and span 210±70 nm in diameter and range tens of microns in length as shown in **Figure II. 2A**.[46]

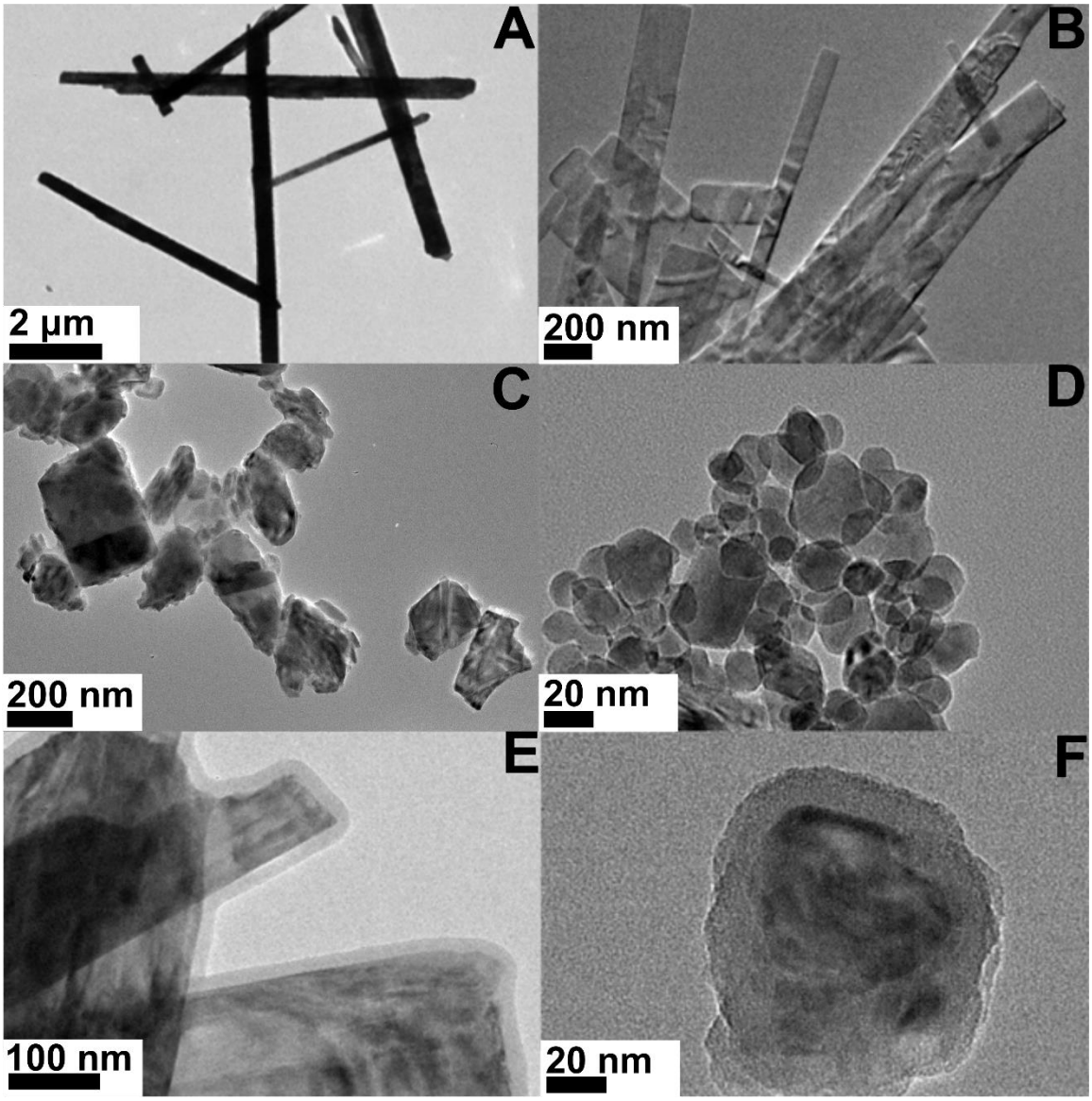

Figure II. 2 TEM images of VO_2 nanocrystals grown via: A) hydrothermal reduction of V_2O_5 by 2-propanol (Sample I); B) hydrothermal reduction of V_2O_5 by acetone (Sample A); C) hydrothermal reduction of V_2O_5 by 2-propanol followed by dry-milling with methacrylate polymer beads (Sample I-BM); and D) precipitation of $VO(OH)_2$ followed by hydrothermal crystallization (Sample NS). TEM images of VO_2 nanocrystals coated with an amorphous SiO_2 shell for E) Sample I and F) Sample NS.

The use of acetone as a reducing agent yields nanowires that again span several micrometers in length but with reduced diameters of 180±70 nm (Figure II. 2B). These samples are referred to as Sample A. To reduce the longitudinal dimensions, the nanowires of Sample I have been dry-

milled with methacrylate polymer beads to obtain Sample I-BM (Figure II. 2C). Ball milling greatly diminishes the particle width to 110±90 nm but the nanocrystals are observed to be highly agglomerated and some amorphization of the crystallites is discernible. Histograms of size distributions obtained from statistical analysis of TEM images have been documented in our previous work.[29] Finally, to achieve VO_2 nanospheres with an approximate size distribution of 44±30 nm, $VO(OH)_2$ is first precipitated using sol—gel techniques, followed by hydrothermal crystallization (referred to as Sample NS, Figure II. 2D).[52,53] The synthesis of VO_2 NS by hydrothermal methods from reduction of pentavalent vanadium precursors has been reported in previous work by Zhou, Jin, and co-workers.[53] Size Heating and cooling phase transitions for each of these samples is shown in Figure A 1 (Appendix A). Heating transition temperatures for I, A, and I-BM samples are between 66—70°C; comparable to bulk VO_2, whereas the NS sample transitions slightly lower at 57°C likely due to surface effects as delineated in previous work.[46,54,64] Scaling to finite size diminishes the transition temperature of both the heating and cooling transitions of VO_2; surface-nucleation mechanisms allow for the monoclinic→tetragonal transformation to be initiated at lower temperatures upon heating; in contrast, the cooling transition is mediated by point defects and is suppressed as a result of the lower density of nucleation sites.[60] Nucleation restrictions for smaller particle volumes (smaller nanocrystals allow for more facile migration of oxygen vacancies to surfaces, thereby diminishing the density of putative nucleation sites) bring about an increase in hysteresis as observed in Figure A 1.[53,54,64,65] Notably, the large hysteresis resulting from a reduced concentration of nucleation sites renders crystalline particles with much smaller dimensions of limited practical utility for thermochromic applications. **Figures A 2 and A 3** exhibit powder X-ray diffraction patterns and selected area electron diffraction (SAED) patterns acquired for the nanoparticles used in this

study, respectively, confirming that they crystallize in the monoclinic M1 phase.[46,66] The SAED patterns attest to the single-crystalline nature of the VO_2 nanowires (Fig. A 3); a combination of discrete diffraction spots and diffuse rings are observed for the NS samples as a result of their agglomeration within polycrystalline agglomerates (Fig. A 3D). Extensive Raman spectroscopy characterization of hydrothermally prepared VO_2 nanowires has been published in our previous work.[46] The hydrothermal methods are documented to yield high-crystalline quality VO_2 nanocrystals exhibiting abrupt four orders of magnitude changes in conductance in single-nanowire electrical transport measurements.[46] The four samples examined here provide an effective means for elucidating particle size effects on visible light transmittance and near-infrared modulation of nanocomposite thin films. Notably, the focus of this article is the elucidation of crystallite size effects on thermochromic performance for well-characterized nanostructures with varying dimensions with a particular emphasis on examination of the size-dependence of light scattering mechanisms; consequently, parameters pertaining to the encapsulating matrix (dielectric shell thickness, surface functionalization of shells, and choice of polymeric matrix as will be discussed below) have been held constant while varying particle size. All of these parameters can undoubtedly be further improved to enhance functional performance.[43]

Our previous work has illustrated the importance of protecting the VO_2 nanocrystals from oxidative degradation by deposition of amorphous silica shells.[48] The silica shells do not alter the magnitude or phase transition temperature but passivate the surfaces of VO_2, endow stability up to temperatures of 300°C, allow for much improved dispersion in aqueous media, and facilitate refractive index matching (the refractive index of SiO_2 is 1.8,[67,68] intermediate between that of the embedded VO_2 nanocrystals and the host polymer matrix (ca. 1.5)). In the absence of a SiO_2

coating, VO_2 nanocrystals dispersed in aqueous media are rapidly degraded to green substoichiometric vanadium oxides (such as V_6O_{13}) and orange V_2O_5. All four samples noted above have been coated with SiO_2 using a modified Stöber approach.[48] In previous work, we have demonstrated the functionalization of SiO_2 shells with perfluorinated silanes, which further renders the nanocrystals superhydrophobic and ensures their long-term preservation at high relative humidities.[54] However, this additional treatment has not been performed here to maintain well-defined interfaces with gradation of refractive indices (VO_2/SiO_2/polymeric medium). Figures II. 2E and F depict representative TEM images of silica-coated VO_2 nanocrystals indicating an average shell thickness of 4.0 ± 0.6 nm following the procedure described in the methods section.

In order to devise a scalable process for casting thin films of VO_2 nanocrystals, a methacrylic acid/ethyl acrylate (MAA/EA) copolymer is used as a dispersant and thickener. The polymeric matrix is typically stored under acidic conditions; upon titration of a base, methacrylic acid groups within the copolymer become deprotonated and take on an anionic charge.[69] Charge repulsion between anionic groups induces swelling of the copolymer, substantially modifying the rheology of the dispersion, and allowing for stabilization of solution-castable dispersions of VO_2@SiO_2 nanocrystals. **Figure A 4A** (Supporting Information) illustrates MAA/EA copolymer dispersions of VO_2@SiO_2 nanocrystals allowed to stand for up to 7 days after mixing. Figure A 4B contrasts the stability of the VO_2@SiO_2 colloidal dispersions in deionized water, with and without the addition of the MAA/EA copolymer, as a function of time clearly illustrating the decreased sedimentation obtained for the dispersion where the polymer is present. The viscous acrylic dispersions have been used to cast VO_2 nanocomposite coatings using a facile straight-edge knife casting process. **Figure II. 3** shows a process flow diagram for the preparation of the

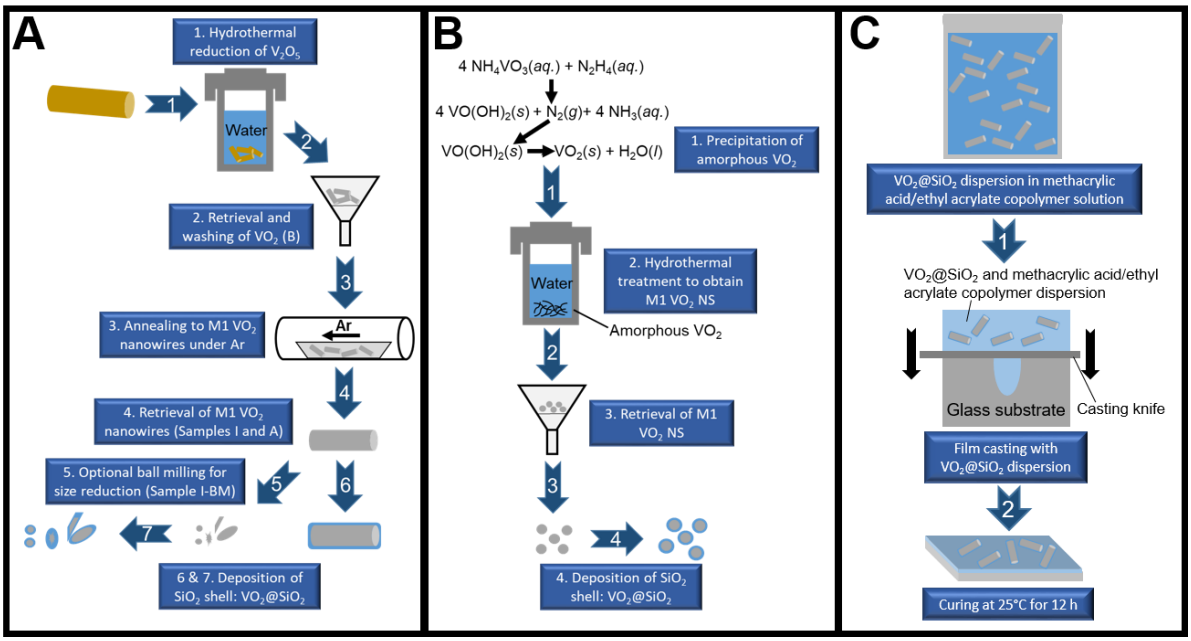

Figure II. 3 Schematic illustration of the process used to prepare nanocomposite thermochromic elements. **A. 1.)** V_2O_5 powder is placed in a hydrothermal vessel with deionized water and the reducing agent of choice (either acetone to yield Sample A or 2-propanol to obtain Sample I). The solution is heated at 210°C for 18—72 h. **2.)** Vacuum filtering and washing of the retrieved VO_2 (B) followed by **3.)** Annealing of retrieved VO_2 under argon to obtain nanowires in the M1 phase. **4.)** Retrieval of M1 VO_2 nanowires followed by **5.)** dry milling with methacrylate polymer beads to reduce size (Sample I-BM) followed by **6**,**7)** coating with an SiO_2 shell to minimize aggregation, provide gradation of refractive indices, and obtain VO_2@SiO_2 nanocrystals. Panel **B** shows the process for synthesis of VO_2 NS. **1.)** Reaction that results in precipitation of amorphous VO_2. **2.)** Hydrothermal treatment of amorphous VO_2 to obtain NS crystallized in the M1 phase. **3.)** Filtering and washing of M1 VO_2 NS followed by **4.)** coating with an SiO_2 shell to obtain VO_2@SiO_2 nanocrystals. Panel **C** outlines the film casting process beginning with VO_2 dispersion in an aqueous solution methacrylic acid/ethyl acrylate copolymer followed by **1.)** casting of films by depositing the dispersion on a borosilicate glass substrate and drawing a casting knife down along the surface to create an even film. **2.)** Curing for 12 h to obtain a homogeneous nanocomposite film.

nanocomposite thermochromic elements. The obtained films are visually transparent and smooth as depicted in Figure A 4C—Figure A 4F of Appendix A. As expected and discussed in greater detail below, the nanocomposite films embedded with the smallest particles show the least amount of haze and the highest optical transmittance in the visible region of the electromagnetic spectrum owing to the most effective mitigation of light scattering. For the same VO_2

nanocrystal loading (0.6 mg VO_2@SiO_2/mL solution), it is clear that the nanowire samples with larger dimensions (Samples I, A, and I-BM) show considerably greater haze as compared to the NS nanocrystals indicating different absorption/scattering wavelength profiles.

Visible-NIR transmission spectra of nanocomposite films prepared using the four VO_2@SiO_2 samples are shown in **Figure II. 4**. The corresponding transmittance and NIR modulation values are listed in **Table II. 1**. Three different nanocrystal loadings have been

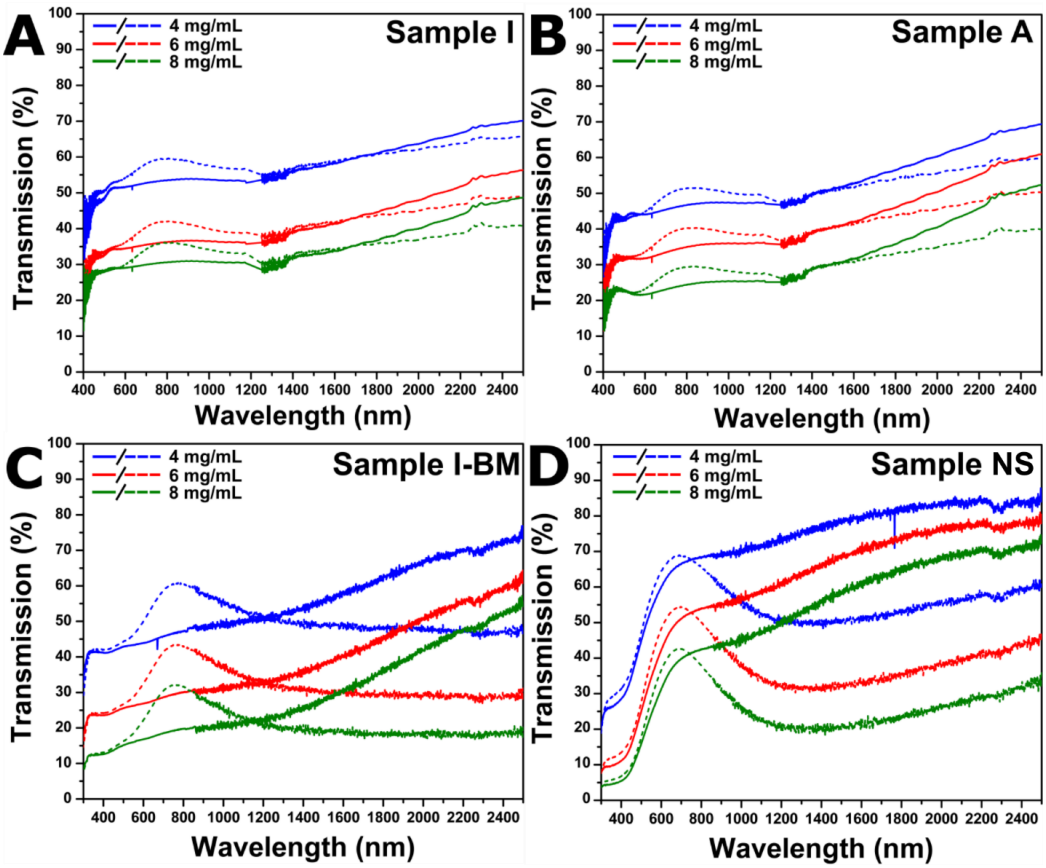

Figure II. 4 Vis-NIR transmission spectra acquired for nanocomposite VO_2@SiO_2/ methacrylic acid/ethyl acrylate copolymer thin films prepared from dispersions with nanocrystal loadings of 4 mg/10 mL (blue lines), 6 mg/10 mL (red lines), and 8 mg/10 mL (green lines). In each case, the solid lines represent spectra acquired at 35°C, whereas the dotted lines represent spectra acquired at 85°C after equilibration for 10 min. A) Sample I at different nanocrystal loadings; B) Sample A at different nanocrystal loadings; C) Sample I-BM at different nanocrystal loadings; and D) Sample NS at different nanocrystal loadings.

Table II. 1 Collated data summarizing ΔT_{sol} (%), ΔT_{NIR} (%), T_{lum} (%), and onset of NIR modulation for the four different size distributions of VO_2 nanocrystals encapsulated within SiO_2 shells for various particle loadings dispersed in an acrylate matrix. T_{lum} (%) is shown for films at 25°C.

Sample (size in nm)	**ΔT_{sol} (%)**			**ΔT_{NIR} (%)**			**T_{lum} (%) (ΔT_{lum}(%))**			**Onset of NIR Modulation (nm)**		
	4 mg/ 10 mL	6 mg/ 10 mL	8 mg/ 10 mL	4 mg/ 10 mL	6 mg/ 10 mL	8 mg/ 10 mL	4 mg /10 mL	6 mg/ 10 mL	8 mg/ 10 mL	4 mg/ 10 mL	6 mg/ 10 mL	8 mg/ 10 mL
I (210±70)	-2.60	-2.00	-1.60	-0.90	-0.30	-0.20	51.9 (-3.5)	34.8 (-2.8)	29.4 (-2.00)	1730	1660	1660
A (180±70)	-0.90	-1.30	-1.00	1.00	0.80	1.30	44.6 (-1.8)	32.4 (-2.8)	22.2 (-2.5)	1380	1380	1380
I-BM (110±90)	-1.54	-0.83	0.25	6.13	7.52	9.08	44.48 (-8.30)	27.42 (-7.42)	17.30 (-7.49)	1208	1184	1150
NS (44±30)	10.28	13.52	16.62	23.18	30.34	32.18	61.44 (-3.43)	44.44 (-4.60)	33.47 (-4.04)	749	746	741

contrasted in each instance. The visible light transmittance is diminished in each case with increasing loading in dicating higher absorption and scattering events within the nanocomposite matrix; the former as a result of the higher optical density resulting from the increased fill factor and the latter as a result of increasing agglomeration of crystallites or primary articles (*vide infra*). All spectra show a clear divergence of the high-temperature (dotted line) spectrum from the low-temperature (solid line) spectrum in the NIR region of the electromagnetic spectrum. The insulating phase of bulk VO_2 has a bandgap estimated to be ca. 0.6 eV, whereas with closing of the bandgap and sharp increase in carrier density upon metallization, the transmittance is greatly diminished in the NIR region of the electromagnetic spectrum. For samples I and A, with the largest dimensions of nanocrystals under consideration, four correlated observations point the operation of multiple scattering mechanisms: (a) the intriguing observation of higher visible-light transmittance (T_{lum}) at high temperatures for both sets of films at all loadings; (b) decreased transmission for sample A compared to I for any given loading; (c) relatively greater near-infrared

modulation (ΔT_{NIR}) for A as compared to I for any given loading; (d) a pronounced blue-shift in onset wavelength of ΔT_{NIR} for sample A in comparison to sample I.

The first and most notable observation is the significant increase in T_{lum} at higher temperatures and is explicable considering the change in n of the VO_2 nanocrystals as a result of the insulator—metal phase transition. The value of n at 700 nm for VO_2 is 3.0 for the M1 phase and 2.2 for the R phase,[62,63] which results in a greater n mismatch between VO_2 and the MAA-EA copolymer host matrix at low temperatures. The SiO_2 shell with an intermediate n value of 1.8 facilitates refractive-index matching between the embedded nanocrystals and the host matrix,[67,68] thereby serving as an anti-reflective coating and minimizing light scattering at the VO_2/ MAA-EA copolymer interface depending on shell thickness. In this study, the shell thicknesses have been held constant for all of the four nanocrystal sizes. The differential in refractive indices of the two phases gives rise to an increased scattering component for the low-temperature phase that is reflected as a negative ΔT_{lum} value in Table II. 1; accordingly, there is no significant change in magnitude as a result of nanocrystal loading for either of these two samples. From a practical perspective, the negative term strongly effects the overall full-spectrum T_{sol} performance values (Table II. 1), effectively negating any gains in energy efficiency derived from ΔT_{NIR} given the higher weighting of the visible region in the AM1.5 spectrum. The second and third observations related to a decrease in overall transmission and increase in NIR modulation between samples A and I go hand-in-hand, and return to the intrinsic trade-off of VO_2-based thermochromic fenestration elements: increasing the loading of VO_2 increases the NIR modulation but also decreases visible transmission. In this comparison, the amount of VO_2 within a given loading is constant but owing to the substantial change in morphology (thick nanowires as compared to thin ribbons) between samples, the absorption

cross-section is much higher for the ribbon-like sample A (note the lack of additional light scattering, as delineated by similar ΔT_{lum} values in Table II. 1). While this effect is not drastic from a numerical performance standpoint, the observation does highlight an additional morphology effect not accounted for in the above theoretical models. The final observation is the 280—350 nm blue-shift of the NIR modulation onset wavelength between samples A and I (Table II. 1). The inflection between high- and low-temperature spectra for samples I and A are observed at ca. 1660 nm and 1380 nm, respectively. The shift to shorter wavelengths is a result of smaller Mie scattering contributions as a result of the reduced size of the nanowires in sample A. These modulation onsets are clearly unviable for fenestration applications since the solar flux beyond this wavelength is minimal.

The rather poor performance metrics of sample I and A is explicable based on the simulations in Figure II. 1. The low T_{lum} and ΔT_{NIR} values, coupled with long-wavelength NIR modulation onsets clearly indicate a size-dependent light scattering mechanism. Mie scattering in the visible-NIR region becomes significant when the diameter of the particle is comparable to or greater than the wavelength of the interacting photon resulting in a scattering in the forward direction. With this in mind, we have examined I-BM and NS samples that have particle dimensions well below the 400—2500 nm range of the visible-NIR spectrum (Fig. II. 4C and D). Notably, the I-BM sample displays a substantial improvement in ΔT_{NIR}; however, the ΔT_{sol} values are still offset by a significant negative ΔT_{lum} component (Table II. 1). Interestingly, the amount of light scattering in the visible region of the electromagnetic spectrum, characterized by ΔT_{lum}, is significantly larger than that of the I and A samples. In contrast, the NS samples do not exhibit a scattering background. A significant increase in T_{lum} along with a substantial enhancement of ΔT_{NIR} is deduced from the spectra of the NS nanocrystals (Figure II. 4D) and is clearly

manifested in the performance metrics enumerated in Table II. 1. These samples exhibit ΔT_{NIR} values as high as 32.18% with ΔT_{sol} values greater than 16% at high loadings. The improved visible light transmittance can be attributed to the reduction of Mie scattering, whereas the improved ΔT_{NIR} performance can be traced to the formation of a localized-surface plasmon resonance (LSPR) with a maximum absorbance between 1200—1400 nm for particles sub-100 nm in size. The LSPR wavelength is advantageous for thermochromic fenestration purposes as the onset of the resonance begins close to the visible/NIR crossover point in the solar spectrum. A fraction of the I-BM nanocrystals are also expected to be within the size regime wherein LSPR formation is expected.[70] However, the NIR onset for I-BM samples is deep in the NIR region of the electromagnetic spectrum, which in conjunction with low T_{lum} values comparable to I and A samples and a significantly increased ΔT_{lum} suggests an "effective" particle-size-dependent scattering mechanism is manifested owing to the agglomeration of the I-BM nanocrystals to form larger particles.

Specular transmission data shown in Figure 4 provides vital optical performance metrics but provide limited mechanistic insight into optical processes such as scattering, reflection, and absorption within the nanocomposite films that underpin these metrics since all of these parameters are incorporated within the measurement of a singular intensity value at each wavelength. In order to derive deeper mechanistic understanding of the optical processes within nanocomposite thin films, absorptance (A) and diffuse transmission (T_{diff}) spectra have been acquired for I-BM and NS samples and are depicted in **Figure II. 5** where A is defined in **Equation II. 3** as

$$A = 100 - T_{tot} - R_{tot} \qquad \text{(II. 3)}$$

and **Equation II. 4** as

$$T_{tot} = T_{spec} + T_{diff} \qquad \text{(II. 4)}$$

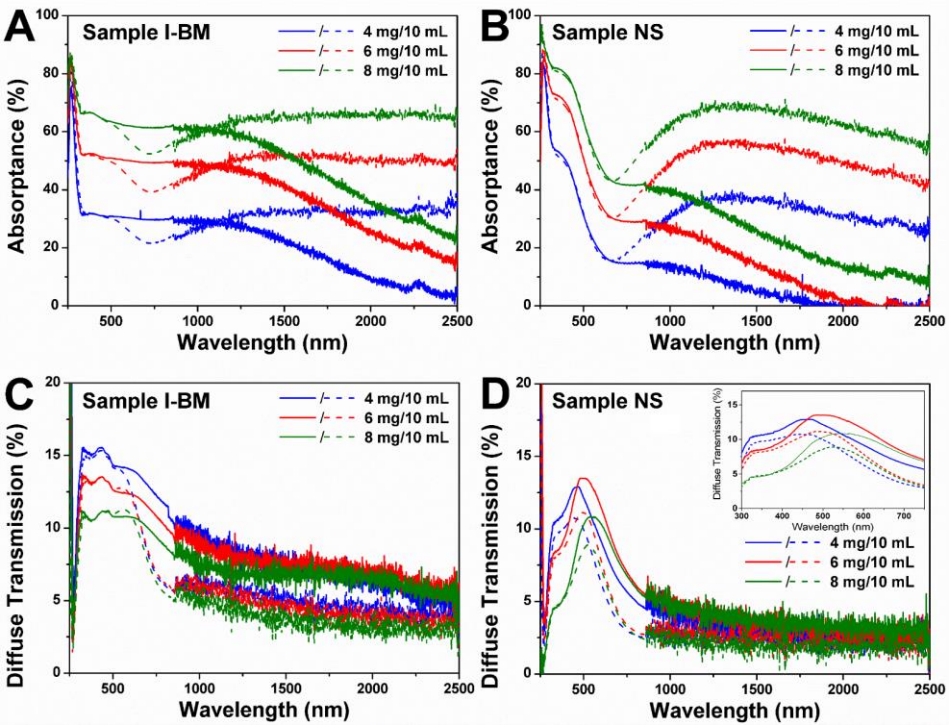

Figure II. 5 Vis-NIR Absorptance (A, B) and diffuse transmission (C, D) spectra for nanocomposite VO_2@SiO_2/ MAA-EA nanocomposite films prepared from dispersions at nanocrystal loadings of 4 mg/10 mL (blue lines), 6 mg/10 mL (red lines), and 8 mg/10 mL VO_2 (green lines). In each case, the solid lines represent acquired at 35°C, whereas dotted lines represent spectra acquired at 85°C after equilibration for 10 min. (A, C) Sample I-BM; and (B, D) Sample NS. The inset in (D) magnifies the 300—750 nm region highlighting the systematic red-shift of the band maximum with VO_2 loading of the displayed spectra.

where T_{tot} is the total transmission and R_{tot} is the total reflection collected using an integrating-sphere-based spectrometer.

Absorptance of the films increase with higher loadings for both I-BM and NS samples but with very different spectral shapes. In the low-temperature phase, absorptance of I-BM is broad and featureless throughout the visible region of the electromagnetic spectrum before decreasing beyond 1500 nm, whereas in contrast, the NS sample has two defined absorption bands. The high-energy absorption is assigned to the O 2p $\pi \rightarrow \pi^*$ interband transition, whereas the weaker low-energy absorption is assigned to the $d_{\parallel} \rightarrow \pi^*$ bandgap transition as described by Goodenough's simplified model of the band structure of VO_2.[71] In the high-temperature phase, when the bandgap is closed, the absorption across the O 2p transition is still observed but a pronounced LSPR dominates the NIR region of the electromagnetic spectrum. For NS samples the modulation in NIR absorptance between low and high temperature films is clearly centered at the inflection point between the two absorption bands. Such is not the case for I-BM samples. Interpretation of the absorptance spectra for NS samples is straightforward with the NIR modulation derived from the appearance of the LSPR absorption upon closing of the bandgap. For I-BM samples, spectra for low-temperature films deviate between 600—1000 nm, absorbing broadly across the inflection point between O 2p $\pi \rightarrow \pi^*$ interband and $d_{\parallel} \rightarrow \pi^*$ bandgap transitions. We can conclude that in the low-temperature phase, significant internal light scattering within the film, arising from clustering of crystallites within larger agglomerates, facilitates a broad absorption in 600—1000 nm region. This broad absorption accounts for the NIR modulation onset beyond 1000 nm and further diminishes any LSPR-related ΔT_{NIR}.

We investigate light scattering profiles in the I-BM and NS samples further with diffuse transmission (Figs. II. 5C and D). Interestingly, for both samples the intensity of the scattering bands are not significantly different (< 5%); however, clear differences are observed in the spectral lineshapes and change in T_{diff} with temperature. For NS samples, which are

homogeneous in terms of their dimensions and nature of encapsulation by a SiO_2 shell, clear spectrally-resolved bands appear in the visible region and are diminished in the NIR region of the electromagnetic spectrum (Figure II. 5D). In fact, the observed scattering bands are remarkably close to those theoretically predicted for homogeneous spherical particles.[70,72,73] Scattering intensity in the low temperature phase is greater and slightly red-shifted than the high temperature phase; both attributes are explicable considering the differential in *n* between the MAA-EA copolymer host matrix and the M1 VO_2 phase as compared to the R phase. T_{diff} measurements exhibit a clear red-shift of the scattering bands with increasing $VO_2@SiO_2$ loading concordant with predictions of size-dependent shifts (inset to Figure II. 5D).[73] Since the crystallite size remains constant as a function of nanocrystal loading, the observed red-shift is attributed to an increasing "effective" particle size as a result of the agglomeration of nanocrystals to form larger particles within the MAA-EA matrix. In contrast, no discernible red-shift is observed for low-temperature I-BM samples; instead the scattering is broader and less defined in the visible and extends well into the NIR. The magnitude of scattering between 600—1000 nm is in good agreement with the associated absorptance spectra (Figures II 5A and 4C), signifying that the internal scattering is derived largely from the mismatch in refractive index. Given the extensive agglomeration of I- BM VO_2 particles during encapsulation with SiO_2, multiple VO_2 nanocrystals are likely incorporated in close proximity within a heterogeneous SiO_2 shell. Such heterogeneous agglomeration likely accounts for the large gradient of *n* scattering in these samples and gives rise to the broad scattering signal.

Comparison of the absorptance and diffuse transmission spectra of the two samples highlight the significant impact that relatively subtle changes in disparate light scattering mechanisms (correlated directly or indirectly to size and size heterogeneity) can have on the

optical performance of nanocomposite films. Consequently, mitigating the disparate light scattering mechanisms within these nanocomposite films requires not just control of particle size to avoid Mie scattering but also homogeneity of the refractive-index matching layer and individual dispersion of VO_2@SiO_2 nanocrystals within the host matrix.[74] **Figure II. 6** provides a visualization of the onset of NIR modulation, visible light transmittance, and NIR modulation

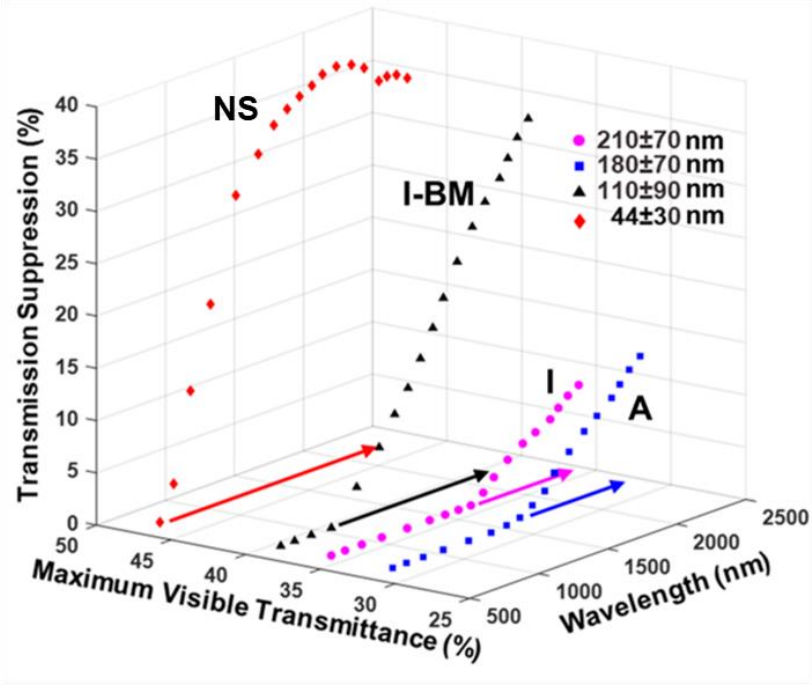

Figure II. 6 Three-dimensional visualization of NIR modulation and visible light transmittance plotted as a function of wavelength for the four sets of samples; I (purple spheres), A (blue squares), I-BM (black triangles), and NS (red diamonds). All samples shown here correspond to a concentration of 0.8 mg VO_2@SiO_2/10 mL dispersion. The maximum visible transmittance is the maxima in the visible region from each 8 mg/10 mL 85°C plot in Figure 4 and is constant for each plot (represented by an arrow across the maximum visible transmittance/wavelength plane).

for the four nanocrystal dimensions at the same loading.

As discussed above, the NS samples have the smallest dimensions (44±30 nm) and clearly show much greater visible light transmittance as compared to the I, I-BM, and A samples as a

result of a reduced scattering background. The NS samples with the smallest nanocrystal dimensions exhibit the best combination of high NIR modulation and visible light transmittance (see also Table II. 1). The onset of NIR modulation at relatively shorter wavelengths implies the ability to dynamically adjust transmittance for a relatively greater region of the solar spectrum.[75] For the three samples I, I-BM, and A, the onset of NIR modulation does not begin until further into the NIR, ca. 1660 nm for sample I, 1380 nm for sample A, and ca. 1150—1200 nm for I-BM. In contrast, for the NS samples, the onset of the drop is blue-shifted to ca. 740—750 nm, partly due to the appearance of LSPR band. Notably, NIR modulation below 700 nm is not desirable since that will bring about a pronounced change of the visible appearance of the film. Figure 6 thus clearly indicates the vastly greater visible light transmittance and higher NIR modulation observed for the NS sample wherein light scattering is considerably mitigated as a result of the optimal nanocrystal dimensions, refractive index matching, and dispersion. A NIR modulation of as much as 32.18% is accessible within these nanocomposite films, which results in a total dynamical modulation of transmitted light approaching 16.62%. The optical performance of our NS samples is indeed comparable to other recently reported values for VO_2 composite films where considerable effort has been made to reduce light scattering.[44,45,70,76–78] Zhang *et al*.[45] and Miao *et al*.[70] reduced Mie scattering by decreasing the as-synthesized VO_2 particle size through grinding or ball-milling treatments and achieved a T_{lum} of 62.1% with ΔT_{sol} of 12.4% and a T_{lum} of 38.5% with ΔT_{sol} of 16.9%, respectively. Guo *et al*. have prepared ultrafine VO_2 nanoparticles using a unique one-step hydrothermal reaction in a self-released oxidizing atmosphere at relatively low temperatures and reported a T_{lum} of 54.26%. and a ΔT_{sol} of 12.34%.[76] As one of best-in-class examples, Chen *et al*. have reported a 31.1% increase (from 38.9% to 51.0%) in T_{lum} and an 11.0% increase (from 17.2% to 19.1%) in ΔT_{sol} upon encapsulation of VO_2 nanospheres within a ZnO

shell.[44] Clear understanding and subsequent mitigation of light scattering mechanisms is of paramount importance to approach the limits of theoretically predicted performance.

In order to examine the dynamical behavior of the nanocomposite thin films, a time-dependent transmission experiment has been performed for nanocomposite thin films incorporating VO_2 NS and is shown in **Figure II. 7**. The temperature of the film has been ramped from room temperature to 73°C and spectra have been acquired from 1250 nm to 1430 nm as a

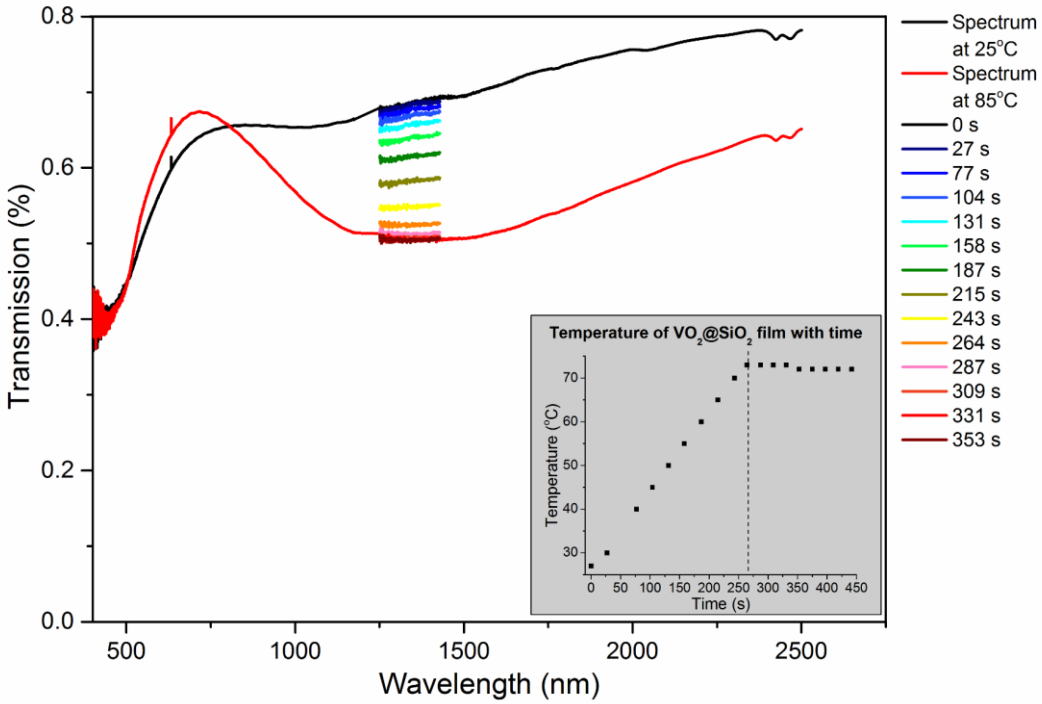

Figure II. 7 Vis-NIR transmission spectra acquired as a function of time during heating for a VO_2@SiO_2 methacrylic acid/ethyl acrylate copolymer thin film prepared from dispersions of VO_2 NS at loadings of 5 mg/10 mL. Full spectra are acquired before heating at 25°C (black line) and after heating at 85°C (red line) upon temperature equilibration for 10 min. The inset plots the temperature of the film as a function of elapsed time. The temperature is increased at a rate of 0.2°C/s.

function of time. The temperature values have been selected based on the differential scanning calorimetry (DSC) trace shown in Figure A 1. At each time interval, the temperature of the film is

read using an internal temperature sensor, as shown in the inset to Figure II. 7. The transmission data shows that the transmission of the sample decreases drastically between 104 s and 287 s (corresponding to film temperatures of 40°C and 73°C, respectively) and is constant thereafter. The maximum decrease in transmission at an elapsed time of 287 s is within 25 s of the internal film temperature reaching 73°C (marked with a dotted line in the inset). This indicates that the switching response time of the NS VO_2@SiO_2 nanocomposite films is well captured by the equilibration steps.[79] Video A. 1 shows the discernible change in the NIR transmittance of a NS nanocomposite VO_2@SiO_2 methacrylic acid/ethyl acrylate copolymer thin film being heated from room temperature with a heat gun acquired using a NIR-enabled camera under solar irradiation. The substantial NIR opacity observed stands in stark contrast to the high visible light transmittance observed in Figure A 4F. A 850 nm longpass filter has been mounted on the camera to exclude shorter wavelengths. The sensitivity range of the camera is between 850 nm and 1000 nm owing to the combination of longpass filter and spectral response of the CMOS sensor of the camera. The speed of Video A. 1 has been digitally increased by a factor of ca. 11; upon reaching the transition temperature, the film is observed to transform within a few seconds. These measurements suggests that the films entirely transform within a few seconds of reaching the transition temperatures with the elapsed time likely reflecting the time taken for the nanocrystals to reach the transition temperature given the poor thermal conductivity of the polymeric matrix. The measurements suggest a transformation timescale well equipped to handle diurnal variations when embedded as fenestration elements in the built environment.

II.4 Conclusion

In conclusion, thermochromic modulation of near-infrared solar flux represents an attractive route for controlling solar heat gain based on the ambient temperature without deleteriously impacting the visible light transmittance of fenestration units. The pronounced near-room-temperature metal—insulator transition of VO_2 provides a means to modulate solar heat gain in a spectrally selective manner. Nanocrystals provide distinct advantages over continuous thin films in being able to better accommodate strains arising from thermal cycling and in affording a higher visible light transmittance, mitigating the thermal-cycling-induced pulverization of large crystals.[80,81] However, the use of nanocrystals requires elucidation of optimal crystallite dimensions, refractive index matching, and the appropriate dispersion of the nanocrystals within a low-refractive-index medium. EMM and FEA+GO optical simulations indicate a pronounced size dependence of the visible light transmittance for VO_2 nanocomposite thin films. Four different sizes of VO_2@SiO_2 nanocrystals have been synthesized and contrasted for thermochromic modulation and visible light transmittance after dispersion in an aqueous acrylate system and solution casting onto glass substrates. For larger nanocrystal sizes as well as agglomerations of smaller particles, dynamical modulation is diminished as a result of Mie scattering from both large individual crystallites and their agglomerations; refractive index mismatch between the low-and high-temperature phases of VO_2 and the host polymer matrix; and the appearance of a LSPR band. The interplay between the fundamental scattering mechanisms have been examined in detail using temperature-variant absorptance and diffuse transmittance measurements of the different particles sizes performed as a function of nanocrystal loading in the polymeric medium. The smallest particle dimensions (44±30 nm, Sample NS) appear to provide the best combination of visible light transmittance and NIR

modulation (blocking up to ca. 16.62% of total solar energy and 32.18% of energy in the NIR) with an onset of NIR modulation in the range of 740—750 nm. This latter system provides a pathway towards the preparation of viable thermochromic elements, founded on detailed mechanistic elucidation of the multiple scattering mechanisms that need to be mitigated for deployment at scale. Future work will focus on optimization of the shell used for refractive index matching, surface functionalization to facilitate dispersion in the polymeric medium and enhance longevity of the nanocrystals, and selection of a high-visible-light transparency dispersion medium. The inclusion of substitutional and interstitial dopants will furthermore be utilized through modification of hydrothermal synthetic methods or post-synthetic modification to prepare nanocomposite thin films with transition temperatures designed to match the requirements of specific climate zones.[29,60]

II.5 References

(1) Houvilla, P. *Buildings and Climate Change: Status, Challenges and Opportunities*; United Nation Environment Programme, **2007**; pp 1− 88.

(2) *Energy Efficiency Trends in Residential and Commercial Buildings*; U.S. Department of Energy, **2008**; pp 1−31.

(3) U.S. Energy Information Administration. How Much Energy Is Consumed in U.S. Residential and Commercial Buildings?, 2018. https://www.eia.gov/tools/faqs/faq.php?id=86&t=1 (accessed Sept 9, 2018).

(4) Kanu, S. S.; Binions, R. Thin Films for Solar Control Applications. *Proc. R. Soc. A Math. Phys. Eng. Sci.* **2010**, *466*, 19–44.

(5) Granqvist, C. G. Electrochromic Materials: Out of a Niche. *Nat. Mater.* **2006**, *5*, 89–90.

(6) Shehabi, A.; DeForest, N.; McNeil, A.; Masanet, E.; Greenblatt, J.; Lee, E. S.; Masson, G.; Helms, B. A.; Milliron, D. J. U.S. Energy Savings Potential from Dynamic Daylighting Control Glazings. *Energy Build.* **2013**, *66*, 415–423.

(7) Llordés, A.; Garcia, G.; Gazquez, J.; Milliron, D. J. Tunable Near-Infrared and Visible-Light Transmittance in Nanocrystal-in-Glass Composites. *Nature* **2013**, *500*, 323–326.

(8) Manning, T. D.; Parkin, I. P.; Pemble, M. E.; Sheel, D.; Vernardou, D. Intelligent Window Coatings: Atmospheric Pressure Chemical Vapor Deposition of Tungsten-Doped Vanadium Dioxide. *Chem. Mater.* **2004**, *16*, 744–749.

(9) Parkin, I. P.; Manning, T. D. Intelligent Thermochromic Windows. *J. Chem. Educ.* **2006**, *83*, 393–400.

(10) Costanzo, V.; Evola, G.; Marletta, L. Thermal and Visual Performance of Real and Theoretical Thermochromic Glazing Solutions for Office Buildings. *Sol. Energy Mater. Sol. Cells* **2016**, *149*, 110–120.

(11) ASTM. *Standard Tables for Reference Solar Spectral Irradiances: Direct Normal and Hemispherical on 37° Tilted Surface*; ASTM: West Conshohocken, PA, 2013; Vol. 3, pp 1−21.

(12) Chernova, N. A.; Roppolo, M.; Dillon, A. C.; Whittingham, M. S. Layered Vanadium and Molybdenum Oxides: Batteries and Electrochromics. *J. Mater. Chem.* **2009**, *19*, 2526.

(13) Deb, S. K. Physical Properties of a Transition Metal Oxide: Optical and Photoelectric Properties of Single Crystal and Thin Film Molybdenum Trioxide. *Proc. R. Soc. A Math. Phys. Eng. Sci.* **1968**, *304*, 211–231.

(14) Marley, P. M.; Horrocks, G. A.; Pelcher, K. E.; Banerjee, S. Transformers: The Changing Phases of Low-Dimensional Vanadium Oxide Bronzes. *Chem. Commun.* **2015**, *51*, 5181–

5198.

(15) Zhou, Y.; Ramanathan, S. Correlated Electron Materials and Field Effect Transistors for Logic: A Review. *Crit. Rev. Solid State Mater. Sci.* **2013**, *38*, 286–317.

(16) Hudak, B. M.; Depner, S. W.; Waetzig, G. R.; Talapatra, A.; Arroyave, R.; Banerjee, S.; Guiton, B. S. Real-Time Atomistic Observation of Structural Phase Transformations in Individual Hafnia Nanorods. *Nat. Commun.* **2017**, *8*, 15316.

(17) Wu, C.; Feng, F.; Xie, Y. Design of Vanadium Oxide Structures with Controllable Electrical Properties for Energy Applications. *Chem. Soc. Rev.* **2013**, *42*, 5157–5183.

(18) Monceau, P. Electronic Crystals: An Experimental Overview. *Adv. Phys.* **2012**, *61*, 325–581.

(19) Imada, M.; Fujimori, A.; Tokura, Y. Metal-Insulator Transitions. *Rev. Mod. Phys.* **1998**, *70*, 1039–1263.

(20) Yang, Z.; Ko, C.; Ramanathan, S. Oxide Electronics Utilizing Ultrafast Metal-Insulator Transitions. *Annu. Rev. Mater. Res.* **2011**, *41*, 337–367.

(21) Patridge, C. J.; Wu, T.-L.; Sambandamurthy, G.; Banerjee, S. Colossal Above-Room-Temperature Metal–insulator Switching of a Wadsley-Type Tunnel Bronze. *Chem. Commun.* **2011**, *47*, 4484.

(22) Edwards, P. P.; Sienko, M. J. Universality Aspects of the Metal-Nonmetal Transition in Condensed Media. *Phys. Rev. B Solid State* **1978**, *17*, 2575–2581.

(23) Edwards, P. P.; Ramakrishnan, T. V; Rao, C. N. R. The Metal-Nonmetal Transition: A Global Perspective. *J. Phys. Chem.* **1995**, *99*, 5228–5239.

(24) Patridge, C. J.; Wu, T. L.; Jaye, C.; Ravel, B.; Takeuchi, E. S.; Fischer, D. A.; Sambandamurthy, G.; Banerjee, S. Synthesis, Spectroscopic Characterization, and

Observation of Massive Metal-Insulator Transitions in Nanowires of a Nonstoichiometric Vanadium Oxide Bronze. *Nano Lett.* **2010**, *10*, 2448–2453.

(25) Adler, D. Mechanisms for Metal-Nonmental Transitions in Transition-Metal Oxides and Sulfides. *Rev. Mod. Phys.* **1968**, *40*, 714–736.

(26) Whittaker, L.; Patridge, C. J.; Banerjee, S. Microscopic and Nanoscale Perspective of the Metal−Insulator Phase Transitions of VO_2: Some New Twists to an Old Tale. *J. Phys. Chem. Lett.* **2011**, *2*, 745–758.

(27) Whittaker, L.; Wu, T.-L.; Patridge, C. J.; Sambandamurthy, G.; Banerjee, S. Distinctive Finite Size Effects on the Phase Diagram and Metal–insulator Transitions of Tungsten-Doped Vanadium(IV) Oxide. *J. Mater. Chem.* **2011**, *21*, 5580.

(28) Morin, F. J. Oxides Which Show a Metal-to-Insulator Transition at the Neel Temperature. *Phys. Rev. Lett.* **1959**, *3*, 34–36.

(29) Alivio, T. E. G.; Sellers, D. G.; Asayesh-Ardakani, H.; Braham, E. J.; Horrocks, G. A.; Pelcher, K. E.; Villareal, R.; Zuin, L.; Shamberger, P. J.; Arroyave, R.; et al. Postsynthetic Route for Modifying the Metal — Insulator Transition of VO_2 by Interstitial Dopant Incorporation. *Chem. Mater* **2017**, *29*, 5401–5412.

(30) Wei, J.; Ji, H.; Guo, W.; Nevidomskyy, A. H.; Natelson, D. Hydrogen Stabilization of Metallic Vanadium Dioxide in Single-Crystal Nanobeams. *Nat. Nanotechnol.* **2012**, *7*, 357–362.

(31) Chen, Z.; Gao, Y.; Kang, L.; Cao, C.; Chen, S.; Luo, H. Fine Crystalline VO_2 Nanoparticles: Synthesis, Abnormal Phase Transition Temperatures and Excellent Optical Properties of a Derived VO_2 Nanocomposite Foil. *J. Mater. Chem. A* **2014**, *2*, 2718–2727.

(32) Ji, S.; Zhang, F.; Jin, P. Preparation of High Performance Pure Single Phase VO_2

Nanopowder by Hydrothermally Reducing the V 2O 5 Gel. *Sol. Energy Mater. Sol. Cells* **2011**, *95*, 3520–3526.

(33) Batista, C.; Ribeiro, R. M.; Teixeira, V. Synthesis and Characterization of VO_2-Based Thermochromic Thin Films for Energy-Efficient Windows. *Nanoscale Res. Lett.* **2011**, *6*, 301.

(34) Liu, W.-T.; Cao, J.; Fan, W.; Hao, Z.; Martin, M. C.; Shen, Y. R.; Wu, J.; Wang, F. Intrinsic Optical Properties of Vanadium Dioxide near the Insulator-Metal Transition. *Nano Lett.* **2011**, *11*, 466–470.

(35) Jones, A. C.; Berweger, S.; Wei, J.; Cobden, D.; Raschke, M. B. Nano-Optical Investigations of the Metal-Insulator Phase Behavior of Individual VO_2 Microcrystals. *Nano Lett.* **2010**, *10*, 1574–1581.

(36) Chen, X.; Lv, Q.; Yi, X. Smart Window Coating Based on Nanostructured VO_2 Thin Film. *Opt. - Int. J. Light Electron Opt.* **2012**, *123*, 1187–1189.

(37) Zhang, P.; Li, M.; Deng, Q.; Zhang, J.; Wu, J.; Hu, Z.; Chu, J. Spectral Assignments in the Infrared Absorption Region and Anomalous Thermal Hysteresis in the Interband Electronic Transition of Vanadium Dioxide Films. *Phys. Chem. Chem. Phys.* **2016**, *18*, 6239–6246.

(38) Charipar, N. A.; Kim, H.; Breckenfeld, E.; Charipar, K. M.; Mathews, S. A.; Piqué, A. Polycrystalline VO_2 Thin Films via Femtosecond Laser Processing of Amorphous VO_X. *Appl. Phys. A Mater. Sci. Process.* **2016**, *122*, 512.

(39) Louloudakis, D.; Vernardou, D.; Spanakis, E.; Katsarakis, N.; Koudoumas, E. Thermochromic Vanadium Oxide Coatings Grown by APCVD at Low Temperatures. *Phys. Procedia* **2013**, *46*, 137–141.

(40) Zhou, J.; Gao, Y.; Zhang, Z.; Luo, H.; Cao, C.; Chen, Z.; Dai, L.; Liu, X. VO_2 Thermochromic Smart Window for Energy Savings and Generation. *Sci. Rep.* **2013**, *3*, 3029.

(41) Clavero, C.; Slack, J. L.; Anders, A. Size and Composition-Controlled Fabrication of Thermochromic Metal Oxide Nanocrystals. *J. Phys. D. Appl. Phys.* **2013**, *46*, 362001.

(42) Li, W.; Ji, S.; Li, Y.; Huang, A.; Luo, H.; Jin, P. Synthesis of VO_2 Nanoparticles by Hydrothermal-Assisted Homogeneous Precipitation Approach for Thermochromic Applications. *RSC Adv.* **2014**, *4*, 13026–13033.

(43) Madida, I. G.; Simo, A.; Sone, B.; Maity, A.; Kana Kana, J. B.; Gibaud, A.; Merad, G.; Thema, F. T.; Maaza, M. Submicronic VO_2-PVP Composites Coatings for Smart Windows Applications and Solar Heat Management. *Sol. Energy* **2014**, *107*, 758–769.

(44) Chen, Y.; Zeng, X.; Zhu, J.; Li, R.; Yao, H.; Cao, X.; Ji, S.; Jin, P. High Performance and Enhanced Durability of Thermochromic Films Using VO_2@ZnO Core-Shell Nanoparticles. *ACS Appl. Mater. Interfaces* **2017**, *9*, 27784–27791.

(45) Zhang, H.; Xiao, X.; Lu, X.; Chai, G.; Sun, Y.; Zhan, Y.; Xu, G. A Cost-Effective Method to Fabricate VO_2(M) Nanoparticles and Films with Excellent Thermochromic Properties. *J. Alloys Compd.* **2015**, *636*, 106–112.

(46) Horrocks, G. A.; Singh, S.; Likely, M. F.; Sambandamurthy, G.; Banerjee, S. Scalable Hydrothermal Synthesis of Free-Standing VO_2 Nanowires in the M1 Phase. *ACS Appl. Mater. Interfaces* **2014**, *6*, 15726–15732.

(47) Whittaker, L.; Zhang, H.; Banerjee, S. VO2 Nanosheets Exhibiting a Well-Defined Metal–insulator Phase Transition. *J. Mater. Chem.* **2009**, *19*, 2968–2974.

(48) Pelcher, K. E.; Crawley, M. R.; Banerjee, S. Silica-Shell Encapsulation and Adhesion of

VO_2 Nanowires to Glass Substrates: Integrating Solution-Derived VO_2 Nanowires within Thermally Responsive Coatings. *Mater. Res. Express* **2014**, *1*, 035014.

(49) Xiao, X.; Zhang, H.; Chai, G.; Sun, Y.; Yang, T.; Cheng, H.; Chen, L.; Miao, L.; Xu, G. A Cost-Effective Process to Prepare VO_2 (M) Powder and Films with Superior Thermochromic Properties. *Mater. Res. Bull.* **2014**, *51*, 6–12.

(50) Yue, F.; Huang, W.; Shi, Q.; Li, D.; Hu, Y.; Xiao, Y.; Deng, X.; Wang, C. Phase Transition Properties of Vanadium Oxide Films Deposited by Polymer-Assisted Deposition. *J. Sol-Gel Sci. Technol.* **2014**, *72*, 565–570.

(51) Naoi, Y.; Amano, J. Optimization of VO_2 Nanowire Polymer Composite Thermochromic Films by Optical Simulation. *J. Appl. Phys.* **2016**, *120*, 235301.

(52) Li, W.; Ji, S.; Qian, K.; Jin, P. Preparation and Characterization of VO_2-$BaSO_4$ Composite Films with Enhanced Optical Properties in Thermochromic Field. *Ceram. Int.* **2015**, *41*, 5049–5056.

(53) Zhu, J.; Zhou, Y.; Wang, B.; Zheng, J.; Ji, S.; Yao, H.; Luo, H.; Jin, P. Vanadium Dioxide Nanoparticle-Based Thermochromic Smart Coating: High Luminous Transmittance, Excellent Solar Regulation Efficiency, and Near Room Temperature Phase Transition. *ACS Appl. Mater. Interfaces* **2015**, *7*, 27796–27803.

(54) Fleer, N. A.; Pelcher, K. E.; Zou, J.; Nieto, K.; Douglas, L. D.; Sellers, D. G.; Banerjee, S. Hybrid Nanocomposite Films Comprising Dispersed VO_2 Nanocrystals: A Scalable Aqueous-Phase Route to Thermochromic Fenestration. *ACS Appl. Mater. Interfaces* **2017**, *9*, 38887–38900.

(55) Liu, C.; Balin, I.; Magdassi, S.; Abdulhalim, I.; Long, Y. Vanadium Dioxide Nanogrid Films for High Transparency Smart Architectural Window Applications. *Opt. Express*

2015, *23*, A124.

(56) Li, S. Y.; Niklasson, G. A.; Granqvist, C. G. Nanothermochromics with VO_2-Based Core-Shell Structures: Calculated Luminous and Solar Optical Properties. *J. Appl. Phys.* **2011**, *109*, 113515.

(57) Kang, L.; Gao, Y.; Luo, H.; Chen, Z.; Du, J.; Zhang, Z. Nanoporous Thermochromic VO_2 Films with Low Optical Constants, Enhanced Luminous Transmittance and Thermochromic Properties. *ACS Appl. Mater. Interfaces* **2011**, *3*, 135–138.

(58) Li, S. Y.; Niklasson, G. A.; Granqvist, C. G. Nanothermochromics: Calculations for VO_2 Nanoparticles in Dielectric Hosts Show Much Improved Luminous Transmittance and Solar Energy Transmittance Modulation. *J. Appl. Phys.* **2010**, *108*, 063525.

(59) Qazilbash, M. M.; Brehm, M.; Chae, B.-G.; Ho, P.-C.; Andreev, G. O.; Kim, B.-J.; Yun, S. J.; Balatsky, A. V; Maple, M. B.; Keilmann, F.; et al. Mott Transition in VO_2 Revealed by Infrared Spectroscopy and Nano-Imaging. *Science.* **2007**, *318*, 1750–1753.

(60) Kango, S.; Kalia, S.; Celli, A.; Njuguna, J.; Habibi, Y.; Kumar, R. Surface Modification of Inorganic Nanoparticles for Development of Organic-Inorganic Nanocomposites - A Review. *Prog. Polym. Sci.* **2013**, *38*, 1232–1261.

(61) Physical Constants of Organic Constants. In *CRC Handbook of Chemistry and Physics*, 93rd ed.; Haynes, W. M.; Lide, D. R.; Bruno, T. J., Eds.; Taylor & Francis Group: Boca Raton, FL, 2011; pp 1−523.

(62) Kana Kana, J. B.; Ndjaka, J. M.; Vignaud, G.; Gibaud, A.; Maaza, M. Thermally Tunable Optical Constants of Vanadium Dioxide Thin Films Measured by Spectroscopic Ellipsometry. *Opt. Commun.* **2011**, *284*, 807–812.

(63) Kakiuchida, H.; Jin, P.; Nakao, S.; Tazawa, M. Optical Properties of Vanadium Dioxide

Film during Semiconductive–Metallic Phase Transition. *Jpn. J. Appl. Phys.* **2007**, *46*, L113–L116.

(64) Braham, E. J.; Sellers, D.; Emmons, E.; Villarreal, R.; Asayesh-Ardakani, H.; Fleer, N. A.; Farley, K. E.; Shahbazian-Yassar, R.; Arròyave, R.; Shamberger, P. J.; et al. Modulating the Hysteresis of an Electronic Transition: Launching Alternative Transformation Pathways in the Metal–Insulator Transition of Vanadium(IV) Oxide. *Chem. Mater.* **2018**, *30*, 214–224.

(65) Whittaker, L.; Jaye, C.; Fu, Z.; Fischer, D. A.; Banerjee, S. Depressed Phase Transition in Solution-Grown VO_2 Nanostructures. *J. Am. Chem. Soc.* **2009**, *131*, 8884–8894.

(66) Li, M.; Magdassi, S.; Gao, Y.; Long, Y. Hydrothermal Synthesis of VO_2 Polymorphs: Advantages, Challenges and Prospects for the Application of Energy Efficient Smart Windows. *Small*. 2017, p 1701147.

(67) Maaza, M.; Nemraoui, O.; Sella, C.; Beye, A. C.; Box, P. O.; Africa, S.; Pierre, U.; Curie, M.; Vi, P.; Cedex, P. Surface Plasmon Resonance Thermochromic Nano-Composites. *Gold Bull.* **2005**, *38*, 100–106.

(68) Hebert, K. J.; Zafar, S.; Irene, E. A.; Kuehn, R.; McCarthy, T. E.; Demirlioglu, E. K. Measurement of the Refractive Index of Thin SiO_2 Films Using Tunneling Current Oscillations and Ellipsometry. *Appl. Phys. Lett.* **1996**, *68*, 266–268.

(69) Sharma, A.; Smith, J. D.; Walters, K. B.; Rick, S. W. Constant PH Simulations of PH Responsive Polymers. *J. Chem. Phys.* **2016**, *145*, 234906.

(70) Miao, L.; Chen, R.; Zhou, J.; Liu, C.; Peng, Y.; Gao, J.; Sun, L.; Tanemura, S. Depressed Haze and Enhanced Solar Modulation Capability for VO_2-Based Composite Films with Distinct Size Effects. *RSC Adv.* **2016**, *6*, 90813–90823.

(71) Goodenough, J. B. The Two Components of the Crystallographic Transition in VO_2. *J. Solid State Chem.* **1971**, *3*, 490–500.

(72) Lopez, R.; Feldman, L. C.; Haglund, R. F. Size-Dependent Optical Properties of VO_2 Nanoparticle Arrays. *Phys. Rev. Lett.* **2004**, *93*, 177403.

(73) Montero, J.; Ji, Y.-X.; Granqvist, C. G.; Niklasson, G. A. Thermochromic Light Scattering from Particulate VO_2 Layers. *J. Appl. Phys.* **2016**, *119*, 85302.

(74) Dennis, R. V; Patil, V.; Andrews, J. L.; Aldinger, J. P.; Yadav, G. D.; Banerjee, S. Hybrid Nanostructured Coatings for Corrosion Protection of Base Metals: A Sustainability Perspective. *Mater. Res. Express* **2015**, *2*, 032001.

(75) Bird, R. E.; Hulstrom, R. L.; Lewis, L. J. Terrestrial Solar Spectral Data Sets. *Sol. Energy* **1983**, *30*, 563–573.

(76) Guo, D.; Ling, C.; Wang, C.; Wang, D.; Li, J.; Zhao, Z.; Wang, Z.; Zhao, Y.; Zhang, J.; Jin, H. Hydrothermal One-Step Synthesis of Highly-Dispersed M-Phase VO_2 Nanocrystals and Application to Flexible Thermochromic Film. *ACS Appl. Mater. Interfaces* **2018**.

(77) Cao, Z.; Xiao, X.; Lu, X.; Zhan, Y.; Cheng, H.; Xu, G. A Simple and Low-Cost Combustion Method to Prepare Monoclinic VO_2 with Superior Thermochromic Properties. *Sci. Rep.* **2016**, *6*, 39154.

(78) Wang, M.; Tian, J.; Zhang, H.; Shi, X.; Chen, Z.; Wang, Y.; Ji, A.; Gao, Y. Novel Synthesis of Pure VO_2@SiO_2 Core@shell Nanoparticles to Improve the Optical and Anti-Oxidant Properties of a VO2 Film. *RSC Adv.* **2016**, *6*, 108286–108289.

(79) Rini, M.; Cavalleri, A.; Schoenlein, R. W.; López, R.; Feldman, L. C.; Haglund, R. F.; Boatner, L. A.; Haynes, T. E. Photoinduced Phase Transition in VO_2 Nanocrystals:

Ultrafast Control of Surface-Plasmon Resonance. *Opt. Lett.* **2005**, *30*, 558.

(80) Fisher, B.; Patlagan, L. Switching VO_2 Single Crystals and Related Phenomena: Sliding Domains and Crack Formation. *Materials.* **2017**, *10*, 554.

(81) Abreu, E.; Liu, M.; Lu, J.; West, K. G.; Kittiwatanakul, S.; Yin, W.; Wolf, S. A.; Averitt, R. D. THz Spectroscopy of VO_2 Epitaxial Films: Controlling the Anisotropic Properties through Strain Engineering. *New J. Phys.* **2012**, *14*, 083016.

CHAPTER III

HYBRID NANOCOMPOSITE FILMS COMPRISING DISPERSED VO_2 NANOCRYSTALS: A SCALABLE AQUEOUS-PHASE ROUTE TO THERMOCHROMIC FENESTRATION

III.1 Introduction

Burgeoning construction worldwide, both in the form of residential dwellings and commercial structures, has led to buildings becoming a major source of energy consumption, a trend that has only been accelerated by rapid urbanization in the developing world.[1,2] A recent report from the United Nations estimates that 30—40% of primary energy usage across the world occurs within buildings.[2] In the United States, the Department of Energy estimates that 41% of the total energy consumption occurs within buildings.[3,4] Much of the energy consumed within buildings goes towards space cooling, space heating, lighting, and ventilation. The inability of the built environment to interface with the natural environment in terms of climate control not only leads to increased energy costs, but also incurs a tremendous cost in terms of CO_2 emissions.[1,5] Consequently, the building envelope, the barrier that separates the interior of a building from the exterior environment, is a target area for improvement in order to achieve the ideal of "net zero" buildings. Fenestration elements are a significant venue through which solar irradiance can enter the building and indeed mitigating solar heat gain is the primary objective in the summer or during warm days, whereas in the winter or during cold days, utilizing the solar heat gain to reduce heating costs is desirable.[6–8] Many current technologies aimed at addressing this problem, most of which are coatings and films, suffer from major drawbacks, including a reduction in the transmission of visible light, thereby resulting in increased use of artificial

*Reprinted with permission from "Hybrid Nanocomposite Films Comprising Dispersed VO_2 Nanocrystals: A Scalable Aqueous-Phase Route to Thermochromic Fenestration" by Fleer, N. A.; Pelcher, K. E.; Zou, J.; Nieto, K.; Douglas, L. D.; Sellers, D. G.; Banerjee, S. *ACS Appl. Mater. Interfaces*, **2017**, 9, 38887-38900 © 2017 Amercan Chemical Society. All rights reserved.

lighting. Since these coatings are temperature-invariant in terms of their solar heat gain modulation, they are unable to offset cold-weather heating costs that would otherwise have resulted from solar heat gain. Dynamically switchable temperature- (or voltage)-responsive glazing could play an active role in modulating solar heat gain through fenestration units and indeed numerous electrochromic and thermochromic technologies have been evaluated for this purpose in recent years.[7–13]

The binary vanadium oxide VO_2 is characterized by an abrupt reversible phase transition from an insulator to a metal when heated to ca. 67°C and this phase transition is accompanied by a dramatic modulation of the electrical conductance and optical transmittance.[13–18] The role of electron—electron and electron—phonon interactions in underpinning the dramatic modulation of conductivity observed in this intriguing material continues to be actively debated.[16,19,20] However, some recent findings suggest that the structural and electronic phase transitions can be decoupled both for thermally and optically excited transitions.[19,21–23] The low-temperature insulating phase of VO_2 has a bandgap of ca. 0.6 eV, which is closed upon metallization, resulting in a pronounced spectrally selective suppression of the near-infrared (NIR) transmittance.[19,24,25] Several characteristics of VO_2 make it particularly intriguing for fenestration applications. First, the suppression of transmittance as the material switches from being insulating to metallic is confined primarily to the NIR region of the electromagnetic spectrum and does not involve a substantial modulation of visible light transmittance. In other words, aesthetically unappealing changes in visible light transmittance that can furthermore increase lighting costs are almost entirely mitigated. Secondly, the transition temperature is close to room temperature and can be systematically decreased through scaling to finite size and by the incorporation of dopants, which allows the material to be customized to meet the requirements of

different climate zones.[26–30] Next, the transition occurs on ultra-fast timescales rendering a homogeneous appearance for optical films[31] and mitigating the inhomogeneities often observed for liquid crystalline or electrochromic devices. Fourth, optical films incorporating VO_2 can be passively switched in response to the external ambient without requiring active electronic control, thereby mitigating the substantial investments oftentimes required by electrochromic units. Finally, vanadium is substantially cheaper than precious metals often used in reflective thin films.

Despite the numerous advantages of VO_2 enumerated above, there exist several impediments to its utilization that have thus far precluded commercial viability. A major impediment to the application of VO_2 in systems that require thermal cycling is the strain that accompanies the structural phase transition. Inhomogeneous lattice strain, which can be as much as 4%, can bring about mechanical degradation or delamination of thin films. Scaling to nanometer-sized dimensions allows for better accommodation of strain, makes these materials resilient to the strain associated with prolonged thermal cycling, and furthermore avoids crack formation and delamination that plague larger crystallites and thin films of VO_2.[19,32] Thermal stability issues represent a further challenge; VO_2 is readily oxidized to V_2O_5 under ambient conditions, especially upon exposure to moisture. The deposition of amorphous SiO_2 shells has been shown to enhance the thermal and chemical stability of VO_2 nanomaterials.[33]

In order to obtain high-quality optical films that demonstrate a large modulation of NIR transmission with retention of good visible light transmittance, optical simulations suggest that it is imperative to prevent Mie scattering, which gives rise to a mostly temperature invariant signature and haze.[34] Mitigating the appearance of a scattering background requires the use of nanocrystals that are of the optimal particulate dimensions (but that are of good crystal quality

and still retain a large magnitude of the phase transition) and further requires the individual dispersion of the particles within low dielectric constant media. Agglomerates present a scattering background very similar to larger particles and thus obtaining a good dispersion of the particles is imperative for functional films. As an additional imperative, the nanocomposites have to be chemically and mechanically resilient, which necessitates a robust interface between the nanocrystals and host matrix. Furthermore, for the viable casting of large-area films, the use of aqueous processes is desirable given increasing concerns regarding the toxicity of organic solvents and curing agents.[35–37] However, this in itself brings a fresh set of challenges since the low viscosity of water makes it difficult to cast films using conventional liquid-phase coating processes. As a direct attempt to address several of these challenges, we demonstrate an entirely aqueous processing approach for obtaining VO_2 nanocomposite thin films showing a high degree of NIR suppression and visible light transmittance. The mitigation of scattering allows for a low onset wavelength of NIR suppression. Surface functionalization with perfluorinated silanes followed by dispersion within methacrylate matrices allows for homogeneous films exhibiting pronounced NIR suppression to be cast from aqueous solutions.

III.2 Experimental

An Aqueous-phase Synthetic Route to VO_2 Nanocrystals. A two-step proceedure was developed to prepare phase-pure VO_2 nanocrystals based on modification of a previously reported method.[38,39] The first step involves the precipitation of $VO(OH)_2$ from a reaction between ammonium metavanadate (NH_4VO_3) and hydrazine (H_2NNH_2) in deionized water (ρ=18.2MΩ/cm, Barnstead Water Purification System) at 80°C (Fig. 1). The second step was the hydrothermal annealing of the $VO(OH)_2$ precipitate within a hydrothermal vessel at 210°C for

24—72 h. The product was recovered by centrifugation at 8500 rpm and the aqueous supernatant was decanted. The solid was then dispersed in acetone *via* ultrasonication, centrifuged at 8500 rpm, followed by the decanting of the acetone supernatant. This acetone washing process was carried out a total of three times.

For comparison, two sets of VO_2 nanowires were also used; nanowires prepared by 2-propanol reduction of V_2O_5 had widths of 210 ± 70 nm and lengths of 4.0 ± 3.0 μm; whereas nanowires prepared by acetone reduction of V_2O_5 had widths of 180 ± 70 nm and lengths of 1.6 ± 0.9 μm as described in our previous work.[19,40]

Deposition of a SiO_2 Shell onto the VO_2 Nanocrystals. Amorphous silica shells were constituted using a modified Stöber method, as reported in previous work.[33] Briefly, 24—48 mg of VO_2 nanocrysals were ultrasonicated in an 4:1 (*v*/*v*) ethanol:water solution to obtain a homogeneous dispersion. 400 μL of ammonium hydroxide (NH_4OH) (0.25M final solution) was used as the catalyst with 24 mg of VO_2 nanocrystals. The catalyst was added to the VO_2 dispersion in 8 mL nanopure water and 32 mL ethanol under vigorous ultrasonication over a period of 10 min. Subsequently, 200 μL tetraethylorthosilicate (TEOS) was added to this dispersion (yielding a 0.02M concentration of TEOS). After reaction for 25 min at room temperature, the VO_2@SiO_2 core—shell nanocrystals were collected by centrifugation. The solid was purified by redispersing in ethanol and collection by centrifugation over three cycles.

Surface Functionalization with Fluorinated Silanes. Hydrothermally grown VO_2 nanocrystals have a high density of surface hydroxyl groups, which can be reacted with silanols to create V—O—Si linkages.[33] Such condensation reactions allow for installation of molecular monolayers on VO_2 surfaces when appropriately functionalized silanes are used. A perfluorinated silane has been grafted directly onto the VO_2 surfaces or onto the surfaces of

VO_2@SiO_2 core—shell nanocrystals. In both cases, a 0.02M solution of (heptadecafluoro-1,1,2,2-tetrahydrodecyl)trimethoxysilane in tetradecafluorohexane (>96% purity) was prepared and stored within polypropylene receptacles. In a typical reaction, 24 mg of VO_2 (or VO_2@SiO_2) nanocrystals was added to the 0.02M perfluorinated silane solution in tetradecafluorohexane, ultrasonicated for roughly 5 min, and allowed to stir overnight to graft the fluorinated siloxane layer onto the nanocrystal surfaces. No water was added during the reaction but the hydrothermally prepared VO_2 nanocrystals contain surface adsorbed water that facilitates hydrolysis of the silane. After reaction, the solid was purified by redispersing in tetradecafluorohexane and collection *via* centrifugation for a total of three cycles to remove adsorbed silanes. After surface functionalization, the nanocrystals can no longer be dispersed in water but are readily dispersible in tetradecafluorohexane, which provides a rapid means of evaluating the success of the grafting step. As-prepared VO_2 nanocrystals functionalized with the perfluorinated silane are denoted as VO_2@-F. Core—shell VO_2@SiO_2 nanocrystals were also functionalized with the perfluorinated silane and are designated as VO_2@SiO_2-F.

Aqueous Dispersions of Functionalized VO_2 Nanocrystals using a Perfluorinated Surfactant. Potassium perfluorooctanesulfonate (PFOS) was used to disperse the functionalized VO_2@-F and VO_2@SiO_2-F in water. Briefly, a given amount of the VO_2@-F and VO_2@SiO_2-F solid was dispersed in 10 mL of water at a pH of ca. 11.5 along with 1 mg of PFOS and the mixture was ultrasonicated for ca. 20 min. Subsequently, additional amounts of solid PFOS were added in increments of 1—2 mg until the solids were homogeneously dispersed in the alkaline deionized water solution. Care must be taken to ensure that a minimal amount of surfactant is utilized in order to avoid surfactant agglomeration and micelle formation that can degrade the optical quality of thin films. The proportions of PFOS to the functionalized VO_2@-F and

VO_2@SiO_2-F solids used to obtain homogeneous 10 mL dispersions were as follows: 2 mg fluorinated solid to ca. 1.1 mg PFOS, 4 mg fluorinated solid to ca. 1.5 mg PFOS, 6 mg fluorinated solid to ca. 1.7 mg PFOS, 8 mg fluorinated solid to ca. 1.6 mg PFOS, 10 mg fluorinated solid to ca. 3.0 mg PFOS, 12 mg fluorinated solid to ca. 3.2 mg PFOS, and 16 mg fluorinated solid to ca. 3.0 mg PFOS.

Polymer Nanocomposites. In order to prepare nanocomposites, VO_2 nanocrystals were homogenously dispersed within a methacrylic acid/ethyl acrylate copolymer (Acrysol ASE-60™, a commercially available high-shear viscosity thickener obtained from Dow Chemical).[41,42] Dispersions of VO_2, VO_2@SiO_2, VO_2@-F, and VO_2@SiO_2-F nanocrystals were prepared in the following manner. Briefly, ca. 3 mg of nanocrystals were dispersed by ultrasonication for 5 min in 9.67 mL of deionized water with pH adjusted to ca. 11.5 by the addition of a solution of 2-amino-2-methyl-1-propanol containing 5% added water (Amresco). As-prepared VO_2 and VO_2@SiO_2 were dispersed in water after synthesis without further processing, whereas VO_2@-F, and VO_2@SiO_2-F nanocrystals were dispersed in water with the help of PFOS as outlined above. Next, the colloidal aqueous dispersion was stirred using a magnetic stir plate and 0.33 mL of the methacrylic acid/ethyl acrylate copolymer solution in water was introduced to obtain a 1 wt.% final concentration of the polymer (the solid content was ca. 28%). Care was taken to avoid foaming and vortex formation in the vial. The alkaline pH induced thickening of the solution; the stirring speed was successively increased to ensure homogeneous dispersion of the nanocrystals. The dispersion was stirred was for at least 20 min after it turned clear (from the initial milky white appearance).

In addition to methacrylic acid/ethyl acrylate copolymer, polyacrylate and hydroxyethylcellulose (Rheolate-1™ obtained from Elementis Specialties and Natrosol B™

obtained from Ashland Chemicals, respectively) matrices were also attempted. However, the polyacrylate dispersions had a low viscosity and did not yield high-quality optical thin films; hydroxyethylcellulose dispersions could be cast into high-quality homogeneous thin films; however, the optical transmittance of the cellulosic matrix was substantially lower than methacrylic acid/ethyl acrylate copolymer and thus only the latter is discussed in subsequent sections. Several phosphate ester surfactants (Dextrol^{TM} and Strodex^{TM} from Ashland Chemicals) were further examined for their ability to facilitate dispersion of the nanocrystals in the methacrylic acid/ethyl acrylate copolymer aqueous dispersion but yielded only marginal improvements in the stability of the dispersions and did not substantially enhance the optical performance of the obtained thin films. Subsequent sections thus focus on studies of VO_2 or VO_2@SiO_2 nanocrystals dispersed within the methacrylic acid/ethyl acrylate copolymer matrix without the use of any additional surfactants and VO_2@-F and VO_2@SiO_2-F nanocrystals dispersed with the help of PFOS.

Film Preparation. Films were cast on 2.5 x 7.5 cm borosilicate glass microscope slides that were cleaned with ethanol and low-lint wipes prior to casting. Films contained a range of VO_2, VO_2@SiO_2, VO_2@-F, and VO_2@SiO_2-F nanocrystal loadings (for 2—16 mg of VO_2 nanocrystals in 10 mL of the methacrylic acid/ethyl acrylate copolymer aqueous dispersion). Films were cast onto glass substrates by drawing out ca. 2.0 mL of the dispersion into a syringe. The previously described borosilicate glass substrate was then placed on an even surface. The dispersion was then placed along a straight line down the center of the borosilicate glass substrate. A casting knife from BYK Wesel, Germany set at a wet thickness of 1 mm was drawn across the substrate. The film was then allowed to cure overnight at room temperature under ambient conditions. After curing, the average dry film thickness was ca. 1—2 μm.

Characterization. Transmission electron microscopy (TEM) images were recorded on a JEOL JEM-2010 instrument operated at an acceleration voltage of 200 kV. Energy dispersive X-ray (EDX) maps were obtained using a JEOL JSM-7500F scanning electron microscope operated at an acceleration voltage of 15 kV with an emission current of 10 μA and a probe current of 12 μA. Powder X-ray diffraction (XRD) data was obtained using a Bruker D8-Focus Bragg-Brentano diffractometer equipped with a Lynxeye detector. Differential scanning calorimetry (DSC) traces were recorded on a Q2000 TA Instrument calorimeter using Al pans and lids. A scanning rate of 15°C per minute under argon was used for the DSC measurements. FTIR data were acquired on a Bruker Vertex-70 FTIR instrument equipped with a Pike MIRacle™ single reflection horizontal ATR accessory. Evaluation of film thicknesses was carried out with a Bruker Dimension Icon atomic force microscope operating in tapping mode. Adjustments to solution pH were monitored with a HACH HQ411d benchtop pH/mV meter utilizing an IntelliCal™ PHC201 standard gel-filled pH electrode. Microindentation for characterization of mechanical properties was accomplished using a Hysitron TI Triboindenter equipped with a Berkovich tip utilizing an applied force of ca. 70 μN. Adhesion testing was performed in accordance with the American Society for Testing Materials (ASTM) guidelines for each test employed. These tests were carried out with a BYK Cross-Cut-Tester for evaluating adhesion by tape test (according to ASTM D3359) and a BYK Balanced Beam Scrape Adhesion and Mar Tester for assessing adhesion of organic coatings by scrape adhesion (according to ASTM D2197).[43,44] Optical characterization of the thin films was performed using a multi-wavelength Bruker Vertex-70 FTIR spectrometer equipped with a Pike Technologies temperature stage in the spectral range between 400 and 2500 nm. The samples were allowed to equilibrate for 10 min at each temperature prior to recording a spectrum. A change in beam splitter distorts the spectra between 1180 and 1250 nm and this region is thus omitted

from the spectral profiles. In order to determine the optical properties attributed to VO_2 nanocrystals alone, a spectrum of a borosilicate glass slide coated with unmodified methacrylic acid/ethyl acrylate copolymer was recorded and the percent transmission reduction across the spectra attributed to the copolymer and glass was added back into the nanocomposite spectra in each instance. This allows each spectra to represent only visible light transmission and NIR suppression contributions from the VO_2 component of the nanocomposite films by removing any contribution from the glass and copolymer.

III.3 Results and Discussion

A primary challenge with the preparation of hybrid nanocomposites is to ensure adequate dispersion of the inorganic filler within the polymeric host matrix in order to realize properties such as mechanical reinforcement, electrical percolation, or matching of dielectric constants for specific optical applications.[37,45–48] For applications of VO_2 nanocomposite thin films as thermochromic elements, particle sizes <100 nm are predicted to be imperative to prevent a large Mie scattering background and furthermore the high-dielectric-constant particles (n = 2.7, k = 0.65) have to be refractive index matched and embedded within a low-dielectric-constant medium without agglomeration.[34] For many semiconductor and oxide materials, solution-phase synthetic methods yield nanocrystals capped with surface passivating ligands that can be readily dispersed within polymeric host matrices.[49–51] However, the metal—insulator transition as well as the preferred phase of VO_2 are both extremely sensitive to the oxygen stoichiometry and crystallinity; consequently, high-quality VO_2 nanomaterials exhibiting pronounced electronic phase transitions have not thus far been accessible from such hot colloidal decomposition routes. High-pressure hydrothermal methods have emerged as an attractive alternative and yield

materials with precise control of dimensions and oxygen stoichiometry.[16,30,52–55] In recent work, we have demonstrated that the stepwise hydrothermal reduction of V_2O_5 with aliphatic alcohols yields VO_2 nanocrystals exhibiting an abrupt (<1° sharpness), almost five orders of magnitude, change in electronic resistance upon the phase transition in single-nanowire electrical measurements and an electrical bandgap of 0.6 eV in the insulating phase, consistent with the optical bandgap.[19] While hydrothermal methods yield high-crystalline-quality faceted nanocrystals, the absence of surface passivating ligands results in considerable agglomeration of the obtained materials and renders them difficult to disperse in solvents or polymeric matrices. In this work, we have explored the dispersion of VO_2 nanocrystals within aqueous polymeric media and homogeneous thin films facilitated by surface functionalization of hydroxyl moieties on VO_2 surfaces with silanes. We have further correlated such dispersion to thermochromic characteristics and devised constructs that substantially mitigate light scattering based on encapsulation of dispersed VO_2 nanocrystals within low-dielectric-constant shells. Two distinct approaches are explored: (1) The grafting of perfluorinated silanes to allow for individual dispersion of VO_2 nanocrystals and (2) the creation of SiO_2 shells around the VO_2 nanocrysyals by continued condensation and siloxane bond formation upon reaction with tetraethylorthosilicate (TEOS). Finally, both approaches have been combined by grafting perfluorinated silanes to VO_2@SiO_2 core—shell nanocrystals. The nanocrystals are dispersed within a methacrylic acid/ethyl acrylate copolymer, which is used as an optically transparent low-refractive-index medium.

VO_2 nanocrystals have been obtained by reacting NH_4VO_3 and H_2NNH_2 to obtain amorphous $VO(OH)_2$, which is subsequently hydrothermally recrystallized.[38,39] **Figure III. 1** depicts the reaction yielding VO_2 nanocrystals and further illustrates the surface

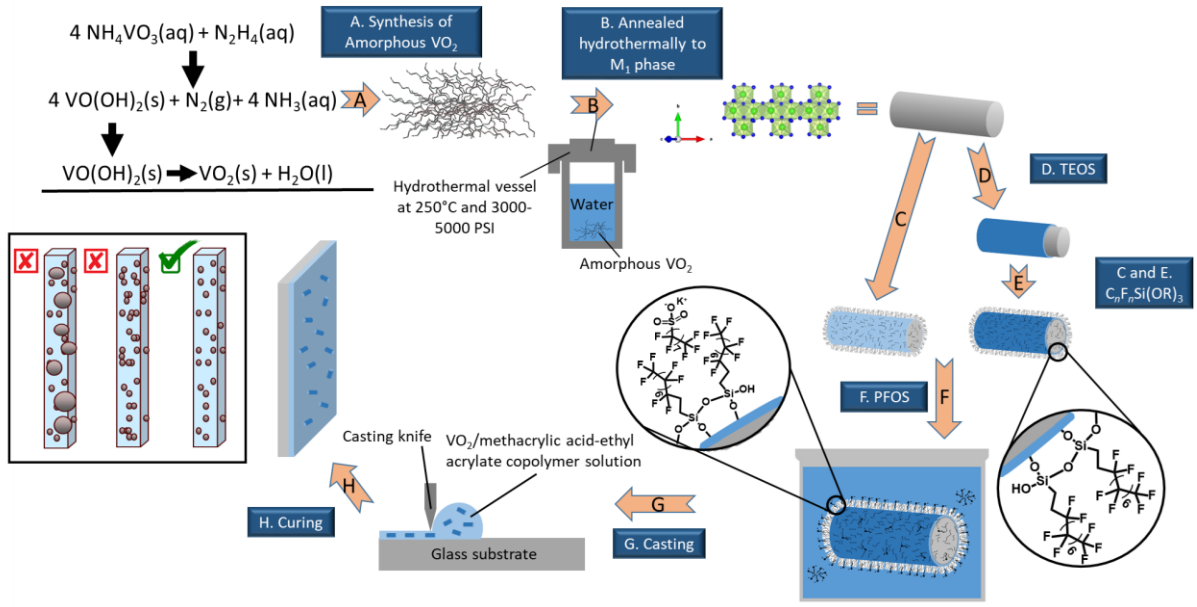

Figure III. 1 Schematic depiction of the overall process for preparation of thermochromic fenestration elements. A) Reaction leading to the synthesis of amorphous VO_2. B) Crystallization of amorphous precursors to obtain VO_2 nanocrystals stabilized in the M1 phase. C) Grafting of trimethoxy(1H,1H,2H,2H-perfluorooctyl)silane to the surface of bare VO_2 nanowires, or D) application of an amorphous SiO_2 shell by reaction with TEOS as per the modified Stöber method. E) Grafting of trimethoxy(1H,1H,2H,2H-perfluorooctyl)silane to the silica-coated surface. F) Dispersion of VO_2 and VO_2@SiO_2 nanocrystals bearing pendant fluorinated moieties in water using PFOS followed by addition of the methacrylic acid/ethyl acrylate polymeric matrix. G) Application of dispersion to cleaned borosilicate glass and the preparation of uniform thin films using a casting knife. H) Curing for 12 h in order to obtain the final thermochromic films. The inset on the left schematically illustrates the desired ideal of small particles homogeneously dispersed within a polymeric matrix and depicts from left to right the following scenarious: large particles that scatter light, agglomerations of small particles that have a similar effect, and, the ideal case, small, individually dispersed particles.

functionalization and dispersion strategy used to obtain homogeneous thermochromic films. As noted above, the design of optical nanocomposites necessitates control of both particle size and dispersion since large particles as well as agglomerations of small particles will yield temperature invariant scattering backgrounds, diminishing the pronounced NIR modulation

desired for thermochromic applications.[34] The inset to Figure III. 1 schematically contrasts the desired ideal of individually dispersed particles with undesirable scenarios of large or agglomerated optically active particles embedded within the polymeric matrix. We contrast three distinct size regimes of particles to arrive upon the optimal particulate dimensions and then subsequently evaluate the influence of different dispersion methods.

Figure III. 2A depicts transmission electron microscopy images of the as-prepared VO_2 nanocrystals. Based on statistical analysis of 350 particles, an average crystallite size of 44 ± 30 nm has been deduced. The crystallites are clearly clustered within larger agglomerates. Figure

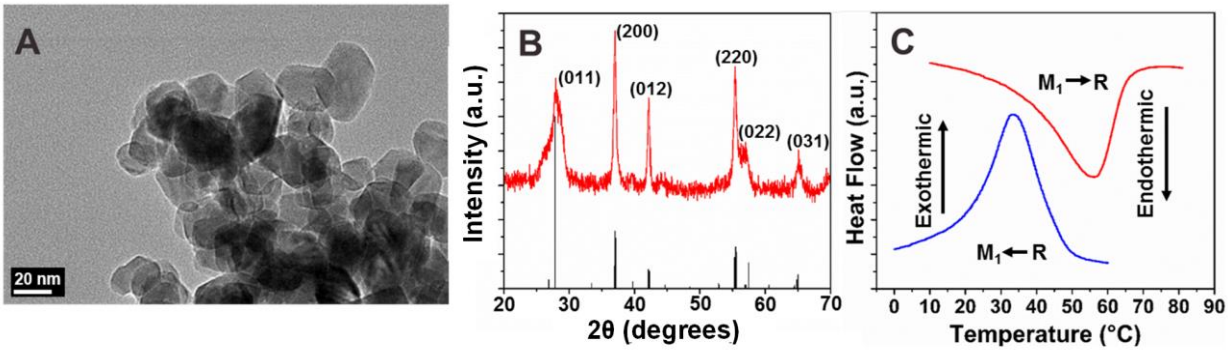

Figure III. 2 A) TEM image of as-prepared VO_2 nanocrystals. B) Powder XRD pattern acquired for VO_2 nanocrystals. The Scherrer broadening of the reflections attests to the small crystallite dimensions of the obtained materials. C) DSC plots acquired for as-prepared VO_2 nanocrystals indicating an endothermic transition upon heating in red and an exothermic transition upon cooling in blue.

III. 2B shows a powder XRD pattern acquired for the as-prepared nanocrystals, which can be indexed to the monoclinic M1 phase of VO_2 (Joint Committee on Powder Diffraction Standards (JCPDS) 43-1051). The Scherrer broadening of the reflections further corroborates their nanometer-sized dimensions. Figure III. 2C plots differential scanning calorimetry traces acquired for these samples, which exhibit pronounced features corresponding to the endothermic

transition of M1 to rutile VO_2 (insulator to metal) and the exothermic transition of rutile to M1 phase VO_2 (metal to insulator). The measured heat flow corresponds to a discontinuous change of lattice enthalpy originating from the structural phase transition as well as pronounced step-change of the conduction entropy of electrons upon metallization.[56,57] The observed hysteresis between heating and cooling cycles is characteristic of first-order transitions.

In order to disperse the nanocrystals, protect them from oxidation, and to facilitate further processing, two approaches have been developed based on grafting of silanes to the surface hydroxyl groups of the hydrothermally prepared VO_2 nanocrystals (Fig. 1). Reaction with TEOS as per the modified Stober method yields core—shell VO_2@SiO_2 nanocrystals as depicted in **Figure III. 3**. In the TEM image shown in Figure III. 3A, the high-electron density crystalline

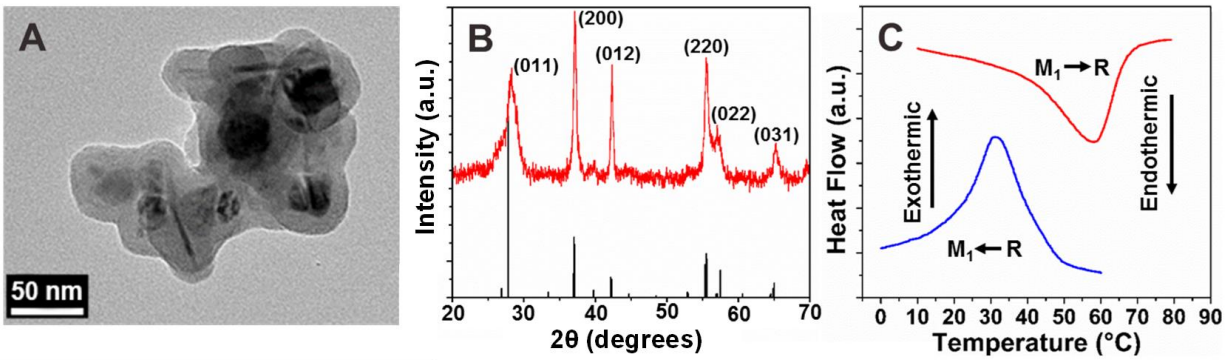

Figure III. 3 A) TEM image of core—shell VO_2@SiO_2 nanocrystals. B) Powder XRD patterns acquired for core—shell nanocrystals indexed to the M1 phase of VO_2. No pronounced changes are discernible upon deposition of SiO_2. C) DSC traces of ultrasmall VO_2@SiO_2 showing an endothermic transition at 58°C upon heating and an exothermic transition at 31°C upon cooling.

VO_2 cores can be readily resolved from the amorphous SiO_2 shells. The SiO_2 shells engender a reduced degree of agglomeration and form a matrix encapsulating the VO_2 nanocrystals. The hydrophilic SiO_2 shells facilitate facile dispersion of the particles in water as schematically depicted in Figure III. 1 and discussed below. Figure III. 3B illustrates that no new reflections

are observed in the XRD pattern upon deposition of SiO_2 attesting to the amorphous nature of the shell.[33] The DSC data in Figure III. 3C further indicates that SiO_2 deposition does not alter the temperature or magnitude of the phase transition.

In an alternative approach, as also schematically illustrated in Figure 1, the as-prepared core—shell VO_2@SiO_2 nanowires are reacted with (heptadecafluoro-1,1,2,2-tetrahydrodecyl)trimethoxysilane in tetradecafluorohexane solution. Reaction with the perfluorinated silane installs perfluorinated groups on the nanocrystal surface. The VO_2@SiO_2@-F nanocrystals are rendered completely hydrophobic as indicated by **Figure III. 4A**, but can be readily dispersed in tetradecafluorohexane (Fig. III. 4B). In contrast, as-prepared VO_2 nanocrystals can be somewhat dispersed in water and are not wetted at all by tetradecafluorohexane. **Figure III. 4C** depicts an EDX spectrum acquired after functionalization indicating the presence of Si and F on the nanocrystal surfaces.

Figure III. 4D depicts a FTIR spectrum acquired after functionalization. The spectra have been acquired in attenuated total reflectance mode. The FTIR spectra is characterized by features at 2924 and 2853 cm^{-1}, which are ascribed to methylene H—C—H asymmetric and symmetric stretching modes, respectively.[58] The values indicate a high degree of ordering of the CH_2 domains of the fluorinated monolayer and infers that the siloxanes are bonded in close proximity to one another on the VO_2 nanocrystal surfaces.[59,60] Dangling Si—OH bonds are also discernible at 1013 cm^{-1}.[58,61] Further evidence for the presence of the fluorinated self-assembled monolayer on the nanocrystals is derived from the peak at 1263 cm^{-1}, which is characteristic of Si—CH_2 stretching arising from the methylene segment of the monolayer.[58,62] A feature observed at 1113 cm^{-1} can be attributed to Si—O—Si stretching from cross-linked siloxanes formed at the nanocrystal surface.[58] A large number of features are present in the region between

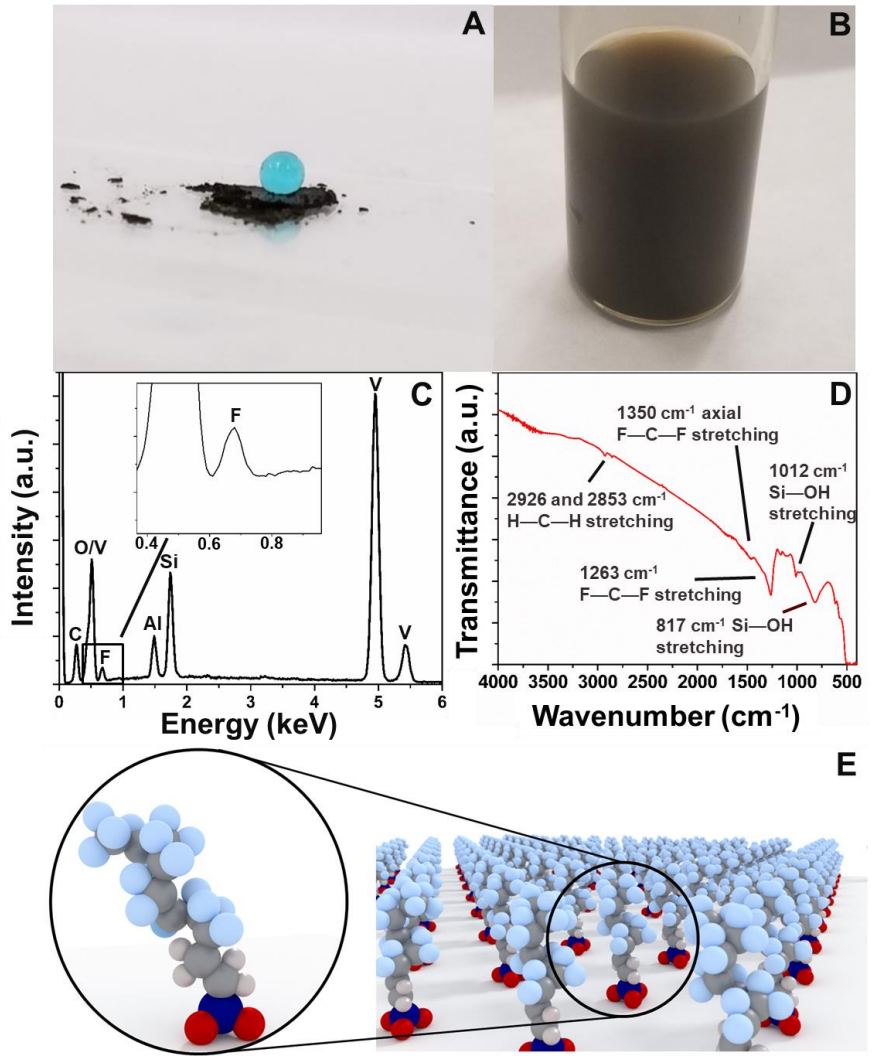

Figure III. 4 A) Digital photograph showing the interaction of a water droplet with VO_2@SiO_2-F nanocrystals; functionalization with a perfluorinated silane renders the surface superhydrophobic. B) VO_2@SiO_2-F nanocrystals are readily dispersible in a perfluorinated solvent. C) EDX spectrum of VO_2@SiO_2-F nanocrystals. D) FTIR ATR spectrum of VO_2 nanowires functionalized with trimethoxy(1H,1H,2H,2H-perfluorooctyl)silane showing characteristic modes of the perfluorinated moieties. E) Graphical representation if the helical-tilt configuration of (heptadecafluoro-1,1,2,2-tetrahydrodecyl)trimethoxysilane SAMs. Spheres represent the following: **light blue = F**; **dark blue = Si**; **red = O**; **white = H**; and **gray = C**.

1400 and 1100 cm^{-1}, especially a strong peak at 1263 cm^{-1}; these features are attributed to F—C—F stretches.[58,62] The poor resolution of individual peaks in this region is attributed to the

presence of multiple rotational isomers of fluoroalkyl chains; however, a peak at 1350 cm^{-1} is fairly well resolved and is specifically attributed to axial CF_2 stretching.[59] The distinctive feature observed for this vibrational mode is characteristic of fluoroalkyl chains configured into a helical-tilt orientation as observed previously for fluoroalkyl self-assembled monolayers albeit such ordering has not thus far been observed on highly curved surfaces such as presented by the nanocrystals here.[59,63,64] Parallel C—F stretching relative to the helical axis results in the change of dipole necessary for observation of this peak.[59,64,65] Furthermore, peaks at 1088 and 1200 cm^{-1} that represent Si—O—CH_3 stretching in the silane precursor are no longer observed for the functionalized product corroborating the hydrolysis of the methoxysilane groups (**Fig. A 5**, Appendix A).[58] The FTIR data thus suggest that the silanes form close-pack ordered arrays on the surfaces of the VO_2 nanocrystals. These arrays can substantially mitigate agglomeration of the nanocrystals and allow for casting of homogeneous optically transparent thin films. **Figure III. 4E** depicts a graphical representation of the helical-tilt arrangement exhibited by (heptadecafluoro-1,1,2,2-tetrahydrodecyl)trimethoxysilane and other fluoroalkyl silane SAMs.[51,61,62] **Figure A 6** (Appendix A) indicates analogous characterization data for VO_2 nanocrystals functionalized with (heptadecafluoro-1,1,2,2-tetrahydrodecyl)trimethoxysilane (without initial deposition of a SiO_2 shell). Again, surface functionalization renders the nanocrystals hydrophobic and facilitates dispersion in a perfluorinated solvent. Functionalization with the fluorinated silane is furthermore critical from a practical materials stability perspective. As-prepared VO_2 is partially oxidized to V_6O_{13} within less than 7 days upon dispersion in water (at neutral pH) with characteristic green coloration of the latter phase visible to the naked eye. In contrast, VO_2@SiO_2 dispersions show no degradation even after 6 weeks. The VO_2@-F and VO_2@SiO_2-F nanocrystals are rendered completely hydrophobic (Fig. III. 4A and Fig. A 6A,

respectively) and maintain their integrity for >12 weeks upon exposure to aqueous media, which is further attributed to the precise ordering of the pendant perfluorinated monolayers that form a helical close-packed array on the nanocrystal surfaces. The ability to prevent degradation of VO_2 is of course critical to the preparation and storage of formulations for casting thermochromic thin films but perhaps more importantly suggests that the thermochromic elements will be far more resilient upon exposure to high humidity conditions as a result of silane functionalization.

In order to facilitate dispersion of the fluorinated nanocrystals in aqueous media, a fluorosurfactant PFOS has been titrated as described in the experimental section. The perfluorinated pendant chain of PFOS is able to interact with the perfluorinated pendant chains of the functionalized VO_2@-F (and VO_2@SiO_2-F) nanocrystals, whereas its sulfonate terminal group facilitates aqueous dispersibility. **Figure A 7** (Appendix A) indicates digital photographs of VO_2@-F in water before and after the addition of PFOS. The addition of PFOS clearly results in stabilization of a homogeneous colloidal dispersion. A methacrylic acid/ethyl acrylate copolymer matrix has been selected as the host. It has a high degree of optical transparency in the visible region of the electromagnetic spectrum and exhibits a pH tunable viscosity that allows for casting of uniform thin films from aqueous solution. The polymer is added to the VO_2@SiO_2, VO_2@-F/PFOS, or VO_2@SiO_2-F colloidal dispersions at acidic pH. Subsequently, the pH is increased by addition of 2-amino-2-methyl-1-propanol containing 5% added water causing deprotonation of methacrylic acid groups that take on an anionic charge.[41,42,66,67] Charge repulsion between anionic groups induces swelling of the copolymer and disperses particles based on volume exclusion.[41,67] The swelling is clearly discernible by the transition of milky white color of the polymer to a highly transparent appearance and by a pronounced increase in the viscosity of the solution, which results from expansion of the polymer. This matrix allows for

homogeneous dispersion of 1—16 mg/mL of functionalized VO_2@SiO_2 nanocrystals. **Figure A 8** (Appendix A) shows digital images of transparent thin films embedded with VO_2 nanocrystals prepared by this method.

In order to maximize energy efficiency of fenestration elements, a comparison of several different metrics is imperative, (a) the visible light transmittance (a fenestration element that is overly dark will be of limited utility); (b) the extent of NIR suppression, which reflects the efficacy of the element in modulating solar heat gain without impacting visible transparency; and (c) the onset of NIR suppression. The last mentioned parameter is of critical relevance for energy efficiency. An early onset of NIR suppression in the 770—800 nm regime allows for the considerable solar flux in the low-wavelength NIR to be reflected at high temperatures. However, this part of the spectrum is also characterized by a scattering background, which can diminish the NIR suppression. Scattering thus induces a red-shift of the NIR suppression to higher wavelengths, where there is less solar flux.

Given the need to simultaneously control both particle size and dispersion as depicted in Fig. 1, three different size regimes of particles have been evaluated; the 44 ± 30 nm nanoparticles noted above have been contrasted to nanowires with lateral dimensions of 210 ± 70 nm and lengths of 4.0 ± 3.0 μm and nanowires with lateral dimensions of 180 ± 70 nm and lengths of 1.6 ± 0.9 μm nanowires prepared as reported in our previous work.[19,40] **Figure III. 5** and **Table III. 1** depict optical spectroscopy data acquired for the three different dimensions of embedded particles dispersed by encapsulated within a SiO_2 shell, functionalization with a perfluorinated silane, and titration with a surfactant (VO_2@SiO_2-F). It is clear that for comparable particle loading, the smallest particle size does considerably better both in terms of the onset of NIR suppression and the magnitude of the NIR modulation. Similar size-dependent results are

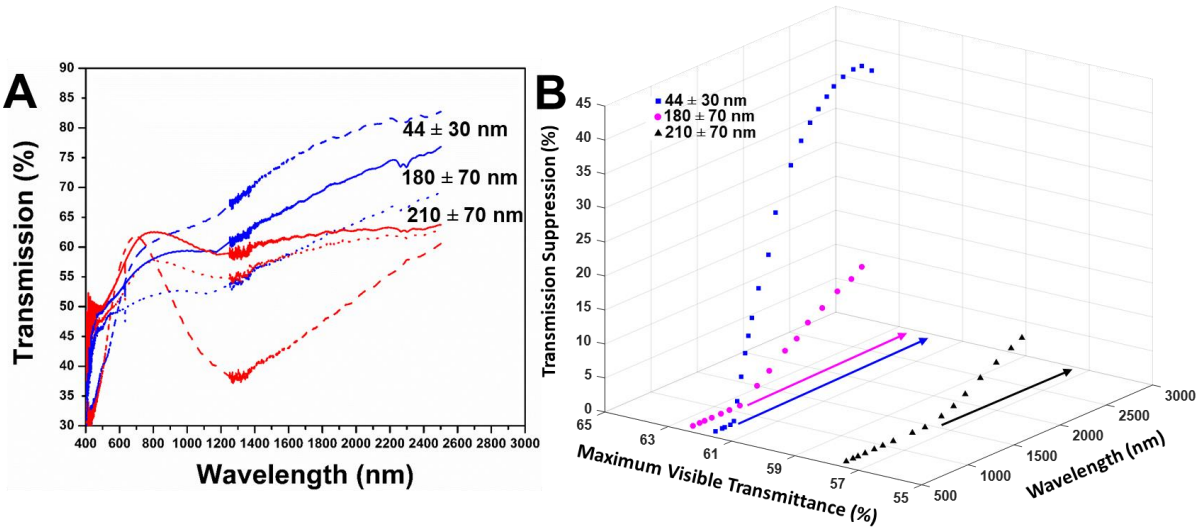

Figure III. 5 A) Absorption spectra acquired for three different sizes of VO_2@SiO_2-F nanocrystals. The plots correspond to 44 ± 30 nm nanocrystals (dashed lines); nanowires with lateral dimensions of 210 ± 70 nm and lengths of 4.0 ± 3.0 μm (dotted lines); and nanowires with lateral dimensions of 180 ± 70 nm and lengths of 1.6 ± 0.9 μm nanowires (solid lines). In each case, 4 mg of the nanowires is dispersed in 10 mL of an aqueous dispersion of 1 wt.% (relative to 10 mL volume of water) methacrylic acid/ethyl acrylate copolymer and cast onto borosilicate glass substrates. Spectra obtained at 30°C are displayed in blue, whereas spectra obtained at 85°C after equilibration for 10 min are shown in red. B) 3D representation of VO_2@SiO_2-F optical data plots showing three nanocrystal size distributions: 44 ± 30 nm nanocrystals (blue squares); nanowires with lateral dimensions of 210 ± 70 nm and lengths of 4.0 ± 3.0 μm (black triangles); and nanowires with lateral dimensions of 180 ± 70 nm and lengths of 1.6 ± 0.9 μm nanowires (purple circles). Maximum visible transmission is the maxima in the visible region from each 85°C plot in (A) and is constant for each plot (represented by an arrow across the maximum visible transmittance/wavelength plane).

obtained when the particles are encapsulated with SiO_2 (VO_2@SiO_2) or simply functionalized with the perfluorinated silane (VO_2@-F). Given these results, the 44 ± 30 nm nanocrystals are selected to further evaluate the different dispersion modes. **Figure III. 6** depicts the temperature-dependent UV- visible-NIR absorption spectrum acquired for as-prepared VO_2 nanocrystals dispersed in the methacrylic acid/ethyl acrylate copolymer matrix at different VO_2 loadings and cast onto borosilicate glass. With increasing temperature, the insulator—metal transition induces a pronounced change of optical transmittance.[68–70] Metallization strongly decreases the

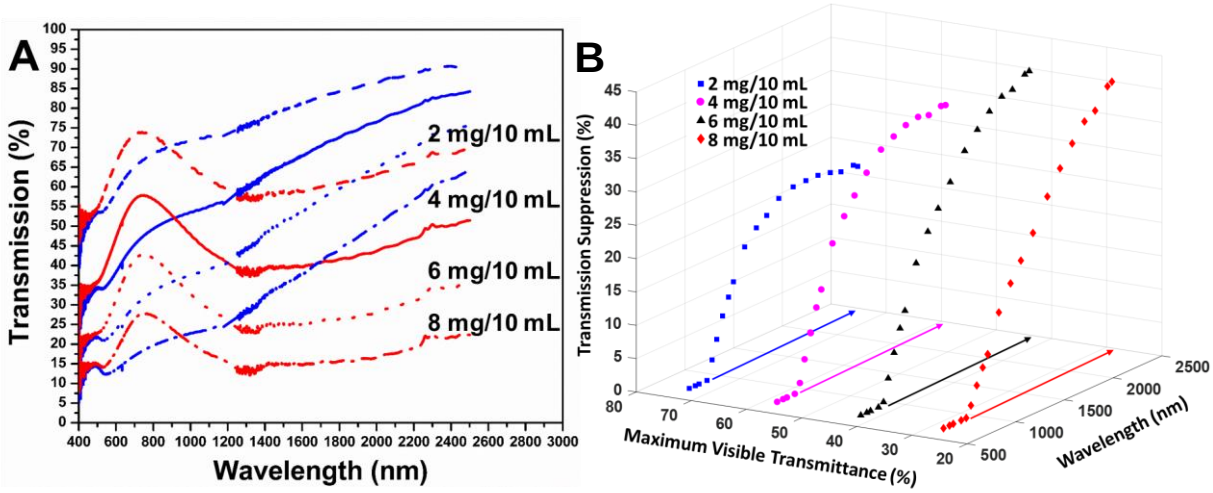

Figure III. 6 A) Absorption spectra acquired for four different loadings of VO_2 nanocrystals. The plots correspond to 2 mg (dashed lines), 4 mg (solid lines), 6 mg (dotted lines), and 8 mg (alternating dash-dot lines) dispersed in 10 mL of an aqueous dispersion of 1 wt.% (relative to 10 mL volume of water) methacrylic acid/ethyl acrylate copolymer cast onto borosilicate glass substrates. Spectra obtained at 30°C are displayed in blue, whereas spectra obtained at 85°C after equilibration for 10 min are shown in red. B) 3D representation of VO_2 optical data plots showing four nanocrystal loadings: 2 mg (blue squares), 4 mg (purple circles), 6 mg (black triangles), 8 mg (red diamonds). Maximum visible transmission is the maxima in the visible region from each 85°C plot in (A) and is constant for each plot (represented by an arrow across the maximum visible transmittance/wavelength plane).

Table III. 1 Summary of maximum NIR modulation, transmission in the visible region, and onset of NIR suppression for varying size distributions of VO_2@SiO_2-F nanocrystals. The particle loading is 4 mg/10 mL in each case.

Nanocrystal size distribution (widths)	Maximum NIR Suppression (%)	Maximum Transmittance in the Visible Spectrum (%)	Onset of NIR Suppression (nm)
44 ± 30 nm	30.2	61.8	758
180 ± 70 nm	13.1	62.5	1120
210 ± 70 nm	6.36	57.7	1580

transmittance as a result of the increased reflectivity of the metallic VO_2 nanocrystals. The pronounced suppression of NIR transmittance as a function of the ambient temperature observed

here is what makes this material attractive as a fenestration element. Figure III. 6B indicates that for the 2 mg/mL dispersion, NIR suppression of 24% is obtained at a visible light transmittance of ca. 74% and the onset of NIR suppression occurs at 883 nm. A pronounced divergence of the

Table III. 2 Summary of maximum NIR modulation, transmission in the visible region, and onset of NIR modulation for bare VO_2, VO_2@SiO_2, VO_2@-F, and VO_2@SiO_2-F nanocrystals dispersed at various loadings in a methacrylic acid/ethyl acrylate matrix. Data for higher loadings of VO_2 nanocrystals are listed in **Tables A 1—A 4**.

Sample and Nanocrystal Loading within Composite	Maximum NIR Suppression (%)	Maximum Transmittance in the Visible Spectrum (%)	Onset of NIR Suppression (nm)
VO_2			
2 mg	23.8	73.9	883
4 mg	33.7	57.9	914
6 mg	40.4	42.8	926
8 mg	41.9	27.8	926
VO_2@-F			
2 mg	23.3	78.9	780
4 mg	38.2	52.4	775
6 mg	41.0	40.4	789
8 mg	40.1	33.3	789
VO_2@SiO_2			
2 mg	24.4	77.6	812
4 mg	39.9	54.0	810
6 mg	47.2	38.4	788
8 mg	46.4	29.7	804
VO_2@SiO_2-F			
2 mg	12.4	87.5	809
4 mg	30.2	61.8	758
6 mg	42.1	45.2	796
8 mg	32.3	46.2	776

blue (30°C) and red (85°C) plots is only observed beyond 1300 nm (**Table III. 2**). Increasing the active particle loading to 4 mg/10 mL increases the maximum NIR suppression to 33.7%; however, the visible light transmittance is diminished to 58% and the onset of NIR suppression is red-shifted to 914 nm. Further increasing the nanocrystal loading to 6 mg/10 mL increases the NIR suppression to ca. 40% but further decreases the visible light transmittance to 42.8% and red-shifts the onset of NIR suppression to 926 nm, suggesting increasing agglomeration (and thereby a stronger scattering background). In general, increased nanocrystal loadings bring about more extensive agglomeration and gives rise to a larger temperature-invariant scattering background (as schematically depicted in the middle panel of the inset to Figure III. 1). Consequently, the NIR suppression is only discernible at higher wavelengths. Increasing the nanocrystal loading to still higher values diminishes the visible light transmittance without much of an increase of the NIR suppression. The spectral shapes discernible in Figure III. 6 suggest pronounced light scattering in these latter samples with the 30 and 85°C spectra diverging only at wavelengths >1300—1400 nm. This scattering background results from the strong agglomeration of the nanocrystals within the films in the absence of a method of dispersion. Indeed, Figure A. 9 plots still higher nanocrystal loadings and the relevant metrics are listed in Table A 1. More severe agglomeration is evidenced with a concomitant decrease of both the NIR suppression and the visible light transmittance; the onset of suppression is shifted to 978 nm for the 12 mg/10 mL dispersion.

As can be seen in Table III. 2, the primary enhancement of function afforded by surface functionalization combined with the use of a dispersant is an earlier onset of NIR suppression as compared to unfunctionalized as-prepared VO_2. The suppression of NIR and visible light transmittance of VO_2 and VO_2@-F nanocrystals are similar (Table III. 2); however, **Figure III. 7**

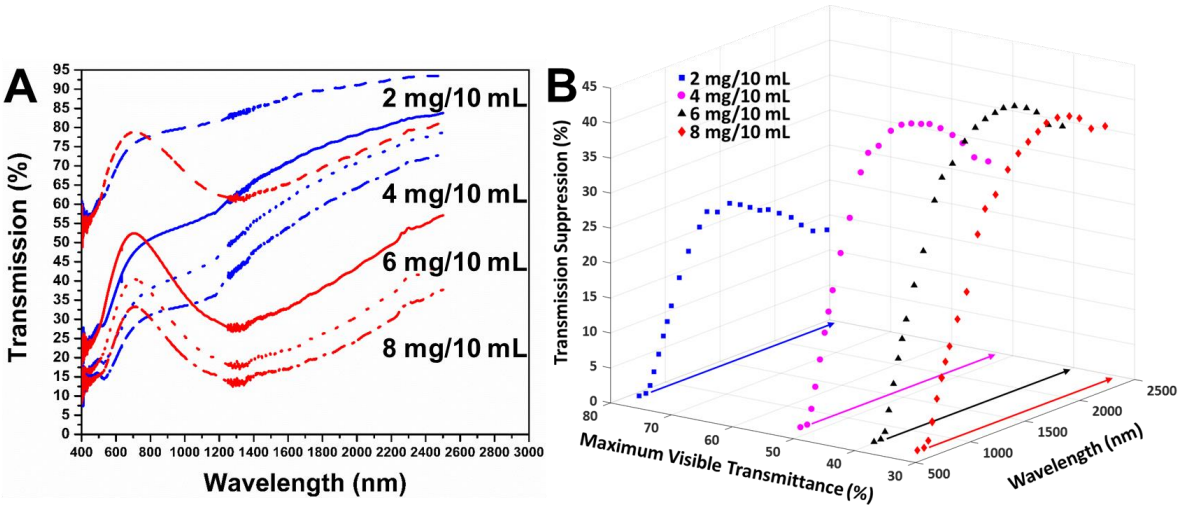

Figure III. 7 A) Absorption spectra acquired for four different loadings of VO_2@-F nanocrystals. The plots correspond to 2 mg (dashed lines), 4 mg (solid lines), 6 mg (dotted lines), and 8 mg (alternating dash-dot lines) dispersed in 10 mL of an aqueous dispersion of 1 wt.% (relative to 10 mL volume of water) methacrylic acid/ethyl acrylate copolymer cast onto borosilicate glass substrates. Spectra obtained at 30°C are displayed in blue, whereas spectra obtained at 85°C after equilibration for 10 min are shown in red. B) 3D representation of VO_2 optical data plots showing four nanocrystal loadings: 2 mg (blue squares), 4 mg (purple circles), 6 mg (black triangles), and 8 mg (red diamonds). Maximum visible transmission is the maxima in the visible region from each 85°C plot in (A) and is constant for each plot (represented by an arrow across the maximum visible transmittance/wavelength plane).

and Table III. 2 illustrate that functionalization of the VO_2 nanocrystals with (heptadecafluoro-1,1,2,2-tetrahydrodecyl)trimethoxysilane followed by dispersion with PFOS brings about a strong blue-shift of the onset of suppression; the spectral lineshapes are starkly altered as a result of the better dispersion of the nanocrystals, which strongly suppresses the scattering background. Two distinct advantages are realized as a result of this spectral shift: (i) more solar flux in the NIR is reflected upon metallization at high temperatures and (ii) the region of maximum NIR suppression is shifted nearer to the highest solar flux part of the spectrum.[71] It can be seen from the 3D graphs in Figure III. 6 for bare VO_2 nanocrystals, maximal suppression is not reached until ca. 2400—2500 nm (depending on the extent of loading); however, for perfluorinated VO_2

nanocrystals dispersed using PFOS (Fig. III. 7), the maximum suppression is achieved near 1600-1700 nm.

The substantially improved dispersion of VO_2@-F nanocrystals is furthermore evidenced by the relative constancy of the onset of NIR suppression with increasing nanocrystal loading (Table III. 2). Figure A. 10 and Table A. 2 (Appendix A) provide data on higher nanocrystal loadings. Interestingly, the better dispersion results in preservation of the extent of NIR

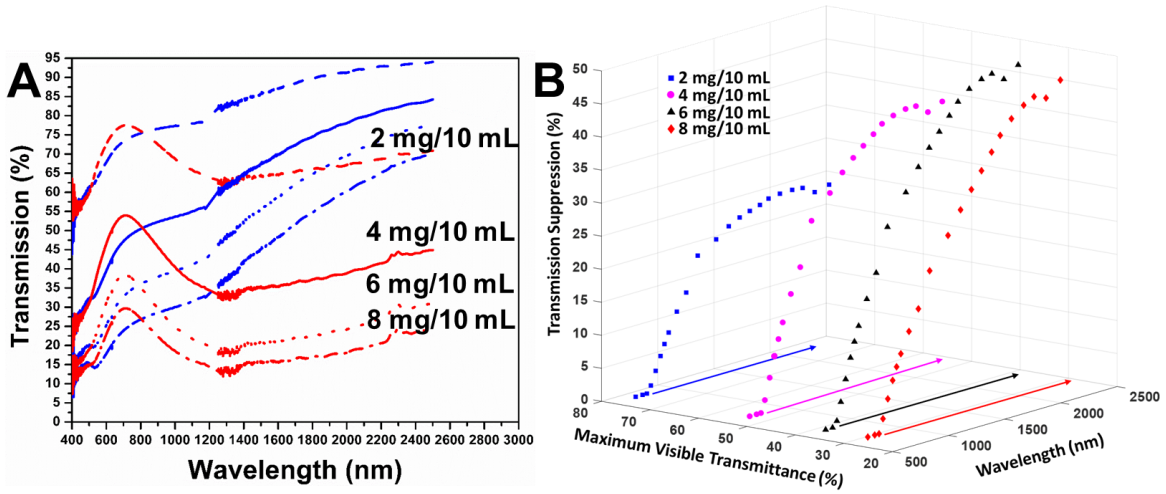

Figure III. 8 A) Absorption spectra acquired for four different loadings of VO_2@SiO_2 nanocrystals. The plots correspond to 2 mg (dashed lines), 4 mg (solid lines), 6 mg (dotted lines), and 8 mg (alternating dash-dot lines) dispersed in 10 mL of an aqueous dispersion of 1 wt.% (relative to 10 mL volume of water) methacrylic acid/ethyl acrylate copolymer cast onto borosilicate glass substrates. Spectra obtained at 30°C are displayed in blue, whereas spectra obtained at 85°C after equilibration for 10 min are shown in red. B) 3D representation of VO_2 optical data plots showing 4 nanocrystal loadings: 2 mg (blue squares), 4 mg (purple circles), 6 mg (black triangles), and 8 mg (red diamonds). Maximum visible transmission is the maxima in the visible region from each 85°C plot in (A) and is constant for each plot (represented by an arrow across the maximum visible transmittance/wavelength plane).

suppression even at high concentrations although some agglomeration is evidenced in the red-shift of the onset of NIR suppression. These compositions provide high NIR suppression but low visible-light transmittance performance that might be suitable for some applications wherein tinting and dynamic fenestration are desired at the same time.

Figure III. 8 plots the temperature-dependent optical characteristics of VO_2@SiO_2 nanocrystal s. As also listed in Table III. 2, the increased dispersion afforded by the SiO_2 shells results in a higher NIR suppression that approaches as much as 47%. However, the onsets of NIR suppression, while being substantially improved over bare VO_2 nanocrystals, are somewhat red-

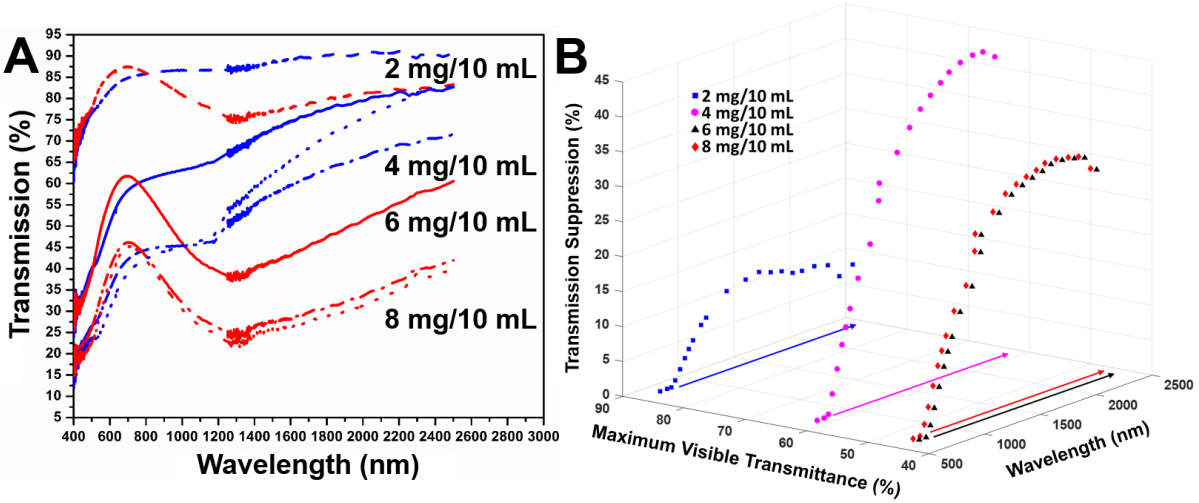

Figure III. 9 A) Absorption spectra acquired for four different loadings of VO_2@SiO_2-F nanocrystals. The plots correspond to 2 mg (dashed lines), 4 mg (solid lines), 6 mg (dotted lines), and 8 mg (alternating dash-dot lines) dispersed in 10 mL of an aqueous dispersion of 1 wt.% (relative to 10 mL volume of water) methacrylic acid/ethyl acrylate cast onto borosilicate glass substrates. Spectra obtained at 30°C are displayed in blue, whereas spectra obtained at 85°C after equilibration for 10 min are shown in red. B) 3D representation of VO_2 optical data plots showing 4 nanocrystal loadings: 2 mg (blue squares), 4 mg (purple circles), 6 mg (black triangles), 8 mg (red diamonds). Maximum visible transmission is the maxima in the visible region from each 85°C plot in (A) and is constant for each plot (represented by an arrow across the maximum visible transmittance/wavelength plane).

shifted from the VO_2@-F nanocrystals. As with the VO_2@-F nanocrystals, the pronounced NIR suppression is preserved even at higher loadings when the visible light transmission is diminished (Fig. A. 11 and Table A. 3, Appendix A). The slightly greater degree of agglomeration observed for VO_2@SiO_2 is attributed to the SiO_2 shells encapsulating multiple

VO_2 nanocrystals; in contrast, based on FTIR data (Fig. III. 4), the perfluorinated self-assembled monolayers allow for individual dispersion of the nanocrystals within the polymeric matrix.

A combination of both dispersion methods has also been attempted by silane functionalization of VO_2@SiO_2 nanocrystals to obtain VO_2@SiO_2-F nanocrystals. **Figure III. 9** and Table III. 2 indicate that this set of samples yields high NIR suppression of above 45% comparable to VO_2@SiO_2 samples and the onset of NIR suppression is further blue-shifted. In these samples, the VO_2 nanocrystals with dimensions of 44 ± 30 nm are protected by low-dielectric-constant SiO_2 shells, which in turn are encapsulated with perfluorinated self-assembled monolayers. The core—shell nanocrystals are homogeneously dispersed within the methacrylic acid/ethyl acrylate copolymer matrix with the help of PFOS allowing for thin films exhibiting large NIR suppression with onsets in the 760—800 nm regime. Furthermore, substantial enhancements of visible light transmittance are observed and the lineshapes in Figure III. 9 indicate that the scattering background is strongly suppressed. Higher loadings of VO_2@SiO_2-F nanocrystals are presented in Figure A .12 and Table A. 4, Appendix A. The low scattering background and strong NIR suppression is preserved even at higher loadings attesting to the excellent dispersion of the VO_2 nanocrystals. The combination of a SiO_2 shell for refractive index matching along with excellent dispersion facilitated by the perfluorinated silane and PFOS yields the most optimal combination of visible light transmittance, high NIR modulation, and early onset of NIR suppression.

The mechanical robustness of the nanocomposite films on borosilicate glass have further been evaluated using nanoindentation and ASTM adhesion tests.[43,44] **Figure III. 10** contrasts nanoindentation results for a methacrylic acid/ethyl acrylate film cast on glass with films

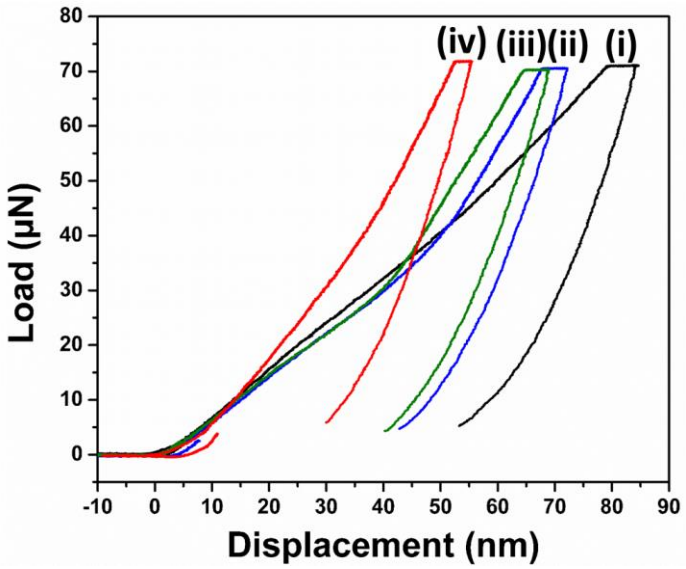

Figure III. 10 Load *versus* displacement curves acquired upon nanoindentation of methacrylic acid/ethyl acrylate film cast onto glass and nanocomposites embedded with three different particle sizes as described in Table III. 1 and Figure III. 5. All tests correspond to 4 mg/10 mL aqueous dispersions of 1 wt.% (relative to 10 mL volume of water) methacrylic acid/ethyl acrylate of each VO_2 size distribution. The plots correspond to (i) methacrylic acid/ethyl acrylate on glass without filler particles; (ii) 44 ± 30 nm nanocrystals; (iii) nanowires with lateral dimensions of 180 ± 70 nm and lengths of 1.6 ± 0.9 μm; (iv) nanowires with lateral dimensions of 210 ± 70 nm and lengths of 4.0 ± 3.0 μm.

embedded with 4 mg/10 mL dispersions of VO_2 nanocrystals of three different size distributions.

Table III. 3 plots values for the reduced modulus (E_r) (determined *via* the Oliver—Pharr method),[72,73] hardness, and stiffness recorded from 12 indentions in each film. Figure III. 10 and Table III. 3 indicate that the VO_2 nanocomposite films show an increase of the reduced modulus by 1.3—2.4 GPa, a concerted increase in hardness of about 25—44%, and an increase of stiffness by 0.2—0.7 μN/nm as compared to the methacrylic acid/ethyl acrylate film without particulate inclusions. These results suggest that incorporation of the inorganic filler yields stiffer and harder films, likely as a result of stabilization an interphase region at the particle/polymer interface.[37] Based on the standard deviations, the measured parameters do not appear to strongly depend on the particle dimensions.

Table III. 3: Summary of reduced modulus, hardness, and stiffness values measured for a methacrylic acid/ethyl acrylate film cast onto glass and nanocomposites embedded with three different particle sizes as described in Table III. 1 and Figure III. 5. All tests correspond to 4 mg/10 mL aqueous dispersions of 1 wt.% (relative to 10 mL volume of water) methacrylic acid/ethyl acrylate of each VO_2 size distribution. For each of the properties, the reported results reflect the average and standard deviation of twelve different measurements.

Nanocrystal size distribution (widths)	Reduced modulus (GPa)	Hardness (GPa)	Stiffness (μN/nm)
Methacrylic acid/ethyl acrylate	6.4 ± 0.40	$3.2 \times 10^{-1} \pm 0.014$	3.4 ± 0.19
44 ± 30 nm	8.0 ± 0.31	$4.6 \times 10^{-1} \pm 0.040$	3.6 ± 0.12
180 ± 70 nm	7.7 ± 1.1	$4.0 \times 10^{-1} \pm 0.13$	3.7 ± 0.18
210 ± 70 nm	8.8 ± 2.6	$4.4 \times 10^{-1} \pm 0.22$	4.1 ± 0.15

Further studies have been performed to evaluate the adhesion of the nanocomposite films to glass. A tape test has been conducted as specified by ASTM D3359;[43] the nanocomposite films are classified on a scale from 5B (indicating the highest level of adhesion wherein there is no visible loss of the coating upon peeling t he tape from the film) to 0B (poor adhesion, corresponding to removal of greater than 65% of the coating by the tape).[43] All the coatings are rated as 5B, indicating the overall excellent adhesion of the host matrix to glass. In addition, a scrape test has been performed as per ASTM D2197;[44] the results are classified based on the applied mass required for the "U"-shaped loop on the balanced beam scrape adhesion tester to break though the organic film and delaminate the film from the glass substrate.[44] All samples of varying nanoparticle size previously tested *via* tape test were rated by scrape test to withstand

scrape loads of >10 kg, the maximum limit tested under the specified method, further demonstrating the excellent adherence of the coatings to glass.

III.4 Conclusion

In summary, fenestration units that are able to adapt to changes in ambient temperature have the potential to bring about considerable energy savings in both residential and industrial buildings by dynamically modulating solar heat gain in response to the external temperature without requiring human intervention. VO_2 exhibits a reversible insulator to metal transition that is accompanied by a massive and dynamically switchable suppression of NIR transmittance and reflectance as a function of temperature. This phase transition can be utilized to limit NIR solar heat gain at high ambient temperatures, while allowing for use of solar heat gain to warm interiors at low ambient temperatures.

In this work, we demonstrate that nanocomposite thin films embedded with well dispersed <100 nm VO_2 nanocrystals are substantially able to mitigate Mie scattering characteristic of larger VO_2 particles and agglomerates, thereby yielding both high visible light transmittance, effective NIR suppression, and a low onset wavelength of NIR suppression. An entirely aqueous-phase process for preparation of nanocrystals and their effective dispersion within polymeric nanocomposites has been devised and allows for realization of viable plastic fenestration elements. The encapsulation of the VO_2 nanocrystals within an amorphous SiO_2 shell or a self-assembled perfluorinated silane ligand shell, facilitated by grafting of silanes to surface hydroxyl groups, protects the nanocrystals from oxidation and allows for their homogeneous dispersion within a pH-responsive methacrylic acid/ethyl acrylate copolymer matrix with the help of a surfactant. The VO_2@SiO_2-F formulations characterized by the most

efficacious refractive index matching and dispersion exhibit an optimal combination of high degree of visible light transmittance, high extent of NIR modulation and early onset of NIR suppression, considerably improved over bare VO_2 nanocrystals of the same particle size, which show a high tendency to agglomerate in the absence of surface functionalization. In contrast, VO_2@-F formulations also show excellent NIR suppression at an early onset but have a relatively lower visible light transmittance. The approach demonstrated here does not require organic solvents and is readily scalable to larger areas and arbitrary surfaces and represents a retrofittable option for modification of existing fenestration.

III.5 References

(1) UNEP. Buildings and Climate Change: Summary for Decision Makers. *Program. Sustain. Build. Clim.* **2009**, 1–62.

(2) Houvila, P. *UNEP. Buildings and Climate Change: Status, Challenges, and Opportunities*; UNEP/EarthPrint, 2007.

(3) Risser, R. *Making Smart Windows Smarter*; U.S. Department of Energy: Washington, DC 2011.

(4) Omer, A. M. Energy, Environment and Sustainable Development. *Renew. Sustain. Energy Rev.* **2008**, *12*, 2265–2300.

(5) U.S. Department of Energy. *Energy Efficiency Trends in Residential and Commercial Buildings*; U.S. DOE: Washington, DC, **2010**, pp 1− 52.

(6) Kanu, S. S.; Binions, R. Thin Films for Solar Control Applications. *Proc. R. Soc. A Math. Phys. Eng. Sci.* **2010**, *466*, 19–44.

(7) Granqvist, C. G. Electrochromic Materials: Out of a Niche. *Nat. Mater.* **2006**, *5*, 89–90.

(8) Wang, Y.; Runnerstom, E. L.; Milliron, D. J. Switchable Materials for Smart Windows. *Annu. Rev. Chem. Biomol. Eng.* **2016**, *7*, 283–304.

(9) Manning, T. D.; Parkin, I. P.; Clark, R. J. H.; Sheel, D.; Pemble, M. E.; Vernadou, D. Intelligent Window Coatings: Atmospheric Pressure Chemical Vapour Deposition of Vanadium Oxides. *J. Mater. Chem.* **2004**, *16*, 744–749.

(10) Hee, W. J.; Alghoul, M. A.; Bakhtyar, B.; Elayeb, O.; Shameri, M. A.; Alrubaih, M. S.; Sopian, K. The Role of Window Glazing on Daylighting and Energy Saving in Buildings. *Renew. Sustain. Energy Rev.* **2015**, *42*, 323–343.

(11) Barile, C. J.; Slotcavage, D. J.; McGehee, M. D. Polymer-Nanoparticle Electrochromic Materials That Selectively Modulate Visible and Near-Infrared Light. *Chem. Mater.* **2016**, *28*, 1439–1445.

(12) Runnerstrom, E. L.; Llordés, A.; Lounis, S. D.; Milliron, D. J. Nanostructured Electrochromic Smart Windows: Traditional Materials and NIR-Selective Plasmonic Nanocrystals. *Chem. Commun.* **2014**, *50*, 10555–10572.

(13) Zhou, J.; Gao, Y.; Zhang, Z.; Luo, H.; Cao, C.; Chen, Z.; Dai, L.; Liu, X. VO_2 Thermochromic Smart Window for Energy Savings and Generation. *Sci. Rep.* **2013**, *3*, 3029.

(14) Zylbersztejn, A.; Mott, N. F. Metal-Insulator Transition in Vanadium Dioxide. *Phys. Rev. B* **1975**, *11*, 4383–4395.

(15) Eyert, V. The Metal-Insulator Transitions of VO_2: A Band Theoretical Approach. *Ann. Phys.* **2002**, *11*, 659–704.

(16) Whittaker, L.; Patridge, C. J.; Banerjee, S. Microscopic and Nanoscale Perspective of the Metal-Insulator Phase Transitions of VO_2: Some New Twists to an Old Tale. *J. Phys.*

Chem. Lett. **2011**, *2*, 745–758.

(17) Qazilbash, M. M.; Brehm, M.; Chae, B.-G.; Ho, P.-C.; Andreev, G. O.; Kim, B.-J.; Yun, S. J.; Balatsky, A. V; Maple, M. B.; Keilmann, F.; et al. Mott Transition in VO_2 Revealed by Infrared Spectroscopy and Nano-Imaging. *Science.* **2007**, *318*, 1750–1753.

(18) Brito, W. H.; Aguiar, M. C. O.; Haule, K.; Kotliar, G. Metal-Insulator Transition in VO_2: A DFT+DMFT Perspective. *Phys. Rev. Lett.* **2016**, *117*, 056402.

(19) Horrocks, G. A.; Singh, S.; Likely, M. F.; Sambandamurthy, G.; Banerjee, S. Scalable Hydrothermal Synthesis of Free-Standing VO_2 Nanowires in the M1 Phase. *ACS Appl. Mater. Interfaces* **2014**, *6*, 15726–15732.

(20) Eyert, V. VO_2: A Novel View from Band Theory. *Phys. Rev. Lett.* **2011**, *107*, 016401.

(21) Qazilbash, M. M.; Tripathi, A.; Schafgans, A. A.; Kim, B.; Kim, H. Nano-Imaging of the Electronic and Structural Transitions in Vanadium Dioxide. *Phys. Rev. B* **2011**, *83*, 165108.

(22) Tao, Z.; Han, T.-R.; Mahanti, S.; Duxbury, P.; Yuan, F.; Ruan, C.-Y.; Wang, K.; Wu, J. Decoupling of Structural and Electronic Phase Transitions in VO_2. *Phys. Rev. Lett.* **2012**, *109*, 166406.

(23) van Veenendaal, M. Ultrafast Photoinduced Insulator-to-Metal Transitions in Vanadium Dioxide. *Phys. Rev. B* **2013**, *87*, 235118.

(24) Lopez, R.; Feldman, L. C.; Haglund, R. F. Size-Dependent Optical Properties of VO_2 Nanoparticle Arrays. *Phys. Rev. Lett.* **2004**, *93*, 177403.

(25) Driscoll, T.; Kim, H.-T.; Chae, B.-G.; Kim, B.-J.; Lee, Y.-W.; Jokerst, N. M.; Palit, S.; Smith, D. R.; Di Ventra, M.; Basov, D. N. Memory Metamaterials. *Science).* **2009**, *325*, 1518–1521.

(26) Patridge, C. J.; Whittaker, L.; Ravel, B.; Banerjee, S. Elucidating the Influence of Local Structure Perturbations on the Metal-Insulator Transitions of $V_{1-x}Mo_xO_2$ Nanowires: Mechanistic Insights from an X-Ray Absorption Spectroscopy Study. *J. Phys. Chem. C* **2012**, *116*, 3728–3736.

(27) Wang, N.; Duchamp, M.; Xue, C.; Dunin-Borkowski, R. E.; Liu, G.; Long, Y. Single-Crystalline W-Doped VO_2 Nanobeams with Highly Reversible Electrical and Plasmonic Responses Near Room Temperature. *Adv. Mater. Interfaces* **2016**, *3*, 1600164.

(28) Lee, S.; Cheng, C.; Guo, H.; Hippalgaonkar, K.; Wang, K.; Suh, J.; Liu, K.; Wu, J. Axially Engineered Metal − Insulator Phase Transition by Graded Doping VO_2 Nanowires. *J. Am. Chem. Soc.* **2013**, *135*, 4850–4855.

(29) Manning, T. D.; Parkin, I. P.; Blackman, C.; Qureshi, U. APCVD of Thermochromic Vanadium Dioxide Thin Films - Solid Solutions $V_{2-x}M_xO_2$ (M = Mo, Nb) or Composites VO_2: SnO_2. *J. Mater. Chem.* **2005**, *15*, 4560–4566.

(30) Whittaker, L.; Zhang, H.; Banerjee, S. VO2 Nanosheets Exhibiting a Well-Defined Metal–insulator Phase Transition. *J. Mater. Chem.* **2009**, *19*, 2968–2974.

(31) Baum, P.; Yang, D.-S.; Zewail, A. H. 4D Visualization of Transitional Structures in Phase Transformations by Electron Diffraction. *Science.* **2007**, *318*, 788–792.

(32) Cao, J.; Ertekin, E.; Srinivasan, V.; Fan, W.; Huang, S.; Zheng, H.; Yim, J. W. L.; Khanal, D. R.; Ogletree, D. F.; Grossman, J. C.; Wu, J. Strain Engineering and One-Dimensional Organization of Metal − Insulator Domains in Single-Crystal Vanadium Dioxide Beams. *Nat. Nanotechnol*. 2009, **4**, 732−737.

(33) Pelcher, K. E.; Crawley, M. R.; Banerjee, S. Silica-Shell Encapsulation and Adhesion of VO_2 Nanowires to Glass Substrates: Integrating Solution-Derived VO_2 Nanowires within

Thermally Responsive Coatings. *Mater. Res. Express* **2014**, *1*, 035014.

(34) Naoi, Y.; Amano, J. Optimization of VO_2 Nanowire Polymer Composite Thermochromic Films by Optical Simulation. *J. Appl. Phys.* **2016**, *120*, 235301.

(35) Jagtap, S. D.; Tambe, S. P.; Choudhari, R. N.; Mallik, B. P. Mechanical and Anticorrosive Properties of Non Toxic Coal-Tar Epoxy Alternative Coating. *Prog. Org. Coatings* **2014**, *77*, 395–402.

(36) Elmore, J. D.; Kincaid, D. S.; Komar, P. C.; Nielsen, J. E. Waterborne Epoxy Protective Coatings for Metal. *J. Coatings Technol.* **2002**, *74*, 63–72.

(37) Dennis, R. V; Patil, V.; Andrews, J. L.; Aldinger, J. P.; Yadav, G. D.; Banerjee, S. Hybrid Nanostructured Coatings for Corrosion Protection of Base Metals: A Sustainability Perspective. *Mater. Res. Express* **2015**, *2*, 032001.

(38) Li, W.; Ji, S.; Qian, K.; Jin, P. Preparation and Characterization of VO_2-$BaSO_4$ Composite Films with Enhanced Optical Properties in Thermochromic Field. *Ceram. Int.* **2015**, *41*, 5049–5056.

(39) Zhu, J.; Zhou, Y.; Wang, B.; Zheng, J.; Ji, S.; Yao, H.; Luo, H.; Jin, P. Vanadium Dioxide Nanoparticle-Based Thermochromic Smart Coating: High Luminous Transmittance, Excellent Solar Regulation Efficiency, and Near Room Temperature Phase Transition. *ACS Appl. Mater. Interfaces* **2015**, *7*, 27796–27803.

(40) Alivio, T. E. G.; Sellers, D. G.; Asayesh-Ardakani, H.; Braham, E. J.; Horrocks, G. A.; Pelcher, K. E.; Villareal, R.; Zuin, L.; Shamberger, P. J.; Arroyave, R.; et al. Postsynthetic Route for Modifying the Metal — Insulator Transition of VO_2 by Interstitial Dopant Incorporation. *Chem. Mater* **2017**, *29*, 5401–5412.

(41) Dow. *ACRYSOL: Rheology Modifiers*, Dow Coating Materials Product Solutions Guide;

Dow Europe GmbH: Horgen, Switzerland, **2013**; p 16.

(42) *Acrysol ASE-60 Alkali-Soluble Anionic Thickener*; Rohm and Haas: Philadelphia, PA, **2003**.

(43) ASTM. Standard Test Methods for Measuring Adhesion by Tape Test. *Annu. B. ASTM Stand.* **2009**, *06.01*, 1–8.

(44) ASTM. Standard Test Method for Adhesion of Organic Coatings by Scrape Adhesion. *Annu. B. ASTM Stand.* **2013**, *06.01*, 1–3.

CHAPTER IV

EPITAXIAL STABILIZATION VERSUS INTERDIFFUSION: SYNTHETIC ROUTES TO METASTABLE CUBIC HfO_2 AND HfV_2O_7 USING CORE—SHELL DISPOSITION OF PRECURSORS

IV.1 Introduction

Metastable crystal structures with atomic connectivities somewhat altered from the thermodynamic phase correspond to relatively shallower local minima on free energy landscapes as compared to the thermodynamic phase but can oftentimes be trapped under ambient conditions.[1–4] The large amounts of energy inputted in conventional ceramic and metallurgical processing methods result in reaction mixtures being able to efficiently approach equilibrium. In contrast, synthetic approaches that can situate the material in a local minimum under specific constraints (temperature, pressure, voltage, strain, chemical doping) can oftentimes be rapidly "quenched", enabling kinetic trapping of metastable atomic configurations.[3,5–11] Perhaps the most iconic example of a metastable material that can be isolated under ambient conditions is diamond, which exhibits a distinctly different bonding motif, and thus vastly different functionality, as compared to its thermodynamically stable counterpart, graphite.[12,13] Seminal work by Garvie several decades ago established synthetic routes to the stabilization of the metastable tetragonal polymorph of ZrO_2;[14] at nanoscale dimensions, the increased stabilization of the tetragonal polymorph derived from surface and strain energy differentials with the monoclinic polymorph overcomes the bulk free energy preference for the latter polymorph.[5,15] The transformation of metastable tetragonal ZrO_2 to the thermodynamically stable monoclinic polymorph provides an effective means of energy dissipation and is used industrially for

transformation toughening.[15–20] Recent work illustrates that the stabilization of tetragonal HfO_2 under ambient conditions is much more challenging and requires scaling to dimensions <4 nm as compared to the ca. 30 nm critical size for ZrO_2.[5,15,20] In this work, we describe a synthetic strategy for stabilizing the energetically still more disfavored cubic phase of HfO_2 under ambient conditions, which as per the binary Hf—O phase diagram is stable only above 2600°C.[21] The binary phase diagram of Hf—O reported by Shin et al. delineates cubic HfO_2 as a relatively small sliver stable only for oxygen stoichiometries between 0.5 and 0.7 mole fraction and in the temperature range between 2600°C and 2758°C whereupon it is congruently melted.[21] A combination of epitaxial growth of HfO_2 onto VO_2 nanocrystals and interdiffusion, followed by etching of the vanadium oxide core enables the stabilization of metastable cubic HfO_2 under ambient conditions. In contrast, annealing core—shell VO_2@HfO_2 nanocrystals under oxidative conditions promotes effective interdiffusion, stabilizing the negative thermal expansion material, HfV_2O_7.

HfO_2 and ZrO_2 are oftentimes referred to as the "twin oxides" owing to the similarities in the properties of these two materials that arises from the closely matched atomic radii of their cations, which indeed is a direct result of lanthanide contraction.[22–24] Under ambient conditions, hafnia crystallizes in a low-symmetry (seven-coordinated) monoclinic phase (M, space group $P2_1/c$) and exhibits a diffusionless Martensitic transition to a higher-symmetry (eight-coordinated) tetragonal structure (R, space group $P4_2/nmc$) at a temperature of ca. 1720°C.[5,15] An even higher symmetry (still with eight-coordinated hafnium atoms) cubic phase (C, space group $Fm\bar{3}m$) is stabilized at temperatures above 2600°C and is retained until hafnia is congruently melted at a temperature of 2758°C.[5,25–27] Traversing the free energy landscape along the pressure axis reveals two oxygen-deficient orthorhombic variants, orthorhombic I (O1, space group

*Pca*2$_1$), which is stabilized above 4.3 GPa and orthorhombic II (O2, space group *Pmn*2$_1$), which is observed above 14.5 GPa.[26,28] The dielectric constant of monoclinic HfO_2 is in the vicinity of 18, higher than that of SiO_2, whereas tetragonal and cubic polymorphs are predicted to have dielectric constants as high as 70 and 30, respectively.[5,15,24]

By reacting $HfCl_4$ with hafnium(IV) *tert*-butoxide ($Hf(O^tBu)_4$) with the addition of low concentrations of the less reactive cerium(IV) *tert*-butoxide and lanthanum(III) isopropoxide, we have recently separated nucleation and growth steps, enabling the stabilization of HfO_2 nanocrystals with dimensions <10 nm.[15] The development of this synthetic route reveals the critical threshold for stabilizing tetragonal HfO_2 as being 3.6—3.8 nm.[15] Another approach to stabilization of tetragonal HfO_2 involves the introduction of multiple nanotwinned domains within the monoclinic variant; the twin planes serve to nucleate the transformation dislocation and mediate stabilization of the tetragonal phase at temperatures more than 1000°C lower than the bulk transformation temperature[5,29] While these efforts have enabled stabilization of the technologically important tetragonal polymorph of HfO_2, the higher temperature cubic phase remains difficult to access. Aliovalent doping has been utilized to stabilize cubic HfO_2 but requires dopant concentrations as high as 11.0 and 3.00 at.% for V and La, respectively. Intriguingly, lanthanum-doped cubic HfO_2 exhibits a remarkably high dielectric constant of 38.[30,31] While dimensional confinement and twin domain control have emerged as viable means of accessing the tetragonal phase of HfO_2, an altogether new strategy is required to stabilize the cubic polymorph of HfO_2 and is demonstrated here based on a core—shell precursor strategy. The intimate mixing and small diffusion lengths within core-shell VO_2@HfO_2 nanocrystals enables the facile stabilization of phase-pure cubic HfO_2 at low temperatures. In contrast, facilitating interdiffusion under oxidative conditions yields HfV_2O_7, a negative thermal

expansion (NTE) material in the MX_2O_7 material family that exhibits isotropic negative thermal expansion.[32–35] The development of a facile synthetic route to this material further mitigates a major impediment to its industrial use within zero thermal expansion composites.

IV.2 Experimental

Synthesis of VO_2 Nanocrystals: VO_2 nanowires with lateral dimensions of 180±70 nm and lengths of 1.6±0.9 μm have been prepared by the hydrothermal reduction of V_2O_5 with acetone as reported in previous work.[36–38] Briefly, 1.60 mg V_2O_5, 42.0 mL acetone, and 33.0 mL of deionized water (ρ=18.2 MΩ·cm, Barnstead Water Purification System) were placed in a 125 mL polytetrafluoroethylene vessel, which in turn was placed within a sealed hydrothermal reactor and maintained at 210°C for 72 h.[36–38] The recovered solid was filtered and washed three times with water and subsequently three times with acetone. The recovered powder was then dried and annealed within a tube furnace under a flow of Ar gas (50 sccm); the furnace was heated to 550°C at a heating rate of ca. 43°C/min and held at this temperature for 5 h. The annealed solid, VO_2 nanowires crystallized in the M1 phase, was then removed and used as prepared.

Quasi-spherical VO_2 nanocrystals with a diameter of 44±30 nm have been prepared by an alternative sol—gel condensation and hydrothermal treatment route.[36,37,39,40] Briefly, $VO(OH)_2$ was precipitated from the reaction between NH_4VO_3 and N_2H_4 in deionized water at a temperature of 80°C. The solid precipitate was then heated at 210°C for 24 h within the hydrothermal apparatus described above. The recovered powder was washed with copious amounts of water and acetone across three cycles of resuspension and centrifugation.

Deposition of HfO_2 onto VO_2 Nanocrystals: Amorphous HfO_2 shells were deposited onto nanowires and quasi-spherical nanocrystals of VO_2 through a hydrolysis approach

analogous to the Stöber method for the preparation of SiO_2 shells.[36,37,41,42] In the first step, 30 mg of nanowires or quasi-spherical nanocrystals of VO_2 crystallized in the M1 phase were dispersed in 80 mL dry ethanol (dried over molecular sieves with 4Å pore size and Na_2SO_4) *via* ultrasonication (Branson 5510) for ca. 10 min. The colloidal dispersion was then placed within a three-neck round-bottomed flask, which was attached to an Ar Schlenk line and cooled using an ice bath. $Hf(O^tBu)_4$ was added dropwise to the ethanol dispersion at a molar ratio of VO_2:$Hf(O^tBu)_4$ of 1:0.5 under an Ar ambient; the reaction mixture was then allowed to stir for 20 min. This dispersion was then removed from the ice bath, placed on a heating mantle, and heated to 80°C while maintaining an Ar ambient. Next, 20 mL of a 1:20 (*v*/*v*) H_2O:EtOH mixture was added dropwise to initiate hydrolysis of the hafnium alkoxide. The low water content precludes homogeneous nucleation of HfO_2 nanocrystals in solution and constrains HfO_2 deposition to the surfaces of the VO_2 nanocrystals. The reaction mixture was maintained at 80°C for 15 min and subsequently removed from heat and allowed to cool to ca. 50°C before moving to centrifugation. The solid precipitate was then recovered by centrifugation at 8700 rpm using a Heraeus Megafuge 8. The recovered solid was resuspended in ethanol and recovered by centrifugation at 8700 rpm. Two such cycles were performed. Dry samples were annealed in a quartz tube placed within a tube furnace under 50 sccm of flowing Ar at 650°C for 25 min. The annealed powder was then allowed to cool to room temperature before further analysis.

Stabilization of Cubic HfO_2 by Dissolution of the V_2O_3 Core of V_2O_3@HfO_2 Core—shell Nanocrystals: After annealing to obtain V_2O_3@HfO_2 core—shell nanocrystals, the vanadium oxide shell was etched in acid solution to stabilize cubic HfO_2. Specifically, V_2O_3@HfO_2 core—shell nanocrystals were placed in a 5.67 M aqueous solution of HCl at a concentration of 1 mg solid per mL of solution. The prepared dispersion had a pH <1, which

results in the dissolution of V_2O_3 and remnant VO_2 from the core.[43] The acid-treated sample was sonicated vigorously for ca. 1 h to ensure dissolution of the core. The supernatant turned light blue in color indicating the stabilization of vanadium oxide clusters.[44] The solid was then recovered by centrifugation at 8700 rpm. The recovered solid was subsequently redispersed in ethanol and collected by centrifugation at 8700 rpm two times before being allowed to dry at room temperature.

Synthesis of HfV_2O_7: VO_2@HfO_2 core—shell nanocrystals were prepared as discussed above and the recovered powders were placed in a quartz tube and annealed under a static air ambient within a tube furnace ramping at a rate of 20°C/min to 650°C. The furnace was maintained at 650°C for 25 min. The recovered solid was light orange in appearance and was analyzed upon cooling to room temperature.

Characterization: Low-magnification transmission electron microscopy (TEM) images were recorded on a JEOL JEM-2010 instrument operated with an accelerating voltage of 200 kV. Atomic-resolution TEM images were recorded on an FEI Tecnai G2 F20 ST FE-TEM at Texas A&M University and a Nion UltraSTEM 200 microscope at Oak Ridge National Laboratory. Samples were dropcast onto copper grids after dispersion in hexanes (e-chips in the case of the Nion UltraSTEM). Both instruments were operated at an accelerating voltage of 200 kV. Scanning electron microscopy (SEM) images were recorded on a JEOL JSM-7500F field-emission scanning electron microscope set at an accelerating voltage of 10 kV.

In-situ powder X-ray diffraction (XRD) experiments were performed using a Bruker D8-Vario X-ray powder diffractometer using a Cu Kα (λ=1.5418Å) source operated at a 40 kV accelerating voltage with a 40 mA current. An MTC oven attachment was used for the heating experiments, which were performed under a flowing N_2 (40 sccm) environment, with patterns

recorded at 50°C intervals. Refinements of powder XRD patterns were performed for patterns recorded using a Bruker D8 Advance Eco X-Ray powder diffractometer with a Cu Kα (λ=1.5418Å) source scanning at 1.9°/min.

Neutron Activation Analysis (NAA) was performed using the Texas Engineering and Experiment Station 1-MW TRIGA reactor. Neutron irradiations of 30 s were performed at a thermal neutron fluence rate of 9.1 x 10^{12} cm^{-2} s^{-1}. Gamma-ray spectra were obtained using an HPGe detector for 500 s after a 270 s decay interval. Data analysis was performed using software from Canberra Industries.

IV.3 Results and Discussion

Stabilizing Metastable Cubic HfO_2: VO_2 nanowires with lateral dimensions of 180±70 nm and lengths of 1.6±0.9 μm have been prepared by the acetone reduction of V_2O_5 under hydrothermal conditions as discussed in detail in the Methods section.[36–38] Quasi-spherical VO_2 nanocrystals with diameters of 44±30 nm have been prepared by sol—gel reduction—condensation of NH_4VO_3 with hydrazine followed by hydrothermal treatment, as also discussed in the Methods section.[36,37,39,40] **Figures A 13A** and **B** (Appendix A) show representative transmission electron microscopy (TEM) images of the as-prepared VO_2 nanowires and quasi-spherical nanocrystals, respectively. **Figure A 13C** plots their corresponding powder X-ray diffraction (XRD) patterns, attesting to the crystallization of both the nanowires and the nanocrystals in the monoclinic M1 phase. Pronounced Scherrer broadening is observed in the XRD pattern acquired for ultrasmall VO_2 nanocrystals owing their small X-ray coherent domain sizes.

Figure IV. 1 schematically illustrates the synthetic approach to core—shell disposition of the precursors and the process used to prepare metastable cubic HfO_2 and the negative thermal

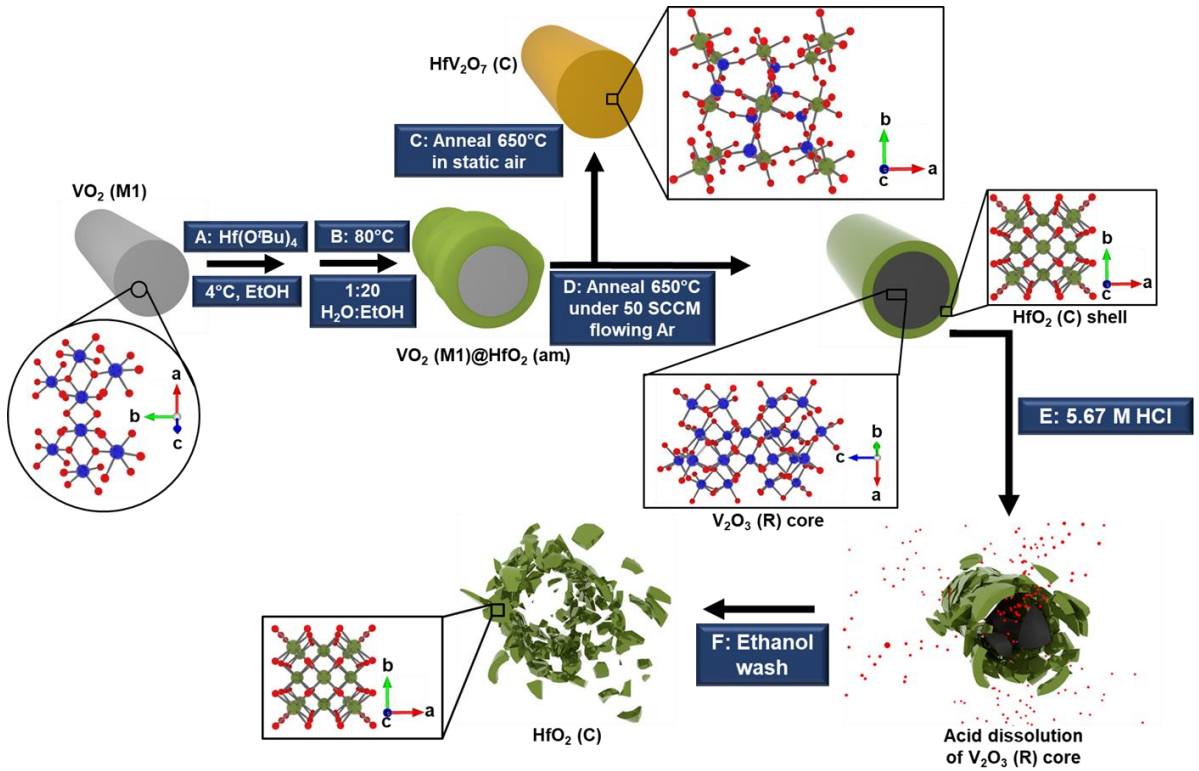

Figure IV. 1 Schematic depiction of the synthesis of cubic HfO_2 and HfV_2O_7 from VO_2 and HfO_2 precursors arranged in a core—shell disposition. A) $Hf(O^tBu)_4$ is deposited on the surface of M1 VO_2 and hydrolyzed in B) to deposit an amorphous HfO_2 shell onto the M1 VO_2 nanowires and nanocrystals. The VO_2@amorphous-HfO_2 core—shell structures can either be C) annealed under static air at 650°C to yield cubic HfV_2O_7, or D) annealed under flowing Ar to produce rhombohedral V_2O_3 with a cubic HfO_2 shell. E) Acid treatment of V_2O_3@HfO_2 with 5.67M HCl results in the dissolution of the V_2O_3 core and after F) washing with ethanol yields phase-pure cubic HfO_2 that is recovered upon centrifugation.

expansion material, HfV_2O_7. An amorphous HfO_2 shell is first deposited onto VO_2 nanocrystals or VO_2 nanowires by hydrolysis and condensation of a hafnium alkoxide precursor as per **Equation IV. 1**:

$$Hf(OR)_4(l) + 2H_2O(l) + VO_2(s) \rightarrow VO_2@HfO_2(s) + 4ROH\ (aq.) \qquad \text{(IV. 1)}$$

This reaction is performed at low temperature (4°C) to prevent homogeneous nucleation of HfO_2 nanocrystals. The abundant hydroxyl groups on the surfaces of the VO_2 nanocrystals allow for formation of V-O-Hf oxo linkages as observed previously in the deposition of SiO_2 shells.[36,37]

Figure A 14 shows room-temperature powder XRD patterns acquired along the synthetic scheme sketched in Figure 1 providing evidence for the phase assignments. Figure 14B shows the appearance of a diffuse scattering background upon deposition of an amorphous HfO_2 shell onto the VO_2 nanowires. Annealing in Ar to 650°C results in the emergence of rhombohedral V_2O_3 (PDF: 85-1411) and cubic HfO_2 (refined parameters) phases (Fig. A 14C), illustrating oxygen diffusion from the core to the shell consistent with the more electropositive nature of hafnium. Acid etching of the core—shell structure leaves behind cubic HfO_2 as the only crystalline phase (Fig. A 14D). No HfV_2O_7 contamination is observed for materials obtained by this method.[31] **Figure A 15** shows powder XRD patterns acquired along the same sequence of reactions for quasi-spherical VO_2 nanocrystals.

Figures IV. 2A and **B** shows TEM and scanning electron microscopy (SEM) images of bare VO_2 nanowires and the nanowires encased by an amorphous HfO_2 shell, respectively. **Figure IV. 2C** shows the nanowires after annealing under Ar at 650°C for 25 min; oxygen diffusion from the core to the shell results in reduction of M1 VO_2 to rhombohedral V_2O_3 and yields V_2O_3@HfO_2 core—shell particles with a cubic HfO_2 shell. The SEM image in Figure IV. 2C reveals that the shell is polycrystalline with faceted plate-like crystallites protruding from the surface of the nanowires. **Figure IV. 2D** shows cubic HfO_2 nanocrystals after acid etching of the rhombohedral V_2O_3 core. **Figure A 16** (Appendix A) shows analogous images across the sequence of reactions for quasi-spherical VO_2 nanocrystals.

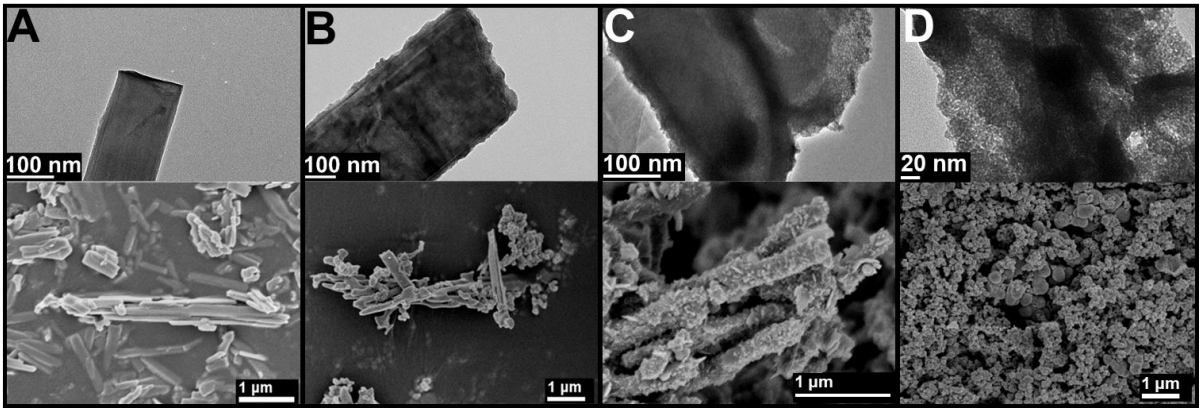

Figure IV. 2 TEM and SEM images corresponding to synthetic steps involved in the stabilization of cubic HfO_2. A) TEM image (top) and SEM image (bottom) of M1-phase VO_2 nanowires prepared by the hydrothermal reduction of V_2O_5 by acetone. B) TEM and SEM images of VO_2 nanowires coated with an amorphous HfO_2 shell. C) TEM and SEM images of V_2O_3@cubic-HfO_2 core—shell structures obtained upon annealing VO_2@amorphous-HfO_2 structures at 650°C. D) TEM and SEM image of polycrystalline cubic HfO_2 after acid etching of the V_2O_3 core.

Figures IV. 3A and **B** show low-magnification TEM images of core—shell V_2O_3@HfO_2 nanowires obtained upon annealing alongside an energy-dispersive X-ray spectroscopy (EDX) map illustrating the core—shell disposition of the vanadium and hafnium oxide domains. Figure IV. 3A shows a panoramic view, whereas Figure IV. 3B exhibits a cross-sectional image and EDX map acquired for an ultramicrotomed nanowire.

This image shows that vanadium (red) is concentrated within the core of the structure, whereas hafnium (green) is concentrated w ithin the shell. Further evidence of the core—shell structure comes from **Figure A 17**, which shows a cross-sectional view of an ultramicrotomed nanowire as well as an EDX line scan that further confirms the core—shell structure with Hf concentrated within the shell and vanadium within the core. Some V content is detected within the shell likely derived from the outwards diffusion of vanadium cations facilitated by the reasonable miscibility of the two cations.[31] The lattice-resolved HRTEM images in **Figures IV. 3C** and **D** demonstrate the epitaxial matching between the rhombohedral V_2O_3 core and cubic

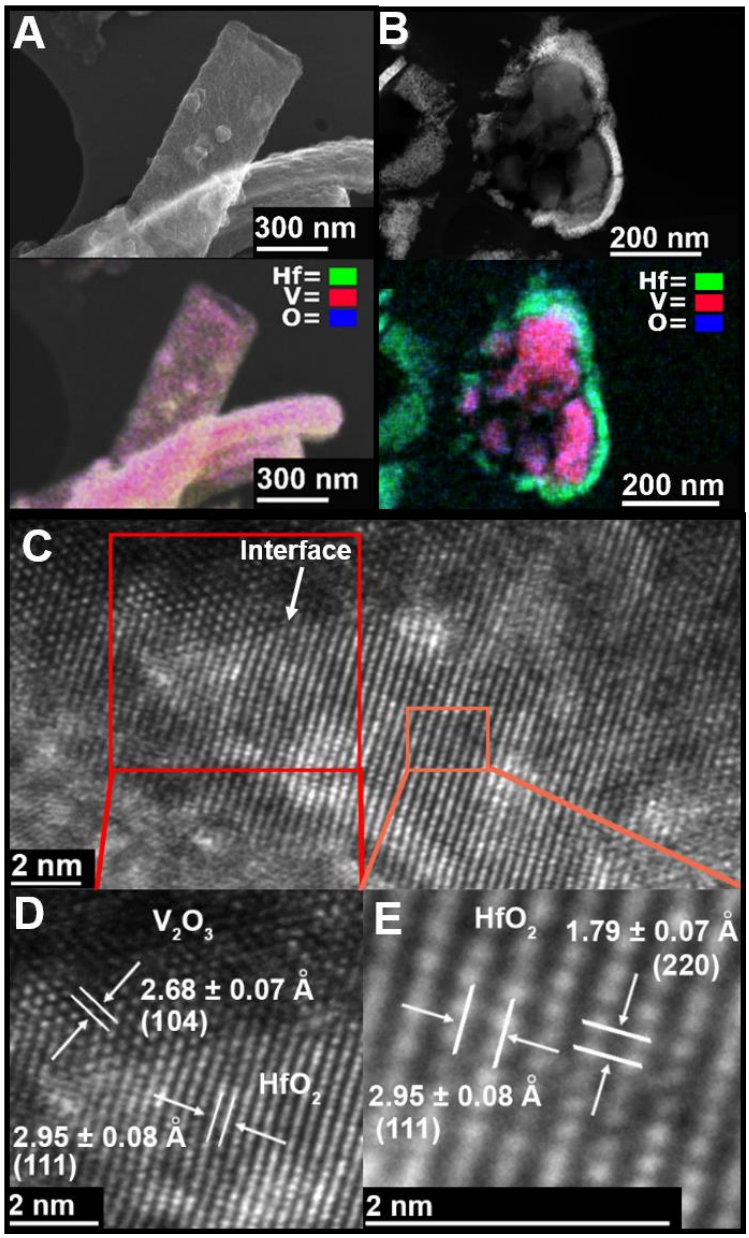

Figure IV. 3 Imaging and compositional mapping of V_2O_3@HfO_2 core—shell structures. A) TEM image of annealed V_2O_3@HfO_2 and corresponding EDX map illustrating the vanadium oxide core surrounded by a hafnium oxide shell. B) Cross-sectional TEM image and EDX map of an ultramicrotomed core—shell nanowire. It is apparent that V (red) is highly concentrated within the core, whereas the Hf signal (green) is concentrated along the shell. C,D) High-resolution TEM images depicting the epitaxial interface between rhombohedral V_2O_3 and cubic HfO_2. Lattice spacings corresponding to rhombohedral V_2O_3 (PDF 85-1411) and cubic HfO_2 are delineated. E) A magnified image of cubic HfO_2 domains within the shell.

HfO_2 shell. **Figures IV. 3D** and **E** delineate the lattice planes. Indeed, this epitaxial matching is

critical to the nucleation of cubic HfO_2. Recent work has illustrated that a metastable polymorph can be preferentially stabilized if the barrier to nucleation of a metastable polymorph is lower than that of the thermodynamic phase.[45,46] The rhombohedral V_2O_3 core essentially selects for the preferential formation of cubic HfO_2 as compared to other HfO_2 polymorphs owing to the available epitaxial relationship as well as the influence of vanadium incorporation. Interestingly, while the epitaxial relationship likely underpins nucleation of cubic HfO_2, the lattice mismatch is sufficiently large such as to bring about strain-induced delamination of the V_2O_3 core from the HfO_2 shell (**Figs**. **IV. 3B** and **A 17**).

Figure IV. 4 plots intensity modulation maps illustrating the evolution of the powder XRD patterns of VO_2@amorphous HfO_2 core—shell structures as a function of temperature upon annealing under a N_2 ambient. Reflections corresponding to the M1 phase of VO_2 disappear rather abruptly at ca. 590—600°C and reflections that can be indexed to cubic HfO_2 emerge in the temperature range of 560—675°C. The crystallization and reduction of VO_2 to V_2O_3 occurs in concert and involves oxygen diffusion along a gradient of electropositivity. Figure 4B shows the results of an identical reaction performed without the presence of VO_2. Initially nucleated cubic/tetragonal domains are lost and the thermodynamically stable monoclinic phase of HfO_2 is stabilized as a result of grain growth.[5,15–17,25] The epitaxial relationship between V_2O_3 and cubic HfO_2 in the crystalline core—shell structures is therefore critical to preventing reversion to the thermodynamically stable monoclinic polymorph at elevated temperatures.

HfO_2 exhibits high stability in aqueous media across a wide pH range; in contrast, V_2O_3 is readily dissolved in acidic media.[43] This difference in reactivity provides a means of isolating free-standing cubic HfO_2 powders. The V_2O_3 cores of V_2O_3@HfO_2 core—shell structures have been

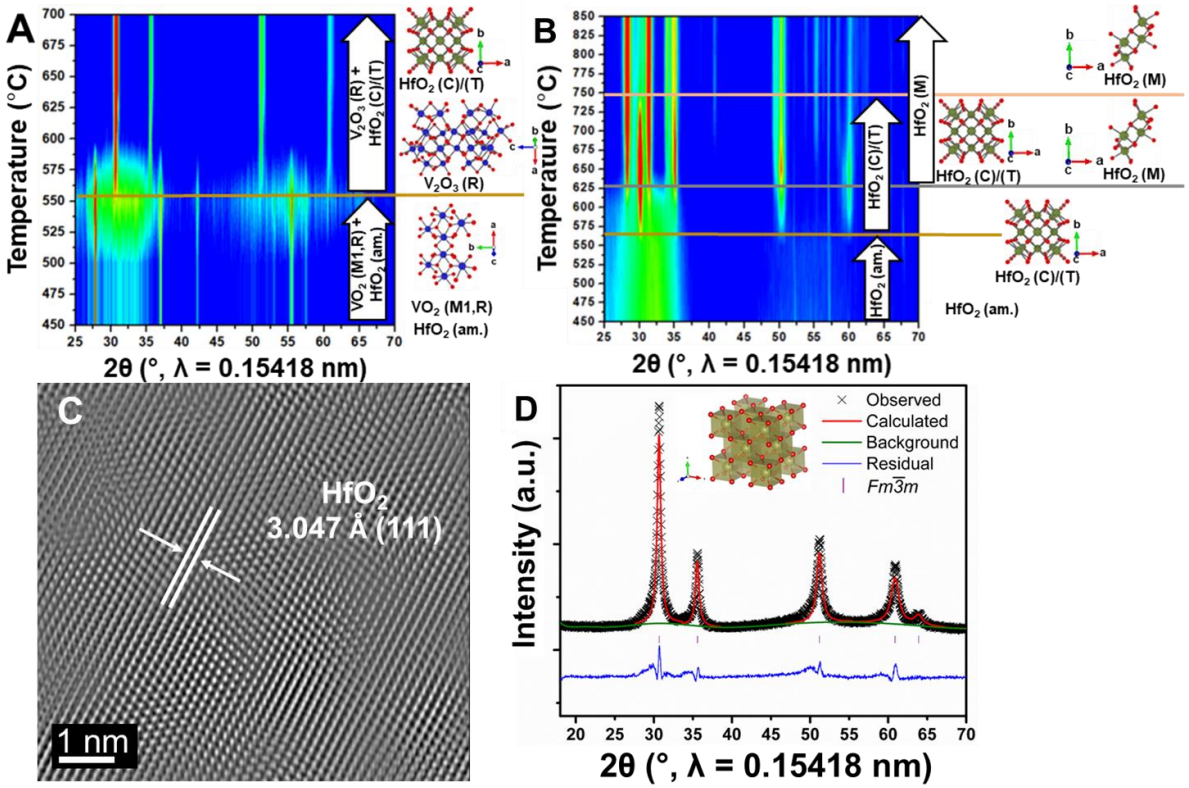

Figure IV. 4 Temperature-dependent XRD patterns and structure refinement. A) Evolution of XRD patterns of VO_2@amorphous HfO_2 with increasing temperature. The (011) reflection of M1 VO_2 is attenuated as the (111) reflection for cubic hafnia begins to reach maximum intensity between 560 and 600°C. Crystal structures of the phases that are predominant within each temperature range are illustrated alongside the intensity map. B) Evolution of the powder XRD pattern in a control experiment omitting the VO_2 nanowires. Initially stabilized tetragonal/cubic HfO_2 domains disappear rapidly with sintering; the thermodynamically stable monoclinic phase of HfO_2 emerges as the dominant species. C) HRTEM image of the cubic HfO_2 lattice. D) Observed XRD pattern (black crosses) plotted along with a refinement to cubic HfO_2. The simulated XRD pattern is displayed in red, background in green, and residual curve in blue; 2θ positions of reflections are marked as purple ticks. The structure refines to cubic HfO_2 crystallized in the $Fm\bar{3}m$ space group (see Table A 5 for refinement metrics).

etched in acid solution at room temperature, thereby preserving the metastable cubic structure of the shell. Refinement of the powder XRD pattern provides corroboration of the cubic crystal structure, which crystallizes in the *Fm3̄m* space group with a lattice constant of a = 5.04793(22) Å

(Figure IV. 4D and Table A 5), consistent with the lattice spacing directly imaged in Figures IV. 3D, 3E, and 4C. The recovered materials are phase pure.

Neutron activation analysis (NAA) quantification of the recovered solids reveals a V concentration of ca. 7.18±0.17 at.%, likely derived from the diffusion of vanadium atoms from within the core given the reasonable solubility of vanadium within the hafnia lattice. Notably, vanadium incorporation alone cannot account for stabilization of the metastable cubic polymorph; previous studies have indicated the need for at least 11 at.% V dopant incorporation to stabilize cubic HfO_2, which is observed to further be contaminated by HfV_2O_7.[31,47] The stabilization of free-standing cubic hafnia thereby provides access to a metastable kinetically trapped polymorph that is otherwise only accessible at temperatures above 2600°C. The cubic HfO_2 remains stable for over 12 months without transforming to metastable tetragonal or thermodynamically stable monoclinic polymorphs.

Synthesis of Negative Thermal Expansion HfV_2O_7: Conventional routes to the synthesis of HfV_2O_7 employ the grinding and sintering at 700°C of hafnyl oxalic acid and ammonium oxodioxalato-vanadium nH_2O complexes in precise stoichiometric amounts.[32] Other methods require copious amounts of organic solvents.[48]

As illustrated in Figure 1, annealing VO_2@amorphous-HfO_2 core—shell nanowires under static air instead of Ar yields HfV_2O_7 by dint of an interdiffusion reaction (albeit without preservation of the nanowire morphology) as per:

$$4VO_2(s) + 2HfO_2(s) + O_2(g) \rightarrow 2HfV_2O_7(s) \qquad \text{(IV. 2)}$$

The reaction is strongly enthalpically favored and entropically disfavored. As such, a lower reaction temperature is imperative to facilitate high reaction yields but requires mitigating

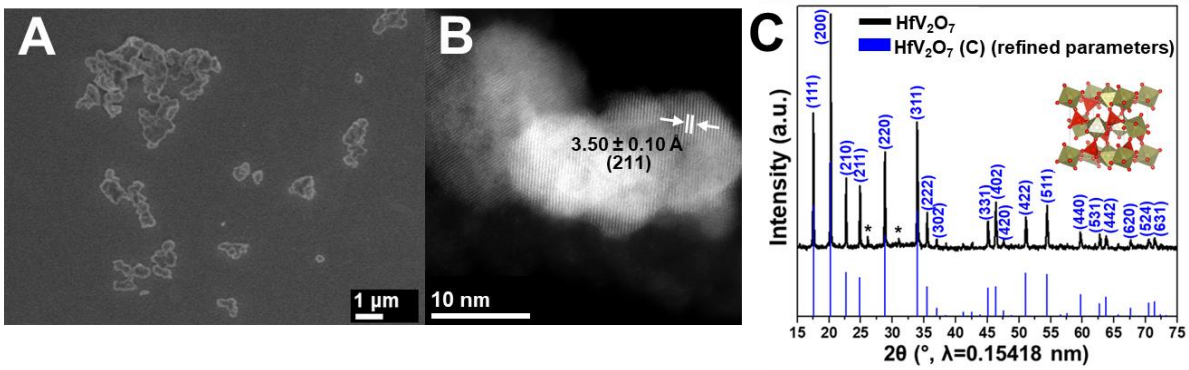

Figure IV. 5 Synthesis of HfV_2O_7. A) SEM image of HfV_2O_7 and B) high-resolution HAADF TEM image of HfV_2O_7. The interplanar separation between (211) planes of HfV_2O_7 are clearly discernible. C) XRD pattern of cubic HfV_2O_7 synthesized by annealing of VO_2@amorphous-HfO_2 structures in air. The sample displays a high degree phase purity with some remnant V_2O_5 (asterisked reflections). The pattern is indexed to refined HfV_2O_7 (C) parameters

kinetic impediments to mixing of the precursors. The core-shell disposition of precursors outlined here allows for facile interdiffusion at relatively low temperatures enabling high conversion yields. **Figure IV. 5** shows SEM and TEM images and an XRD pattern indicating the synthesis of HfV_2O_7. The core-shell structuring of precursors thus represents a facile low-temperature route for the stabilization of HfV_2O_7, which is an isotropic negative thermal expansion material.

Figure IV. 6 shows variable-temperature powder X-ray diffraction data acquired for the HfV_2O_7 materials obtained by this approach.[31,32,34] The evolution of two prominent reflections, (440) and (422), is shown in **Figure IV. 6**. For both sets of reflections, a shift of 2θ to lower values is initially observed (until a temperature of 150°C), followed by a subsequent increase to

higher 2θ values up to 700°C. The initial increase and subsequent decrease of interplanar lattice separation with increasing temperature is indicative of the straightening of VO_3—O—VO_3 bonds and the subsequent transverse, volume-reducing oscillations of said bonds.[31,32,34] The negative thermal expansion behavior is observed to be entirely reversible in the cooling panels of **Figure IV. 6**.[31,32,34]

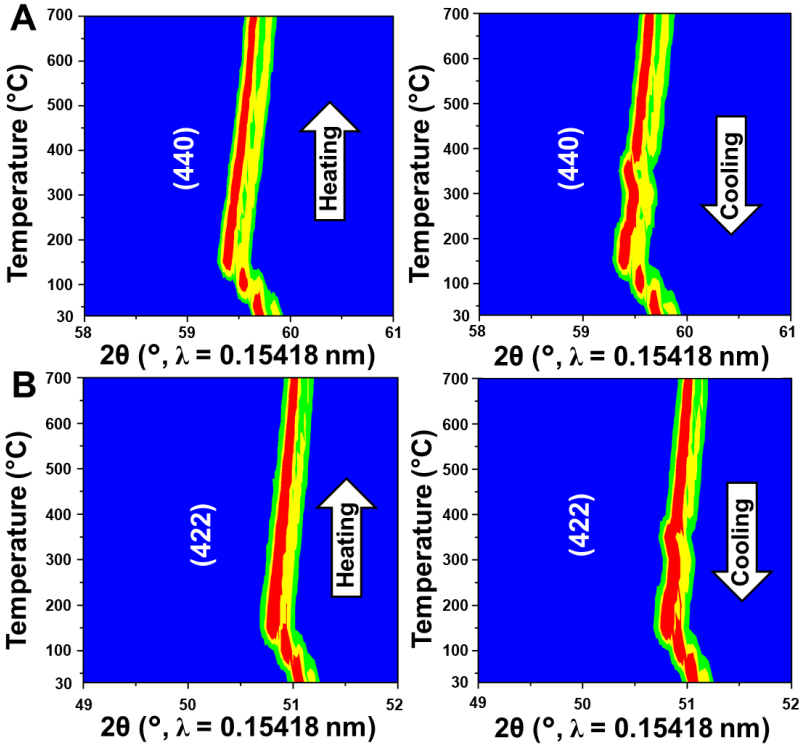

Figure IV. 6 A) In situ temperature-variant powder XRD of HfV_2O_7 illustrating NTE behavior. Intensity modulation plots for A) (440) and B) (422) reflections of HfV_2O_7 plotted as a function of temperature. Shifts to lower and higher 2θ represent lattice expansion and compression, respectively. The right panels indicate the entirely reversible alteration of lattice constants upon cooling.

IV.4 Conclusion

In summary, we have demonstrated a facile low-temperature synthetic route for stabilizing the metastable cubic phase of HfO_2 under ambient conditions utilizing the epitaxial relationship between rhombohedral V_2O_3 (generated *in situ* from reduction of VO_2 as a result of oxygen diffusion) and cubic HfO_2.[3,49] Oxygen diffusion proceeds from the VO_2 core to the amorphous HfO_2 shell owing the more electropositive nature of the latter; the available epitaxial relationship along with incorporation of vanadium atoms reduces the barrier to nucleation of the cubic polymorph notwithstanding its metastable nature and allows for its preservation at elevated temperatures wherein sintering and grain growth strongly favors stabilization of the monoclinic phase.[45,46] The epitaxial synthesis route thus serves as a valuable addition to strategies such as size reduction and introduction of twin domains used to stabilize metastable polymorphs of HfO_2.[5,15]

The disposition of VO_2 and HfO_2 in a core—shell structure further provides a direct solid-state synthetic route to cubic HfV_2O_7, a technologically important, yet notoriously difficult to synthesize, negative thermal expansion material.[32,33,35] The core-shell disposition of precursors allows for this entropically disfavored reaction to be performed at low temperatures with excellent conversion. Variable-temperature powder XRD measurements show pronounced negative thermal expansion behavior in the range between 150 and 700°C.[3,50] Future work will focus on experimentally determining the dielectric constant of this polymorph as well as exploring epitaxial relationships with the rich available repertoire of VO_2 polymorphs to stabilize other metastable variants of HfO_2.

IV.5 References

(1) Navrotsky, A. Nanoscale Effects on Thermodynamics and Phase Equilibria in Oxide

Systems. *ChemPhysChem* **2011**, *12*, 2207–2215.

(2) Martinolich, A. J.; Neilson, J. R. Toward Reaction-by-Design: Achieving Kinetic Control of Solid State Chemistry with Metathesis. *Chem. Mater.* **2017**, *29*, 479–489.

(3) Parija, A.; Waetzig, G. R.; Andrews, J. L.; Banerjee, S. Traversing Energy Landscapes Away from Equilibrium: Strategies for Accessing and Utilizing Metastable Phase Space. *J. Phys. Chem. C* **2018**, *122*, 25709–25728.

(4) Sun, W.; Dacek, S. T.; Ong, S. P.; Hautier, G.; Jain, A.; Richards, W. D.; Gamst, A. C.; Persson, K. A.; Ceder, G. The Thermodynamic Scale of Inorganic Crystalline Metastability. *Sci. Adv.* **2016**, *2*, e1600225.

(5) Hudak, B. M.; Depner, S. W.; Waetzig, G. R.; Talapatra, A.; Arroyave, R.; Banerjee, S.; Guiton, B. S. Real-Time Atomistic Observation of Structural Phase Transformations in Individual Hafnia Nanorods. *Nat. Commun.* **2017**, *8*, 15316.

(6) Navrotsky, A.; Mazeina, L.; Majzlan, J. Size-Driven Structural and Thermodynamic Complexity in Iron Oxides. *Science.* **2008**, *319*, 1635.

(7) De Jesus, L. R.; Andrews, J. L.; Parija, A.; Banerjee, S. Defining Diffusion Pathways in Intercalation Cathode Materials: Some Lessons from V_2O_5 on Directing Cation Traffic. *ACS Energy Lett.* **2018**, *3*, 915–931.

(8) Powell, A. E.; Hodges, J. M.; Schaak, R. E. Preserving Both Anion and Cation Sublattice Features during a Nanocrystal Cation-Exchange Reaction: Synthesis of Metastable Wurtzite-Type CoS and MnS. *J. Am. Chem. Soc.* **2016**, *138*, 471–474.

(9) Schaak, R. E.; Mallouk, T. E. Perovskites by Design: A Toolbox of Solid-State Reactions. *Chem. Mater.* **2002**, *14*, 1455–1471.

(10) Bianco, E.; Butler, S.; Jiang, S.; Restrepo, O. D.; Windl, W.; Goldberger, J. E. Stability

and Exfoliation of Germanane: A Germanium Graphane Analogue. *ACS Nano* **2013**, *7*, 4414–4421.

(11) Cultrara, N. D.; Wang, Y.; Arguilla, M. Q.; Scudder, M. R.; Jiang, S.; Windl, W.; Bobev, S.; Goldberger, J. E. Synthesis of 1T, 2H, and 6R Germanane Polytypes. *Chem. Mater.* **2018**, *30*, 1335–1343.

(12) DeVries, R. C. Synthesis of Diamond Under Metastable Conditions. *Ann. Rev. Mater. Sci.* **1987**, *17*, 161.

(13) Angus, J. C.; Hayman, C. C. Low-Pressure, Metastable Growth of Diamond and "Diamondlike" Phases. *Annu. Rev. Mater. Sci.* **1988**, *241*, 913–921.

(14) Garvie, R. C. The Occurrence of Metastable Tetragonal Zirconia as a Crystallite Size Effect. *J. Phys. Chem.* **1965**, *69*, 1238–1243.

(15) Waetzig, G. R.; Depner, S. W.; Asayesh-Ardakani, H.; Cultrara, N. D.; Shahbazian-Yassar, R.; Banerjee, S. Stabilizing Metastable Tetragonal HfO_2 Using a Non-Hydrolytic Solution-Phase Route: Ligand Exchange as a Means of Controlling Particle Size. *Chem. Sci.* **2016**, *7*, 4930–4939.

(16) Garvie, C. The Occurrence of Metastable Tetragonal Zirconia as a Crystallite Size Effect. *J. Phys. Chem.* **1965**, *69*, 1238–1243.

(17) Chevalier, J.; Gremillard, L.; Clarke, D. R.; Clarke, D. R. The Tetragonal-Monoclinic Transformation in Zirconia: Lessons Learned and Future Trends. *J. Am. Ceram. Soc.* **2009**, *92*, 1901–1920.

(18) Tang, J.; Zhang, F.; Zoogman, P.; Fabbri, J.; Chan, S.-W.; Zhu, Y.; Brus, L. E.; Steigerwald, M. L. Martensitic Phase Transformation of Isolated HfO_2, ZrO_2, and $Hf_xZr_{1-x}O_2$ ($0 < x < 1$) Nanocrystals. *Adv. Funct. Mater.* **2005**, *15*, 1595–1602.

(19) Joo, J.; Yu, T.; Kim, Y. W.; Park, H. M.; Wu, F.; Zhang, J. Z.; Hyeon, T. Multigram Scale Synthesis and Characterization of Monodisperse Tetragonal Zirconia Nanocrystals. *J. Am. Chem. Soc.* **2003**, *125*, 6553–6557.

(20) Tang, J.; Fabbri, J.; Robinson, R. D.; Zhu, Y.; Herman, I. P.; Steigerwald, M. L.; Brus, L. E. Solid-Solution Nanoparticles: Use of a Nonhydrolytic Sol−Gel Synthesis To Prepare HfO_2 and $Hf_x Zr_{1-x} O_2$ Nanocrystals. *Chem. Mater.* **2004**, *16*, 1336–1342.

(21) Shin, D.; Arróyave, R.; Liu, Z. K. Thermodynamic Modeling of the Hf-Si-O System. *Calphad Comput. Coupling Phase Diagrams Thermochem.* **2006**, *30*, 375–386.

(22) Wang, J.; Li, H. P.; Stevens, R. Review Hafnia and Hafnia-Toughened Ceramics. *J. Mater. Sci.* **1992**, *27*, 5397–5430.

(23) Luo, X.; Zhou, W.; Ushakov, S. V; Navrotsky, A.; Demkov, A. A. Monoclinic to Tetragonal Transformations in Hafnia and Zirconia: A Combined Calorimetric and Density Functional Study. *Phys. Rev. B - Condens. Matter Mater. Phys.* **2009**, *80*, 134119.

(24) Zhao, X.; Vanderbilt, D. First-Principles Study of Structural, Vibrational, and Lattice Dielectric Properties of Hafnium Oxide. *Phys. Rev. B* **2002**, *65*, 233106.

(25) Depner, S. W.; Cultrara, N. D.; Farley, K. E.; Qin, Y.; Banerjee, S. Ferroelastic Domain Organization and Precursor Control of Size in Solution-Grown Hafnium Dioxide Nanorods. *ACS Nano* **2014**, *8*, 4678–4688.

(26) Zhou, B.; Shi, H.; Zhang, X. D.; Su, Q.; Jiang, Z. Y. The Simulated Vibrational Spectra of HfO_2 Polymorphs. *J. Phys. D. Appl. Phys.* **2014**, *47*, 115502.

(27) Böscke, T. S.; Müller, J.; Bräuhaus, D.; Schröder, U.; Böttger, U. Ferroelectricity in Hafnium Oxide Thin Films. *Appl. Phys. Lett.* **2011**, *99*, 102903.

(28) Batra, R.; Huan, T. D.; Rossetti, G. A.; Ramprasad, R. Dopants Promoting Ferroelectricity

in Hafnia: Insights From A Comprehensive Chemical Space Exploration. *Chem. Mater.* **2017**, *29*, 9102–9109.

(29) Perevalov, T. V.; Gritsenko, V. A.; Erenburg, S. B.; Badalyan, A. M.; Wong, H.; Kim, C. W. Atomic and Electronic Structure of Amorphous and Crystalline Hafnium Oxide: X-Ray Photoelectron Spectroscopy and Density Functional Calculations. *J. Appl. Phys.* **2007**, *101*, 053704.

(30) He, W.; Zhang, L.; Chan, D. S. H.; Cho, B. J. Cubic-Structured HfO_2 with Optimized Doping of Lanthanum for Higher Dielectric Constant. *IEEE Electron Device Lett.* **2009**, *30*, 623–625.

(31) Turquat, C.; Leroux, C.; Roubin, M.; Nihoul, G. Vanadium-Doped Elaboration and Structural Hafnia: Elaboration and Structural Characterization. *Solid State Sci* **1999**, *1*, 3–13.

(32) Turquat, C. Structural Investigation of Temperature-Induced Phase Transitions in HfV_2O_7. *Eur. Phys. J. Appl. Phys.* **2000**, *10*, 15–27.

(33) Evans, J. S. O. Negative Thermal Expansion Materials. *J. Chem Soc., Dalt. Trans.*, **1999**, 3317–3326.

(34) Buchanan, R. C.; Wolter, G. W. Properties of Hot-Pressed Zirconium Pyrovanadate Ceramics. *J. Electrochem. Soc.* **1983**, *130*, 1905.

(35) Korthuis, V.; Khosrovani, N.; Sleight, A. W.; Roberts, N.; Dupree, R.; Warren, W. W. Negative Thermal Expansion and Phase Transitions in the $ZrV_{2-x}P_xO_7$ Series. *Chem. Mater.* **1995**, *7*, 412–417.

(36) Fleer, N. A.; Pelcher, K. E.; Zou, J.; Nieto, K.; Douglas, L. D.; Sellers, D. G.; Banerjee, S. Hybrid Nanocomposite Films Comprising Dispersed VO_2 Nanocrystals: A Scalable

Aqueous-Phase Route to Thermochromic Fenestration. *ACS Appl. Mater. Interfaces* **2017**, *9*, 38887–38900.

(37) Fleer, N. A.; Pelcher, K. E.; Nieto, K.; Braham, E. J.; Zou, J.; Horrocks, G. A.; Naoi, Y.; Depner, S. W.; Schultz, B. J.; Amano, J.; et al. Elucidating the Crystallite Size Dependence of the Thermochromic Properties of Nanocomposite VO_2 Thin Films. *ACS Omega* **2018**, *3*, 14280–14293.

(38) Alivio, T. E. G.; Sellers, D. G.; Asayesh-Ardakani, H.; Braham, E. J.; Horrocks, G. A.; Pelcher, K. E.; Villareal, R.; Zuin, L.; Shamberger, P. J.; Arroyave, R.; et al. Postsynthetic Route for Modifying the Metal — Insulator Transition of VO_2 by Interstitial Dopant Incorporation. *Chem. Mater* **2017**, *29*, 5401–5412.

(39) Li, X.; Cai, W.; Colombo, L.; Ruoff, R. S. Evolution of Graphene Growth on Ni and Cu by Carbon Isotope Labeling. *Nano Lett.* **2009**, *9*, 4268–4272.

(40) Zhu, J.; Zhou, Y.; Wang, B.; Zheng, J.; Ji, S.; Yao, H.; Luo, H.; Jin, P. Vanadium Dioxide Nanoparticle-Based Thermochromic Smart Coating: High Luminous Transmittance, Excellent Solar Regulation Efficiency, and Near Room Temperature Phase Transition. *ACS Appl. Mater. Interfaces* **2015**, *7*, 27796–27803.

(41) Li, Y.; Ji, S.; Gao, Y.; Luo, H.; Kanehira, M. Core-Shell VO_2@TiO_2 Nanorods That Combine Thermochromic and Photocatalytic Properties for Application as Energy-Saving Smart Coatings. *Sci. Rep.* **2013**, *3*, 1370.

(42) Pelcher, K. E.; Crawley, M. R.; Banerjee, S. Silica-Shell Encapsulation and Adhesion of VO_2 Nanowires to Glass Substrates: Integrating Solution-Derived VO_2 Nanowires within Thermally Responsive Coatings. *Mater. Res. Express* **2014**, *1*, 035014.

(43) Rai, D.; Kitamura, A.; Rosso, K. M.; Sasaki, T.; Kobayashi, T. Issues Concerning the

Determination of Solubility Products of Sparingly Soluble Crystalline Solids: Solubility of HfO2(Cr). *Radiochim. Acta* **2016**, *104*, 583–592.

(44) Post, K.; Robins, R. G. Thermodynamic Diagrams for the Vanadium-Water System at 298·15K. *Electrochim. Acta* **1976**, *21*, 401–405.

(45) Chen, B. R.; Sun, W.; Kitchaev, D. A.; Mangum, J. S.; Thampy, V.; Garten, L. M.; Ginley, D. S.; Gorman, B. P.; Stone, K. H.; Ceder, G.; et al. Understanding Crystallization Pathways Leading to Manganese Oxide Polymorph Formation. *Nat. Commun.* **2018**, *9*, 2553.

(46) Sun, W.; Kitchaev, D. A.; Kramer, D.; Ceder, G. Non-Equilibrium Crystallization Pathways of Manganese Oxides in Aqueous Solution. *Nat. Commun.* **2019**, *10*, 1–9.

(47) Ushakov, S. V.; Brown, C. E.; Navrotsky, A. Effect of La and y on Crystallization Temperatures of Hafnia and Zirconia. *J. Mater. Res.* **2004**, *19*, 693–696.

(48) Hisashige, T.; Yamaguchi, T.; Tsuji, T.; Yamamura, Y. Phase Transition of $Zr_{1-x}Hf_xV_2O_7$ Solid Solutions Having Negative Thermal Expansion. *J. Ceram. Soc. Japan* **2006**, *114*, 607–611.

(49) Braham, E. J.; Andrews, J. L.; Alivio, T. E. G.; Fleer, N. A.; Banerjee, S. Stabilization of a Metastable Tunnel-Structured Orthorhombic Phase of VO_2 upon Iridium Doping. *Phys. Status Solidi Appl. Mater. Sci.* **2018**, *215*, 1–9.

(50) Marley, P. M.; Horrocks, G. A.; Pelcher, K. E.; Banerjee, S. Transformers: The Changing Phases of Low-Dimensional Vanadium Oxide Bronzes. *Chem. Commun.* **2015**, *51*, 5181–5198.

CHAPTER V

A FACILE SYNTHETIC ROUTE TO HFV_2O_7 AND EVALUATION OF ITS NEGATIVE THERMAL EXPANSION PROPERTIES

V.1 Introduction

Thermal expansion gradients resulting in uneven expansion in materials causes a substantial amount of damage in infrastructure and requires installation of expansion joints to accommodate the resulting stress and prevent catastrophic failure of materials.[1–3] One such place that these joints are most readily observed are in cement and railways; however, other materials that experience high temperature operating conditions, such as glassware or electronics, also experience a similar detrimental effect.[1–3] Many NTE materials, such as those related to the $NaZr_2(PO_4)_3$ family of materials, exhibit anisotropic NTE behavior.[2,4–9] This results in undesirable microcracking that damages the NTE material under repeated thermal cycling.[1–3] HfV_2O_7 (C); however, alleviates this drawback in that its NTE behavior is isotropic and thus negates any orientation requirements in NTE composite materials and prevents microcracking.[1–3] Many synthetic procedures to produce the MxV_2O_7 family of materials lack scalability or rely on more complicated, costly procedures and undesirable organic solvents such as hexanes.[1,3,10]

Here, we report a synthesis involving a completely solid—solid reaction with characterization of the NTE behavior. This method relies on mechanical grinding of HfO_2 with VO_2 in the appropriate molar ratio of 1:2 (HfO_2:VO_2).

V.2 Experimental

A typical mechanical synthetic route is accomplished by taking VO_2 (M1) nanocrystals and grinding them with amorphous HfO_2. VO_2 (M1) nanocrystals were synthesized by precipitating $VO(OH)_2$ from a solution of deionized, nanopure water (ρ=18.2 MΩ·cm, Barnstead Water Purification System) and ammonium metavanadate that was reduced with a 10% hydrazine solution in water at 80°C.[11–14] The precipitate is then collected *via* centrifugation and is then annealed in a Teflon cup placed inside a hydrothermal autoclave at 210°C for 24 hours to produce VO_2 (M1) nanocrystals. This material was then collected by centrifugation and subsequently washed and centrifuged with acetone a total of three times to purify the solid. The solid was allowed to dry and used without further modification.

Amorphous HfO_2 was synthesized by placing 400 µL $Hf(O^tBu)_4$ in 80 mL water and then collecting the white amorphous HfO_2 precipitate through centrifugation. This precipitate was washed twice with acetone followed by collection *via* centrifugation each time.

This amorphous HfO_2 was ground with VO_2 nanocrystals in a mortar and pestle in a molar ratio of 1:2 HfO_2:VO_2 in accordance with **Equation V. 1** shown below:

$$4VO_2\,(s) + 2HfO_2\,(s) + O_2\,(g) \xrightarrow{\Delta} 2HfV_2O_7\,(s) \qquad \textbf{(V. 1)}$$

This mixture was then ball milled in a 100 mg quantity using three polymethacrylate milling beads to ensure a homogenous mixture. This mixture is the annealed at 600°C under static air.

This procedure is shown schematically in **Figure V. 1**.

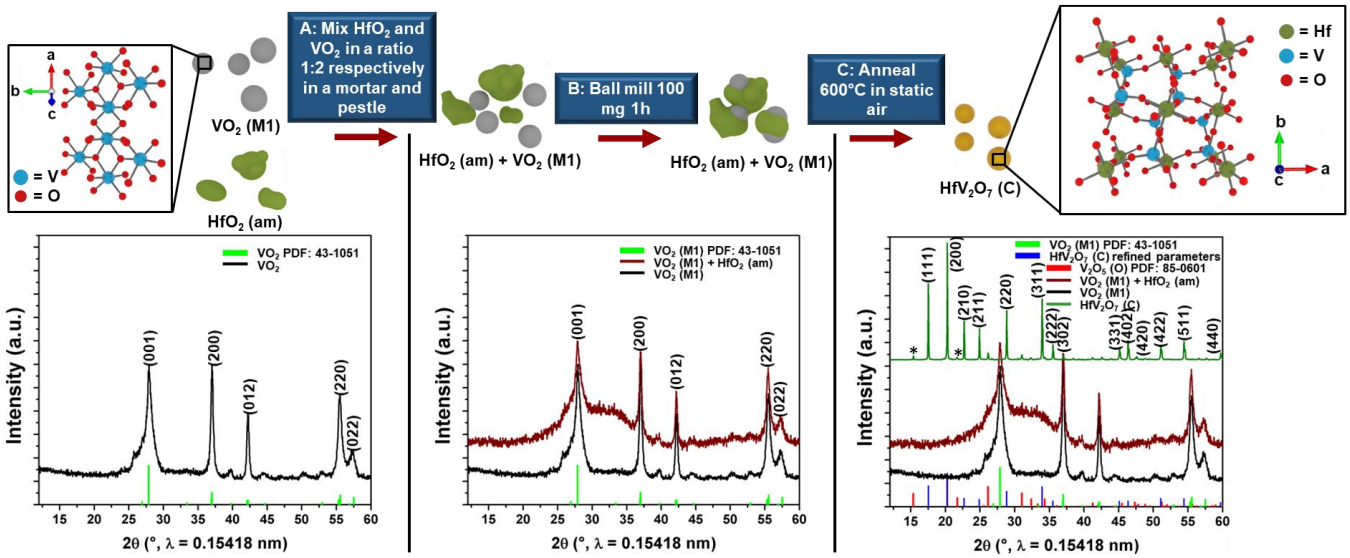

Figure V. 1 Mechanical synthesis of HfV_2O_7 (C). A) Mortar and pestle grinding of amorphous HfO_2 and VO_2 (M1) nanocrystals (shown in XRD pattern) at a molar ratio of 1:2 (HfO_2:VO_2). B) Ball milling the mixture. The milled material is shown in the corresponding pattern under step B. The amorphous scattering background of amorphous HfO_2 is clearly visible. C) The milled material was annealed in static air under ambient pressure at 600°C for 25 min. The final product, HfV_2O_7 (C), needs no further purification once removed from heat and shows excellent purity with minimal V_2O_5 (O) impurities marked with an (*) in the corresponding XRD pattern.

V.3 Results and Discussion

Figure V. 2 shows a Rietveld refinement of an observed cubic HfV_2O_7 pattern. This pattern refines to HfV_2O_7 (C) with a ($Pa\bar{3}$) space group which is common for this material.[15] Thermal XRD in **Figure V. 3** demonstrates the expected NTE behavior from this family of materials.[1–3,7–10] This plot shows intensity (a.u.) in the Z direction to better observe how 2θ positions of a representative (440) reflection and how it shifts with temperature. The sample was held at 600°C for 4 hours to facilitate drying. NTE materials tend to be very easily hydrated in ambient conditions due to humidity diffusing into vacant spaces in the lattice which are essential for lattice contraction.[2,16] It can be observed in the thermal modulation plot of XRD patterns recorded at increasing and then subsequently decreasing temperatures (taken at 50°C intervals)

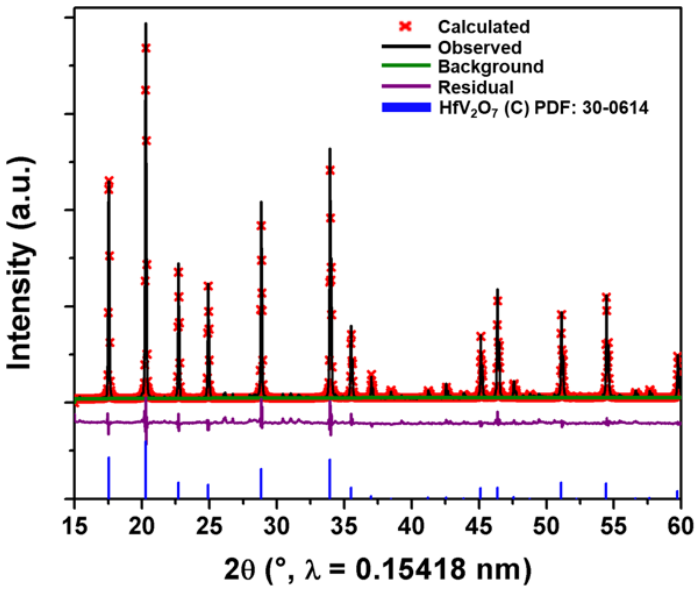

Figure V. 2 Observed XRD pattern (black line) on the calculated Rietveld refinement (red crosses). The residual curve is purple and the blue bars show the known reflections for HfV_2O_7 (C) with a ($Pa\bar{3}$) space group. The pattern matches to that of HfV_2O_7 (C).

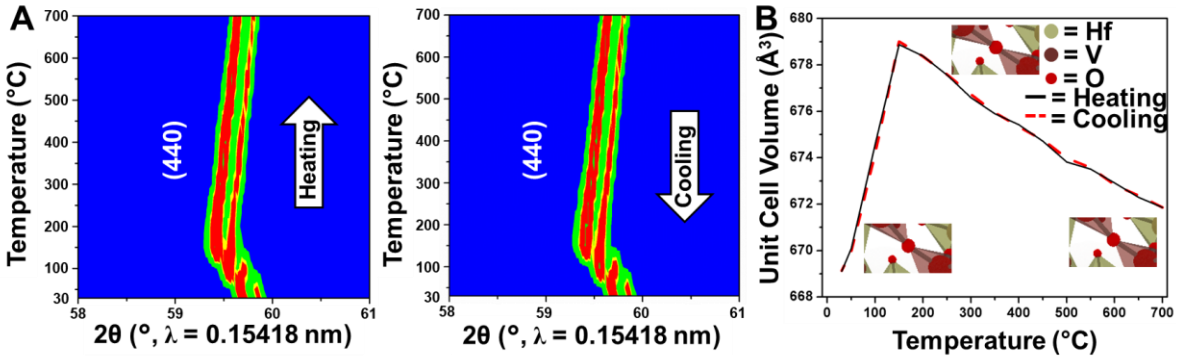

Figure V. 3 A) *In situ* thermal XRD intensity (a.u. in the Z direction) modulation plot of HfV_2O_7 (C) showing a representative reflection (440) shifting to lower 2θ as the lattice expands with temperature increase following a subsequent shift to a higher 2θ with lattice compression. The cooling phase shows another lattice expansion followed by contraction. B) shows unit cell volume and its relation to temperature as well as illustrations of bond angles of the VO_3—O—VO_3 oxygen bridge.

that the reflections exhibit a rapid, downward shift in 2θ followed by a gradual increase in 2θ.

This is especially obvious in the expanded view of the (440 reflection that was selected as an

example. The decrease in 2θ is characteristic of an expansion in d-spacing and is caused in part by the straightening of the central VO_3—O—VO_3 bond at rising temperatures prior to transverse, volume reducing oscillations which results in a subsequent, gradual increase in 2θ as d-spacing is reduced by transverse vibrations of the oxygen bridge.[1–3,7–10,17,18] The lineshape of the plotted unit cell volume *vs* temperature corroborates this behavior in Figure V. 3B. Figure V. 3B also shows illustrations of the central VO_3—O—VO_3 bond and how these two central tetrahedra

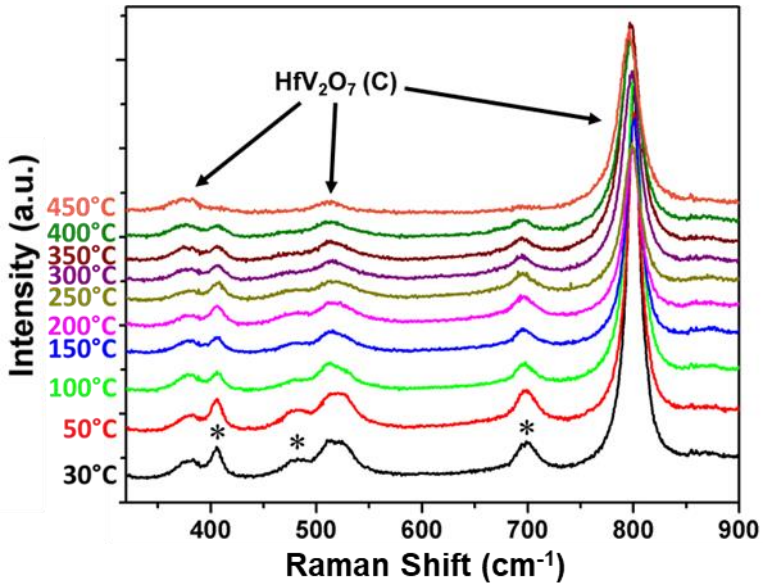

Figure V. 4 Raman spectroscopy of HfV_2O_7 (C) at increasing temperatures. Modes marked with an (*) are attributed to V_2O_5.

vibrate transversely at key stages of heating and is similar to other classes of NTE materials with a P—O—P bond, such as the $ZrV_xP_{2-x}O_7$ system, where the oxygen bridge angle switches between 160° and 180° at room temperature and ca. >100°C respectively.[1–3,5,10,17–19]

Figure V. 4 shows successive Raman spectra of a HfV_2O_7 (C) sample at increasing temperatures. The spectra were recorded after holding the HfV_2O_7 (C) material at a temperature of 450°C for 4 h under circulating nitrogen to ensure adequate drying. The temperature was then

lowered to 30°C for 10 min to allow for equilibration and a spectra was obtained. The same was done at 50°C and then at 50°C intervals up to 450°C. The modes at 377 and 798 cm^{-1} are understood to be partly contributed to internal modes of VO_4.[20,21] The modes at 405, 482, and 698 cm^{-1} are due to the presence of V_2O_5 (O) which is generally present in small quantities after synthesis as can be seen in the XRD patterns shown previously.[21,22] It can be noted that the V_2O_5 (O) peaks are greatly reduced or completely nonexistent at higher temperatures as the V_2O_5 (O) metal to insulator transition occurs at 257 ± 5°C and results in higher reflectivity and increased carrier density which reduces the Raman sensitivity for the material due to lower laser penetration depth.[22–27] It is also noteworthy that the HfV_2O_7 (C) peaks shift slightly to lower frequencies, by about 5.0 ± 0.9 cm^{-1}, as is consistent with V—O bond stretching related to lattice vibrations responsible for NTE behavior.[1,2,21]

V.4 Conclusion

In conclusion, we have demonstrated here a synthetic method for the synthesis of HfV_2O_7 (C) that avoids traditional synthetic procedures that rely on high pressure and organic solvents. The method presented here relies mostly on water or ethanol and may be performed in an entirely solid, mechanical procedure. This presents an opportunity for a scalable, reliable synthesis to produce an isotropic NTE material that is highly industrially relevant as an additive to any material exhibiting undesirable thermal expansion.[1–6] It has been shown that this material displays characteristic lattice expansion and contraction as expected in HfV_2O_7 (C) and related materials.[1–9] The nature of the NTE behavior of HfV_2O_7 (C) was also examined using XRD and Raman showing that these synthetic procedures do indeed produce high quality HfV_2O_7 (C) and

could lead to deployment of such materials to produce zero thermal expansion composite materials.

V.5 References

(1) Turquat, C. Structural Investigation of Temperature-Induced Phase Transitions in HfV_2O_7. *Eur. Phys. J. Appl. Phys.* **2000**, *10*, 15–27.

(2) Evans, J. S. O. Negative Thermal Expansion Materials. *J. Chem Soc., Dalt. Trans.*, **1999**, 3317–3326.

(3) Korthuis, V.; Khosrovani, N.; Sleight, A. W.; Roberts, N.; Dupree, R.; Warren, W. W. Negative Thermal Expansion and Phase Transitions in the $ZrV_{2-x}P_xO_7$ Series. *Chem. Mater.* **1995**, *7*, 412–417.

(4) Lightfoot, P.; Woodcock, D. A.; Jorgensen, J. D.; Short, S. Low Thermal Expansion Materials: A Comparison of the Structural Behaviour of $La_{0.33}Ti_2(PO_2)_3$, $Sr_{0.5}Ti_2(PO_4)_3$ and $NaTi_2(PO_4)_3$. *Int. J. Inorg. Mater.* **1999**, *1*, 53–60.

(5) Barrera, G. D.; Bruno, J. A. O.; Barron, T. H. K.; Allan, N. L. Negative Thermal Expansion. *J. Phys. Condens. Matter* **2005**, *17*, R217–R252.

(6) Catti, M.; Comotti, A.; Di Blas, S. High-Temperature Lithium Mobility in α-$LiZr_2(PO_4)_3$ NASICON by Neutron Diffraction. *Chem. Mater.* **2003**, *15*, 1628–1632.

(7) Khosrevani, N.; Korthuis, V.; Sleight, A. W.; Vogt, T. Unusual 180° P-O-P Bond Angles in ZrP_2O_7. *Inorganic Chemistry*. 1996, *35*, 485-489.

(8) Khosrovani, N.; Sleight, A. W.; Vogt, T. Structure of ZrV_2O_7 from -263 to 470°C. *Journal of Solid State Chemistry*. 1997, *132*, 355–360.

(9) Evans, J. S. O.; Hanson, J. C.; Sleight, A. W. Room-Temperature Superstructure of

ZrV_2O_7. *Acta Crystallogr. Sect. B Struct. Sci.* **1998**, *54*, 705–713.

(10) Hisashige, T.; Yamaguchi, T.; Tsuji, T.; Yamamura, Y. Phase Transition of $Zr_{1-x}Hf_xV_2O_7$ Solid Solutions Having Negative Thermal Expansion. *J. Ceram. Soc. Japan* **2006**, *114*, 607–611.

(11) Fleer, N. A.; Pelcher, K. E.; Nieto, K.; Braham, E. J.; Zou, J.; Horrocks, G. A.; Naoi, Y.; Depner, S. W.; Schultz, B. J.; Amano, J.; et al. Elucidating the Crystallite Size Dependence of the Thermochromic Properties of Nanocomposite VO_2 Thin Films. *ACS Omega* **2018**, *3*, 14280–14293.

(12) Fleer, N. A.; Pelcher, K. E.; Zou, J.; Nieto, K.; Douglas, L. D.; Sellers, D. G.; Banerjee, S. Hybrid Nanocomposite Films Comprising Dispersed VO_2 Nanocrystals: A Scalable Aqueous-Phase Route to Thermochromic Fenestration. *ACS Appl. Mater. Interfaces* **2017**, *9*, 38887–38900.

(13) Li, W.; Ji, S.; Qian, K.; Jin, P. Preparation and Characterization of VO_2-$BaSO_4$ Composite Films with Enhanced Optical Properties in Thermochromic Field. *Ceram. Int.* **2015**, *41*, 5049–5056.

(14) Zhu, J.; Zhou, Y.; Wang, B.; Zheng, J.; Ji, S.; Yao, H.; Luo, H.; Jin, P. Vanadium Dioxide Nanoparticle-Based Thermochromic Smart Coating: High Luminous Transmittance, Excellent Solar Regulation Efficiency, and Near Room Temperature Phase Transition. *ACS Appl. Mater. Interfaces* **2015**, *7*, 27796–27803.

(15) Mittal, R.; Chaplot, S. L. Lattice Dynamical Calculation of Negative Thermal Expansion in ZrV_2O_7 and HfV_2O_7. *Phys. Rev. B* **2008**, *78*, 174303.

(16) Banek, N. A.; Baiz, H. I.; Latigo, A.; Lind, C. Autohydration of Nanosized Cubic Zirconium Tungstate. *J. Am. Chem. Soc.* **2010**, *132*, 8278–8279.

(17) Liu, X.; Le Flem, M.; Béchade, J. L.; Onimus, F.; Cozzika, T.; Monnet, I. XRD Investigation of Ion Irradiated $Ti_3Si_{0.90}Al_{0.10}C_2$. *Nucl. Instruments Methods Phys. Res. Sect. B Beam Interact. with Mater. Atoms* **2010**, *268*, 506–512.

(18) Sawabe, T.; Akiyoshi, M.; Yoshida, K.; Yano, T. Estimation of Neutron-Irradiation-Induced Defect in 3C-SiC from Change in XRD Peak Shift and DFT Study. *J. Nucl. Mater.* **2011**, *417*, 430–434.

(19) Ibberson, R. M.; Kameswari, U.; Hanson, P. A.; Evans, J. S. O.; Duan, N.; Sleight, A. W. Symmetric Stretching Vibrations of Two-Coordinate Oxygen Bridges as a Cause for Negative Thermal Expansion in $ZrV_xP_{2-x}O_7$AndAW_2O_8(A=Zr, Hf) at High Temperature. *J. Am. Chem. Soc.* **2002**, *122*, 8694–8699.

(20) Hemamala, U. L. C.; El-Ghussein, F.; Goedken, A. M.; Chen, B.; Leroux, C.; Kruger, M. B. High-Pressure x-Ray Diffraction and Raman Spectroscopy of HfV_2O_7. *Phys. Rev. B - Condens. Matter Mater. Phys.* **2004**, *70*, 1–4.

(21) Sakuntala, T.; Arora, A. K.; Sivasubramanian, V.; Rao, R.; Kalavathi, S.; Deb, S. K. Pressure-Induced Amorphization and Decomposition in ZrV_2O_7: A Raman Spectroscopic Study. *Phys. Rev. B - Condens. Matter Mater. Phys.* **2007**, *75*, 1–6.

(22) Horrocks, G. a.; Likely, M. F.; Velazquez, J. M.; Banerjee, S. Finite Size Effects on the Structural Progression Induced by Lithiation of V_2O_5: A Combined Diffraction and Raman Spectroscopy Study. *J. Mater. Chem. A* **2013**, *1*, 15265.

(23) Pérez-Pacheco, A.; Acosta-Najarro, D. R.; Castañeda-Guzmán, R.; Cruz-Manjarrez, H.; Rodriguez-Fernandez, L.; Pineda-Santamaría, J. C.; Aguilar-Franco, M. Evidence of the Semiconductor-Metal Transition in V_2O_5 Thin Films by the Pulsed Laser Photoacoustic Method. *J. Appl. Phys.* **2013**, *113*, 184307.

(24) Aita, C. R.; Liu, Y. L.; Kao, M. L.; Hansen, S. D. Optical Behavior of Sputter-Deposited Vanadium Pentoxide. *J. Appl. Phys.* **1986**, *60*, 749–753.

(25) Alivio, T. E. G.; Sellers, D. G.; Asayesh-Ardakani, H.; Braham, E. J.; Horrocks, G. A.; Pelcher, K. E.; Villareal, R.; Zuin, L.; Shamberger, P. J.; Arroyave, R.; et al. Postsynthetic Route for Modifying the Metal — Insulator Transition of VO_2 by Interstitial Dopant Incorporation. *Chem. Mater* **2017**, *29*, 5401–5412.

(26) Whittaker, L.; Wu, T. L.; Stabile, A.; Sambandamurthy, G.; Banerjee, S. Single-Nanowire Raman Microprobe Studies of Doping-, Temperature-, and Voltage-Induced Metal-Insulator Transitions of $W_xV_{1-x}O_2$ Nanowires. *ACS Nano* **2011**, *5*, 8861–8867.

(27) Jones, A. C.; Berweger, S.; Wei, J.; Cobden, D.; Raschke, M. B. Nano-Optical Investigations of the Metal-Insulator Phase Behavior of Individual VO_2 Microcrystals. *Nano Lett.* **2010**, *10*, 1574–1581.

CHAPTER VI

DISSERTATION SUMMARY AND OUTLOOK

VI.1 Conclusion

This dissertation is focused on the theme of establishing control of free energy landscapes of early transition metal oxides with a view towards stabilizing metastable polymorphs, modulating the transformation characteristics of solid-solid transitions, and utilizing such polymorphs and transitions for functional applications in thermochromics and high-k dielectrics. The first part of the dissertation (Chapters II and III) focused on devising routes to utilize the change in optical conductivity of a canonical Martensitic transforming material VO_2. The reversible insulator to metal phase transition of VO_2 occurs in relative proximity to room temperature, which makes it useful for thermochromic applications such as dynamically switchable glazing.[1–3] Chapter IV focus on a similar Martensitic transforming material HfO_2 albeit where such transitions are manifested at much higher temperatures. The large bandgap and soft phonon modes of this material make it an excellent candidate as an alternative to amorphous silica as a gate dielectric for field-effect transistors. However, the most desirable properties of the materials are only achievable for the metastable phases. The tetragonal and cubic polymorphs of HfO_2 have dielectric constants of ca. 70 and ca. 20—30, respectively.[4–7] As such, stabilization of these metastable polymorphs under ambient conditions has emerged as an urgent imperative. Finally, the high-temperature reaction of these two materials yields a Negative Thermal Expansion (NTE) material, HfV_2O_7, which can potentially be used as an additive to access net-zero thermal expansion materials. The inclusion of NTE materials within composites reduces

stress engendered by thermal expansion gradients, thereby mitigating a primary means of crack formation and catastrophic failure.[8–10]

Chapter II demonstrates how the size of VO_2 (M1) nanoparticles and wires impacts the Mie scattering of nanocomposite films in a thermochromic fenestration application designed to reduce the energy consumption of buildings.[2] Visible light scattering in window films produces aesthetically unappealing haze and increases the need for daylighting. However, this scattering is size dependent as Mie scattering increases as the particle size matches that or exceeds the wavelength of light with which it is interacting. This chapter examined four sizes of VO_2 (M1) nanoparticles and wires, 210±70 nm width and 4.0±3.0 μm length, 180±70 nm with and 1.6±0.9 μm length, 110±90 nm width and 211±187 nm length, and 44±30 nm quasi spherical particles, all coated with a SiO_2 shells, to determine how particle size influences the proportion of transmitted visible light, referred to as T_{lum}, the quantity of near infrared (NIR) light transmitted, T_{NIR}, and the quantity of total solar energy transmitted, T_{Sol}.[11,12] The performance of these VO_2 (M1) nanocomposite films also relies heavily on a Localized-Surface Plasmon Resonance (LSPR) which arises upon closing of the VO_2 (M1) band gap and transitioning from an insulator to metal phase. The larger wires experience more internal scattering and thus show a much broader scattering profile that extends into the NIR region and minimizes the effectiveness of the LSPR. NIR modulation is initiated only beyond 1000 nm, thereby rendering the thermochromic films ineffective in modulating solar heat gain in the proximal NIR region and substantially degrading achievable performance metrics. The 44±30 nm particle nanocomposite films experience less internal scattering and the small particle size results in an early NIR modulation onset (in the range between 741 and 749 nm depending on solid loading), owing to the LSPR absorbing more light at shorter wavelengths, while not diminishing visible light transmittance

due to less internal scattering.[2] The scattering resulting from increased particle size is also observed in the smaller particles as higher particle loadings result in agglomeration and increased internal scattering, which is accompanied by a red-shift of the NIR modulation onset (Figure II. 5).

Chapter III further elaborates on this research by examining the influence of (a) dispersion and (b) refractive index matching of VO_2 nanocrystals to the surrounding polymeric medium on thermochromic performance metrics. As stated in the previous paragraph, agglomeration of small particles causes extensive internal scattering, red-shifts the onset of NIR modulation, and diminishes the effectiveness of the LSPR in modulating NIR absorbance. Improvements in dispersion quality to mitigate scattering were achieved by functionalization of the surfaces of VO_2@SiO_2 particles with a fluorocarbon silane (trimethoxy(1H,1H,2H,2H-perfluorooctyl)silane), which is further complexed with a fluorinated ionic surfactant (potassium perfluorooctanesulfonate). Surface functionalization and dispersion using the polar perfluorinated surfactant yields aqueous dispersions of the nanoparticles, which allow for casting of high-quality optical films. In these films, a blue-shift of the onset of the LSPR-driven modulation of NIR light is observed from ca. 920 to ca. 760 nm. This occurs due to a reduction in the aforementioned internal scattering resulting from agglomeration of small particles.[1,2]

Chapter IV examines another solid phase transition, but one that is highly relevant to the electronics industry. The high dielectric constant of HfO_2 makes it a potential replacement for SiO_2, which is reaching its limitations, as a gate dielectric in FETs. The metastable phases of HfO_2; however, have only been stabilized via size confinement, the addition of twin planes, and substantial doping with elements such as Ge and La We have shown that the high temperature cubic phase can be stabilized through the reduction of VO_2 (M1) and epitaxial relationship

between the resulting rhombohedral V_2O_3 and HfO_2 (C) at 650°C.[13,14] This metastable phase remains stable upon quenching to ambient conditions. This approach results in some interdiffusion of vanadium onto the hafnium lattice but HfO_2 (C) is stabilized at $<7.18 \pm 0.17$ at.% vanadium doping (as compared to 11.0 at.% reported in the literature).[15] Furthermore, phase-pure cubic HfO_2 is obtained sans any HfV_2O_7 contamination, which is common as the reaction between VO_2 and HfO_2 proceeds readily discussed in Chapter V. This transition takes place at the very low temperature of 560-675°C and ambient pressure as compared to the bulk transition temperature of 2600°C. Cubic HfO_2 remains stable at room temperature and is a potential gate dielectric given its order-of-magnitude increase dielectric constant as compared to SiO_2.

Chapters IV and V illustrated in detail how the epitaxial relationship outlined in Chapter IV to stabilize HfO_2 (C) can be leveraged to synthesize HfV_2O_7 (C) via a solid—solid reaction. As discussed previously, HfV_2O_7 is an NTE material that, as is the case for many $M_xV_2O_7$ materials, contracts isotropically when heated. This makes this material ideal for industrial applications as it does not experience the drawbacks of anisotropic materials, such as uneven contraction and micro cracking. Two distinctive synthetic routes have been developed for the preparation of HfV_2O_7: i) a core—shell disposition of precursors yields VO_2@HfO_2 core—shell nanocrystals, which are annealed to obtain HfV_2O_7 through interdiffusion (Chapter IV) and ii) a mechanochemical method wherein a stoichiometric mixture of VO_2:HfO_2 is ball milled and annealed as described in Chapter V. Both methods rely on annealing the reaction mixtures in ambient pressure under static air. NTE behavior has been defined in temperature-variant powder X-ray diffraction and Raman spectroscopy measurements, which display a contraction of refined lattice parameters and shifting of phonon modes to higher frequencies. Such materials can be

used as additives to other materials that undergo (more conventional) positive thermal expansion resulting in a net zero thermal expansion for nanocomposites.

As future work for cubic HfO_2, **Figure VI. 1** outlines the details of producing nanocomposite films of HfO_2 (C), (R), and (M) in order to examine the dielectric constants

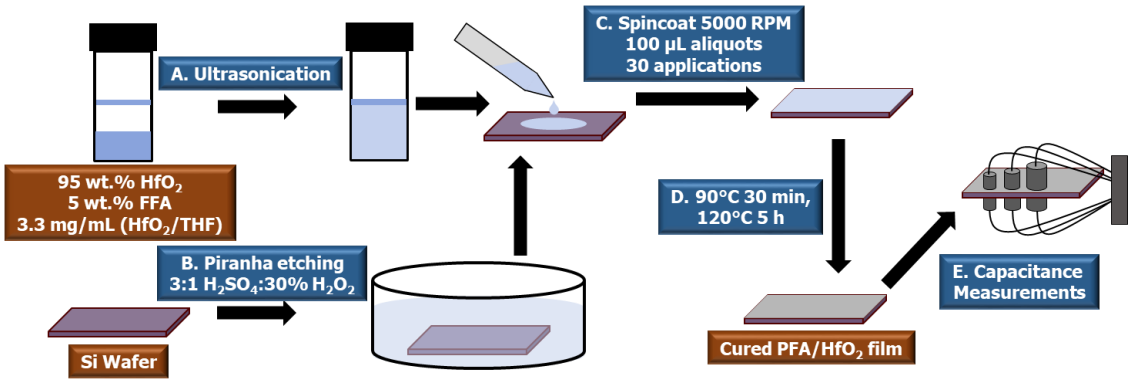

Figure VI. 1 Film casting scheme for PFA/HfO_2 films. A) Ultrasonication of FFA, HfO_2, and THF to produce a homogenous dispersion. B) Etching of Si wafer. C) Spin coating application of film material followed by D) gentle curing of films at 90°C for 30 min. to avoid monomer evaporation and high temperature annealing at 120°C for 5 h to rapidly crosslink FFA to PFA. E) Dielectric constant of films can be determined from capacitance measurements.[17]

accessible within flexible nanocomposite films.[5,6,16]

These values are confirmed to be ca. 18 for HfO_2 (M), predicted to be ca. 30 for HfO_2 (C), and ca. 70 for HfO_2 (R).[5,6,16] Films were cast by spincoating high loadings of HfO_2 solutions and a polymer host to avoid empty space in said films. Furfuryl alcohol (FFA) was utilized as the host material as it can be polymerized *in situ* to polyfurfuryl alcohol (PFA).[17] Tetrahydrofuran (THF) was used as a solvent. The solution was mixed as follows: 95 wt.% of the HfO_2/FFA mixture must be HfO_2, so a solution is mixed in a vial that is 95 wt.% HfO_2 and 5 wt.% FFA. This procedure used a 20 mL vial with 57 mg HfO_2 and 3 mg FFA. After the desired quantity of each material has been placed in a vial, the mixture is dispersed in a volume of THF equal to the

volume of THF – x where x = the volume of FFA used in the solution equal to 5 wt.% of the HfO_2/FFA mixture. The concentration of HfO_2/ mL THF + FFA is 3.3 mg/mL. This solution is sonicated vigorously for 2 h. This will be used as the casting solution. Si wafers (P doped) are cut at the size of 2 cm x 2 cm. These are etched using a piranha solution of the ratio 3:1 concentrated H_2SO_4:30% H_2O_2 for the duration of the casting solution's sonication.[3] The Si wafers were removed from the piranha solution and washed with nanopure water followed by 2-propanol and dried under flowing nitrogen. These wafers were then placed in a spin coater set at 5000 RPM. The casting solution was applied in 100 μL aliquots at 10 second intervals while the wafer was spinning for a total of 30 applications to produce films of 70 wt.% HfO_2. Prior to curing, each film is gently heated at 90°C for 30 min to both initiate curing and avoid evaporating the FFA monomer.[17] It is then crosslinked at 120°C for 5 h to complete the film.[17] This film has a 70% coverage of HfO_2 as confirmed by a custom built Secondary Ion Mass Spectrometry (SIMS) using a C_{60} beam shown in **Figure VI. 2**. The C_{60} source is used for impacts on the front side of the bulk target at an angle of incidence of 25° from normal. The secondary ions are emitted/detected in the reflection direction. The SIMS instrument is equipped with a 1.2 m linear time-of-flight (ToF) mass spectrometer and an electron emission microscope (EEM).[18,19] The EEM was used to detect secondary electrons for the ToF start signal. The secondary electrons being detected as a magnified electron image are used for "electron collimation" of the bombarded area. The data were acquired at the level of individual 50 keV C_{60} impacts with repetition rate of 1000 impacts/s. This event-by-event bombardment-detection mode allows for the selection of specific impacts.[20]

There are four types of projectile impacts using this method shown in **Figure VI. 3**: i) Impacts on the HfO_2 nanoparticles, when the emitted ions are small fragments of HfO and

$(HfO_2)_nO^-$ cluster ions, ii) Impacts on the surface of HfO_2 Nanoparticles coated by thin layers of the PFA resin, when the emitted from the emission volume (approximately semispherical of Ø 5nm) ions belong to nanoparticles and resin, iii) Impacts on the surface of PFA resin, only, iv) Impacts on the $NaSO_4$ salt impurities. The SIMS method with event-by-event bombardment-detection mode allows selection of individual mass spectra.

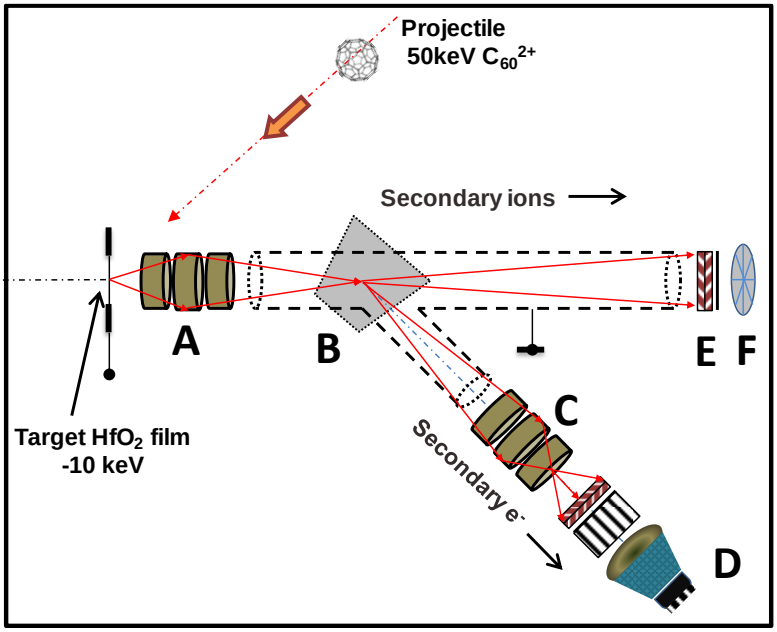

Figure VI. 2 Custom SIMS instrumentation. A) Objective lens for secondary ions and electrons B) Magnetic prism for redirection of electrons toward imaging electron optics in (C). C) Imaging electron optics. D) Position sensitive detector consisting of dual microchannel plate, phosphor screen, and complementary metal-oxide semiconductor camera E) Dual microchannel plate F) Anode detector.

Film thickness was determined by milling the surface of the film with a 14.5 keV Cs^+ beam with a current of 11 nA to create two 250×250 μm^2 craters on the film that extend down to the Si wafer. The depth of each crater was analyzed by Atomic Force Microscopy (AFM) to obtain a depth profile. The film thickness was determined to be 83.8±4.9 nm for the HfO_2 (R) films.

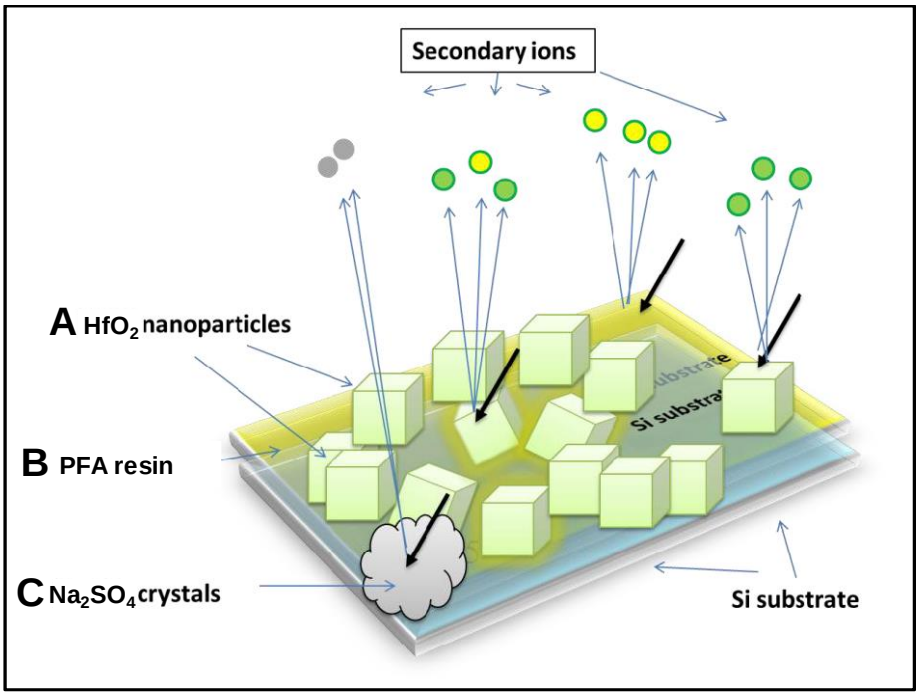

Figure V. 3 Impact types. A) Impact on HfO_2 nanoparticles or nanoparticles coated in PFA resin B) Impact on PFA resin without nanoparticles C) Impact on Na_2SO_4 salt impurities remaining from the surfactant.

A high nanoparticle loading such as this should be sufficient to determine the dielectric constant of the nanoparticle component of each film by measuring the capacitance of each nanocomposite film and backing out the dielectric constant of the HfO_2 component.[17] Such measurements are the focus on ongoing research.

VI.2 References

(1) Fleer, N. A.; Pelcher, K. E.; Zou, J.; Nieto, K.; Douglas, L. D.; Sellers, D. G.; Banerjee, S. Hybrid Nanocomposite Films Comprising Dispersed VO_2 Nanocrystals: A Scalable Aqueous-Phase Route to Thermochromic Fenestration. *ACS Appl. Mater. Interfaces* **2017**, *9*, 38887–38900.

(2) Fleer, N. A.; Pelcher, K. E.; Nieto, K.; Braham, E. J.; Zou, J.; Horrocks, G. A.; Naoi, Y.; Depner, S. W.; Schultz, B. J.; Amano, J.; Sellers, D. G.; Banerjee, S. Elucidating the

Crystallite Size Dependence of the Thermochromic Properties of Nanocomposite VO2 Thin Films. *ACS Omega* **2018**, *3*, 14280–14293.

(3) Pelcher, K. E.; Crawley, M. R.; Banerjee, S. Silica-Shell Encapsulation and Adhesion of VO_2 Nanowires to Glass Substrates: Integrating Solution-Derived VO_2 Nanowires within Thermally Responsive Coatings. *Mater. Res. Express* **2014**, *1*, 035014.

(4) Zhao, X.; Vanderbilt, D. First-Principles Study of Electronic and Dielectric Properties of ZrO_2 and HfO_2. *Mat. Res. Soc. Symp. Proc.* **2003**, *745*, 283–289.

(5) Zhao, X.; Vanderbilt, D. First-Principles Study of Structural, Vibrational, and Lattice Dielectric Properties of Hafnium Oxide. *Phys. Rev. B* **2002**, *65*, 233106.

(6) Hudak, B. M.; Depner, S. W.; Waetzig, G. R.; Talapatra, A.; Arroyave, R.; Banerjee, S.; Guiton, B. S. Real-Time Atomistic Observation of Structural Phase Transformations in Individual Hafnia Nanorods. *Nat. Commun.* **2017**, *8*, 15316.

(7) Waetzig, G. R.; Depner, S. W.; Asayesh-Ardakani, H.; Cultrara, N. D.; Shahbazian-Yassar, R.; Banerjee, S. Stabilizing Metastable Tetragonal HfO_2 Using a Non-Hydrolytic Solution-Phase Route: Ligand Exchange as a Means of Controlling Particle Size. *Chem. Sci.* **2016**, *7*, 4930–4939.

(8) Korthuis, V.; Khosrovani, N.; Sleight, A. W.; Roberts, N.; Dupree, R.; Warren, W. W. Negative Thermal Expansion and Phase Transitions in the $ZrV_{2-x}P_xO_7$ Series. *Chem. Mater.* **1995**, *7*, 412–417.

(9) Evans, J. S. O. Negative Thermal Expansion Materials. *J. Chem Soc., Dalt. Trans.*, **1999**, 3317–3326.

(10) Barrera, G. D.; Bruno, J. A. O.; Barron, T. H. K.; Allan, N. L. Negative Thermal Expansion. *J. Phys. Condens. Matter* **2005**, *17*, R217–R252.

(11) Zhu, J.; Zhou, Y.; Wang, B.; Zheng, J.; Ji, S.; Yao, H.; Luo, H.; Jin, P. Vanadium Dioxide Nanoparticle-Based Thermochromic Smart Coating: High Luminous Transmittance, Excellent Solar Regulation Efficiency, and Near Room Temperature Phase Transition. *ACS Appl. Mater. Interfaces* **2015**, *7*, 27796–27803.

(12) Liu, C.; Balin, I.; Magdassi, S.; Abdulhalim, I.; Long, Y. Vanadium Dioxide Nanogrid Films for High Transparency Smart Architectural Window Applications. *Opt. Express* **2015**, *23*, A124.

(13) He, W.; Zhang, L.; Chan, D. S. H.; Cho, B. J. Cubic-Structured HfO_2 with Optimized Doping of Lanthanum for Higher Dielectric Constant. *IEEE Electron Device Lett.* **2009**, *30*, 623–625.

(14) Debernardi, A. Ab Initio Study of Structural, Vibrational and Dielectric Properties of High-κ HfO_2 as a Function of Doping. *IOP Conf. Ser. Mater. Sci. Eng.* **2010**, *8*, 012021.

(15) Turquat, C.; Leroux, C.; Roubin, M.; Nihoul, G. Vanadium-Doped Elaboration and Structural Hafnia: Elaboration and Structural Characterization. *Solid State Sci* **1999**, *1*, 3–13.

(16) Buchanan, D. A.; Lo, S. H. Growth, Characterization and the Limits of Ultrathin SiO_2 Based Dielectrics for Future CMOS Applications. in *The Physics and Chemistry of SiO_2 and the Si-SiO_2 Interface-3, Electrochemical Society Meeting Proceedings*, Massoud, H.; Poindexter, E.; Helms, C. Pennington, NJ: The Electrochemical Society, **1996**, vol. 96-1, pp. 1-14.

(17) Huang, L.; Liu, S.; Van Tassell, B. J.; Liu, X.; Byro, A.; Zhang, H.; Leland, E. S.; Akins, D. L.; Steingart, D. A.; Li, J.; O'Brien, S. Erratum: Structure and Performance of Dielectric Films Based on Self-Assembled Nanocrystals with a High Dielectric Constant.

Nanotechnology **2013**, *24*, 499601.

(18) Verkhoturov, S. V.; Eller, M. J.; Rickman, R. D.; Della-Negra, S.; Schweikert, E. A. Single Impacts of C60 on Solids: Emission of Electrons, Ions and Prospects for Surface Mapping. *J. Phys. Chem. C* **2010**, *114*, 5637–5644.

(19) Eller, M. J.; Verkhoturov, S. V.; Della-Negra, S.; Schweikert, E. A. SIMS Instrumentation and Methodology for Mapping of Co-Localized Molecules. *Rev. Sci. Instrum.* **2013**, *84*, 103706.

(20) Eller, M. J.; Verkhoturov, S. V.; Schweikert, E. A. Testing Molecular Homogeneity at the Nanoscale with Massive Cluster Secondary Ion Mass Spectrometry. *Anal. Chem.* **2016**, *88*, 7639–7646.

APPENDIX A

SUPPLEMENTARY FIGURES AND TABLES

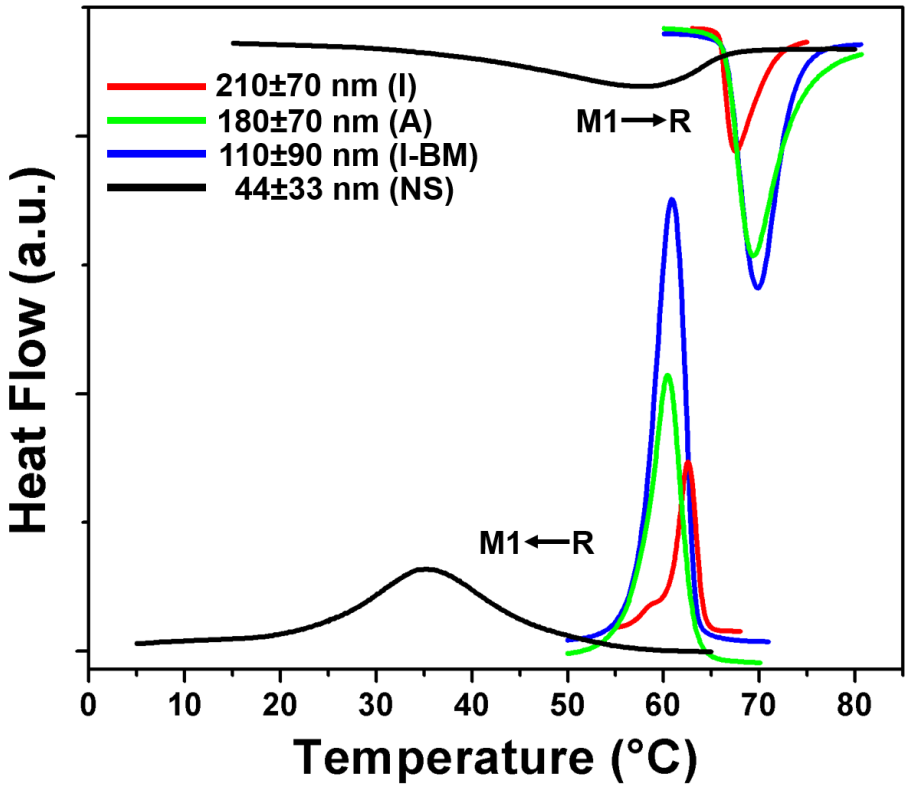

Figure A. 1 Differential scanning calorimetry (DSC) traces acquired for each set of particle sizes. Nanowires >100 nm (I, A, I-BM) show a M1 to R transition at ca. 66-70°C, whereas the NS sample transitions at ca. 57°C. The R to M1 cooling transition of the I, A, I-BM samples is at ca. 60°C, whereas the transition for NS particles is at ca. 36°C.

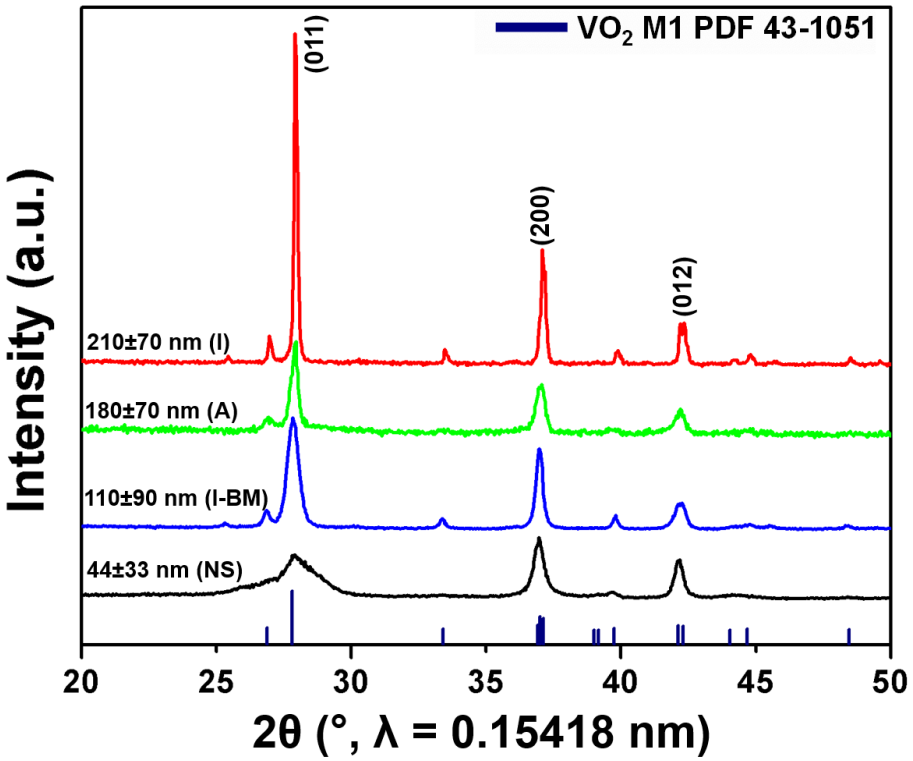

Figure A. 2 Powder X-ray diffraction patterns of VO_2 nanocrystals of varying sizes. Scherrer broadening is apparent below an average crystal size of ca. 100 nm.

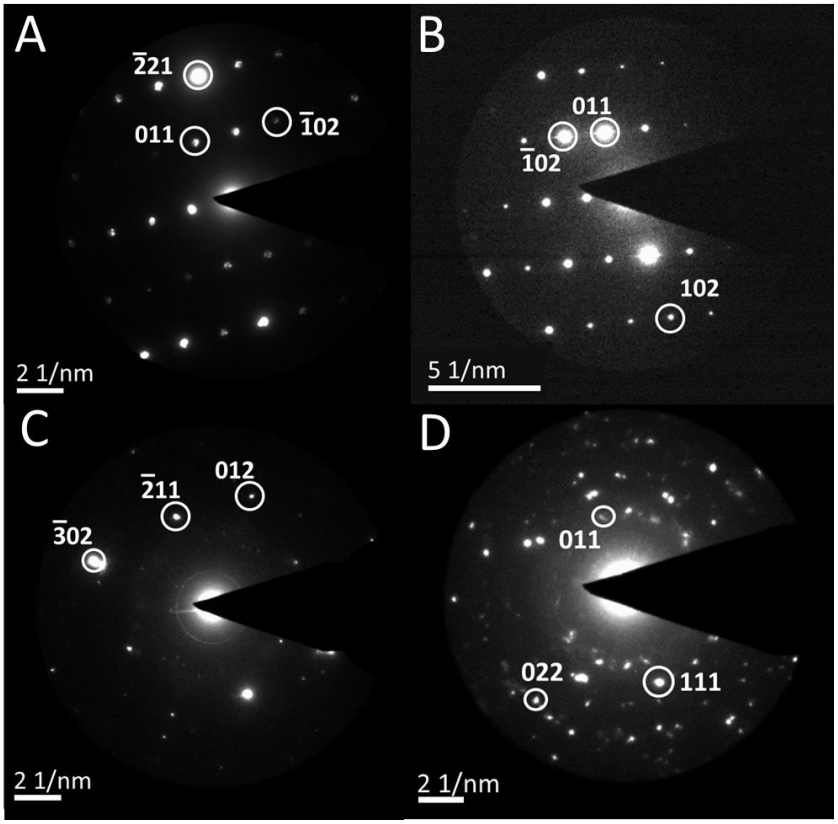

Figure A. 3 Selected area electron diffraction (SAED) patterns acquired for nanostructures examined in this study. A) VO_2 nanowires prepared via reduction of V_2O_5 using 2-propanol (Sample I). B) VO_2 nanowires prepared by reduction of V_2O_5 using acetone (Sample A) C) VO_2 nanoparticles produced by 2-propanol reduction of V_2O_5 followed by 2.5 h dry milling with methacrylate polymer beads (Sample I-BM). D) VO_2 NS produced by reduction and precipitation using a soluble ammonium metavanadate precursor (Sample NS). The diffraction patterns are entirely consistent with a phase assignment to the M1 monoclinic phase of VO_2.

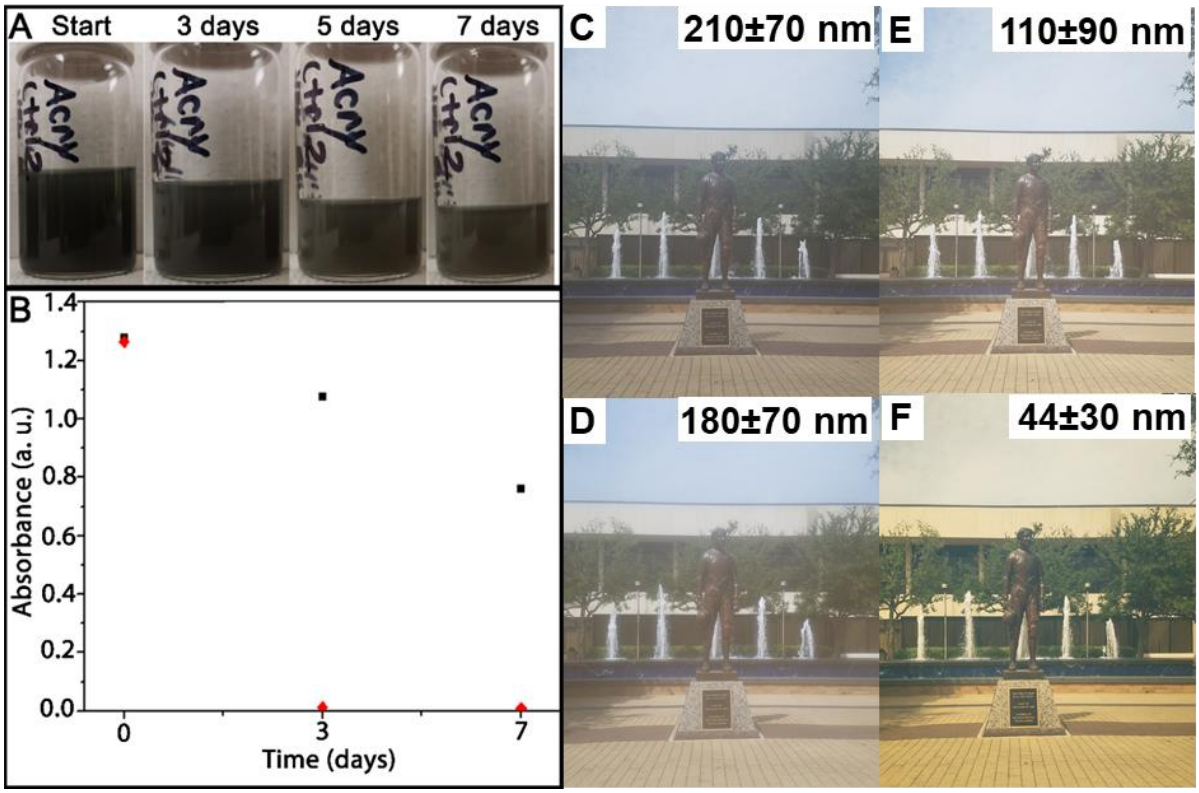

Figure A. 4 A) Digital photograph of aqueous dispersions of VO_2@SiO_2 nanocrystals dispersed in methacrylic acid/ethyl acrylate (MAA/EA) copolymer; B) Sedimentation plot of ball-milled VO_2@SiO_2 nanowires dispersed in deionized water (red diamonds) and in deionized water with the addition of 1 wt.% MAA/EA copolymer (black squares); dispersion concentrations correspond to 0.6 mg VO_2@SiO_2/mL. Panels C-F depict digital photographs acquired through films cast onto glass from dispersions with concentrations of 0.6 mg VO_2@SiO_2/mL with a dry thickness of 1—2 μm. C) Transparency of a film cast from MAA/EA and VO_2@SiO_2 dispersion with Sample I nanowires with a width of 210±70 nm. D) Transparency of a film cast from MAA/EA and VO_2@SiO_2 dispersion with Sample A nanowires with a width of 180±70 nm. E) Transparency of a film cast from MAA/EA and VO_2@SiO_2 dispersion with Sample I-BM nanowires. Particle widths were 110±90 nm. F) Transparency of a film cast from MAA/EA and VO_2@SiO_2 dispersion with VO_2 NS with a size range of 44±30 nm.

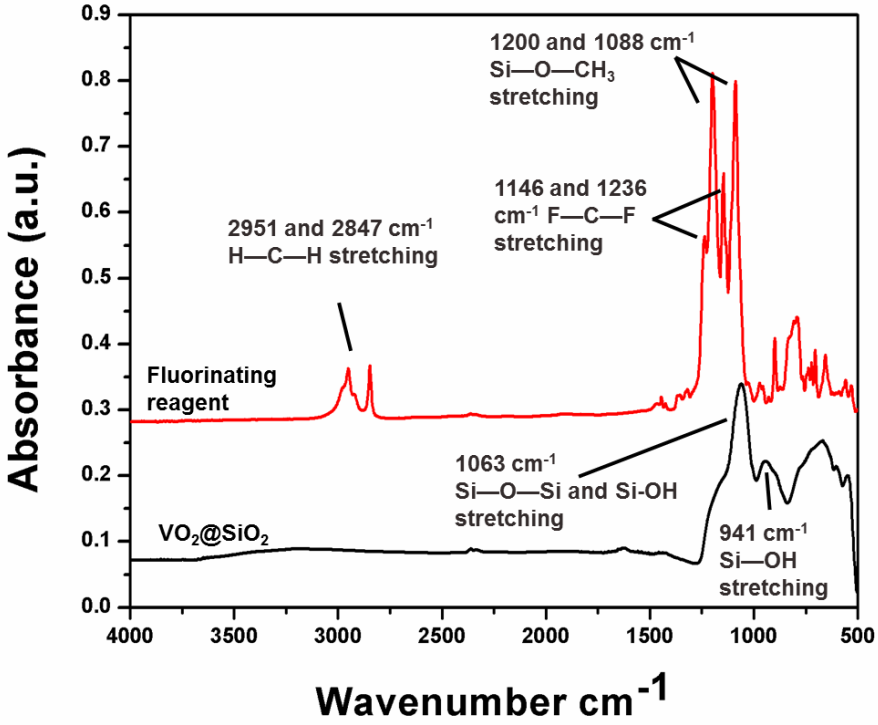

Figure A. 5 FTIR spectra of the fluorinating reagent (heptadecafluoro-1,1,2,2-tetrahydrodecyl)trimethoxysilane) and core—shell VO_2@SiO_2. The spectrum for VO_2@SiO_2 is characterized by infrared-active modes at 1063 and 941 cm^{-1} that correspond to Si—O—Si and Si—OH stretches, respectively.

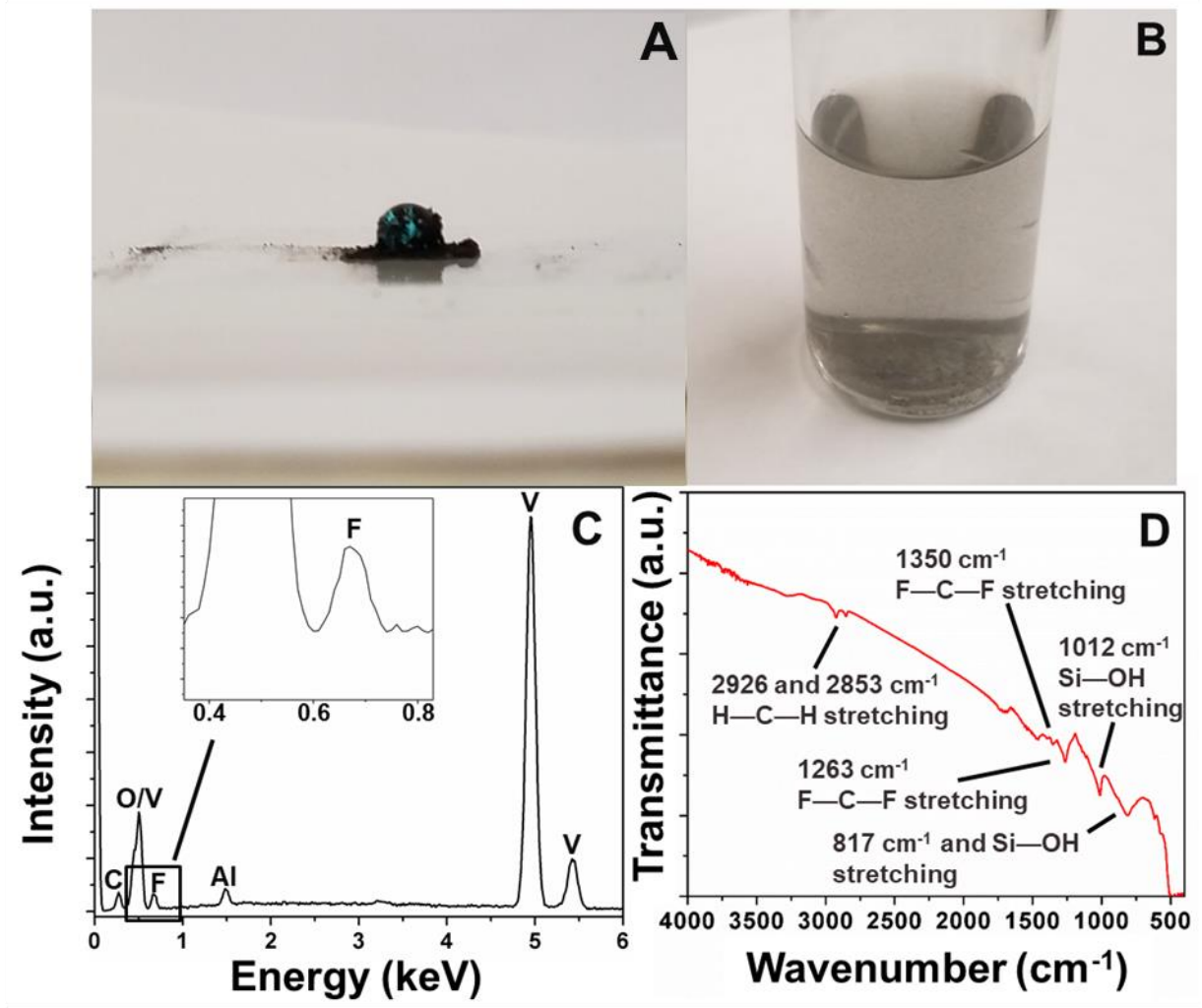

Figure A. 6 A) Digital photograph showing the interaction of a water droplet with VO_2@-F nanocrystals; functionalization with a perfluorinated silane renders the surface hydrophobic, although not to the same extent as fluorinated VO_2@SiO_2-F core—shell nanocrystals. B.) VO_2@-F nanocrystals are readily dispersible in a perfluorinated solvent. C) EDX spectrum acquired for VO_2@-F nanocrystals. It is worth noting that the Si peak is too small to resolve in this sample which was not coated in SiO_2 prior to functionalization. D) FTIR ATR spectrum of VO_2 nanowires functionalized with trimethoxy(1H,1H,2H,2H-perfluorooctyl)silane showing characteristic modes of the perfluorinated moieties as assigned in the discussion.

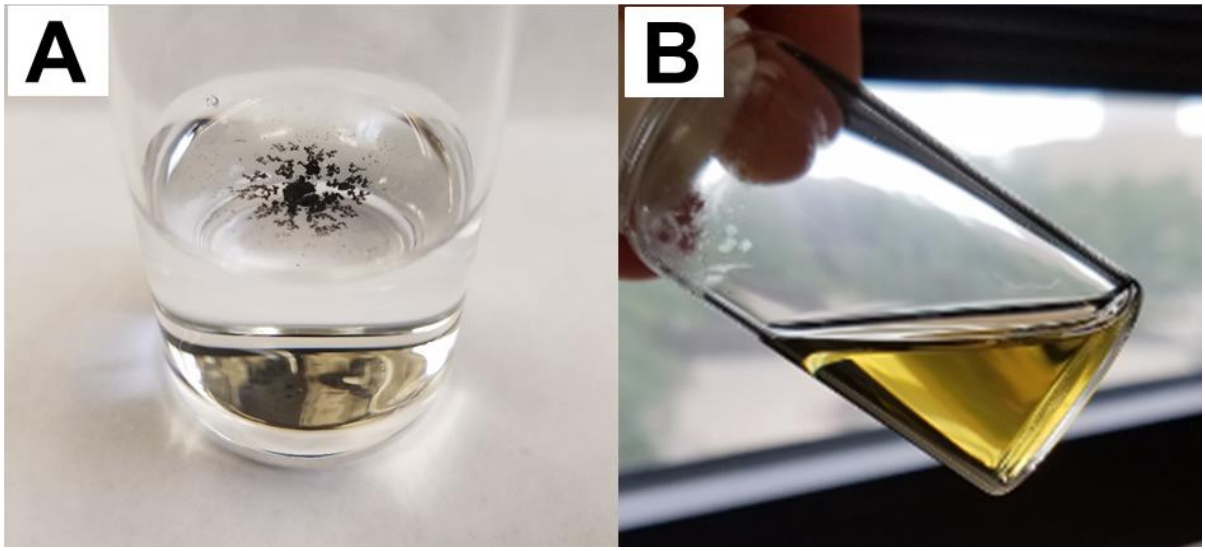

Figure A. 7 A) Digital photograph of VO_2@-F nanocrystals in water indicating their water repellency as a result of the pendant perfluorinated chains. B) An aqueous dispersion of 0.04 mg/mL VO_2@-F with 1.5 x 10^{-3} M PFOS depicting stabilization of a homogenous and stable colloidal dispersion.

Figure A. 8 Digital photographs acquired with illumination through solution-cast nanocomposite VO_2 thin films. A) A crosslinked polyacrylic acid is used as the thickener with a 6 mg loading of VO_2 nanocrystals. B) Methacrylic acid/ethyl acrylate copolymer is used as the matrix with a 6 mg loading of VO_2 nanocrystals. The polymer matrix exhibits significantly decreased scattering. C) Methacrylic acid/ethyl acrylate copolymer with a 6 mg loading VO_2@-F nanocrystals with PFOS as a surfactant. The scattering of visible light has been further reduced. D) Uncoated borosilicate glass slide.

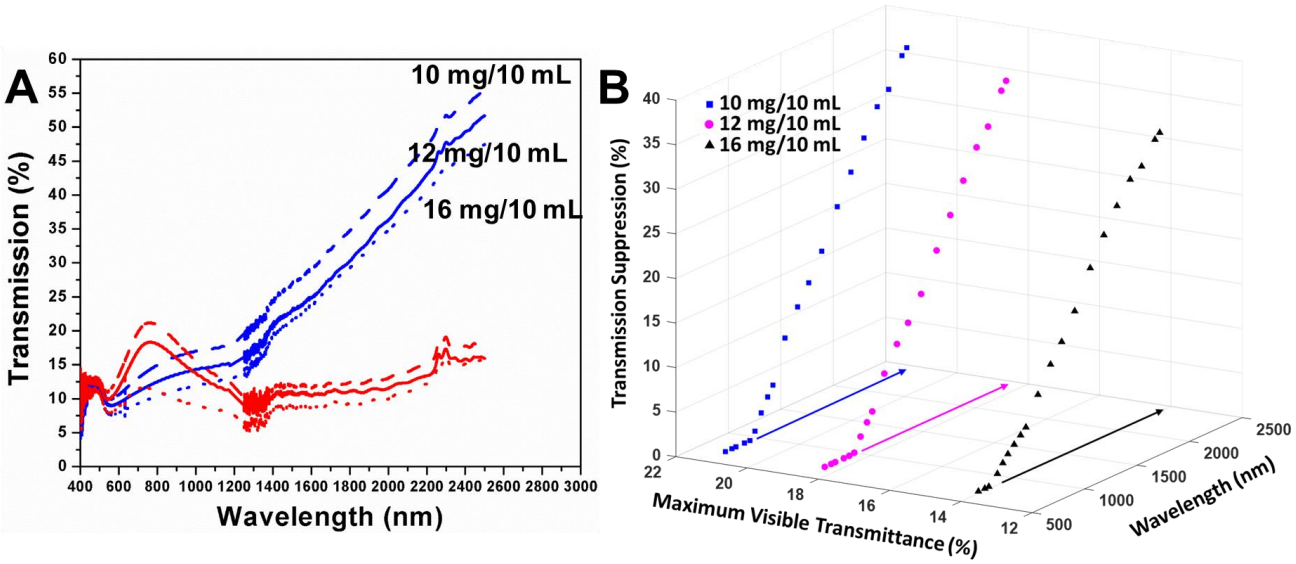

Figure A. 9: A) Absorption spectra acquired for three higher loadings of VO_2 nanocrystals. The plots correspond to 10 mg (dashed lines), 12 mg (solid lines), and 16 mg (dotted lines) dispersed in 10 mL of an aqueous dispersion of 1 wt.% (relative to 10 mL volume of water) methacrylic acid/ethyl acrylate copolymer cast onto borosilicate glass substrates. Spectra obtained at 30°C are displayed in blue, whereas spectra obtained at 85°C after equilibration for 10 min are shown in red. B) 3D representation of VO_2 optical data plots showing three nanocrystal loadings: 10 mg (blue squares), 12 mg (purple circles), and 16 mg (black triangles). Maximum visible transmission is the maxima in the visible region from each 85°C plot in A and is constant for each plot in B (represented by an arrow across the maximum visible transmittance/wavelength plane).

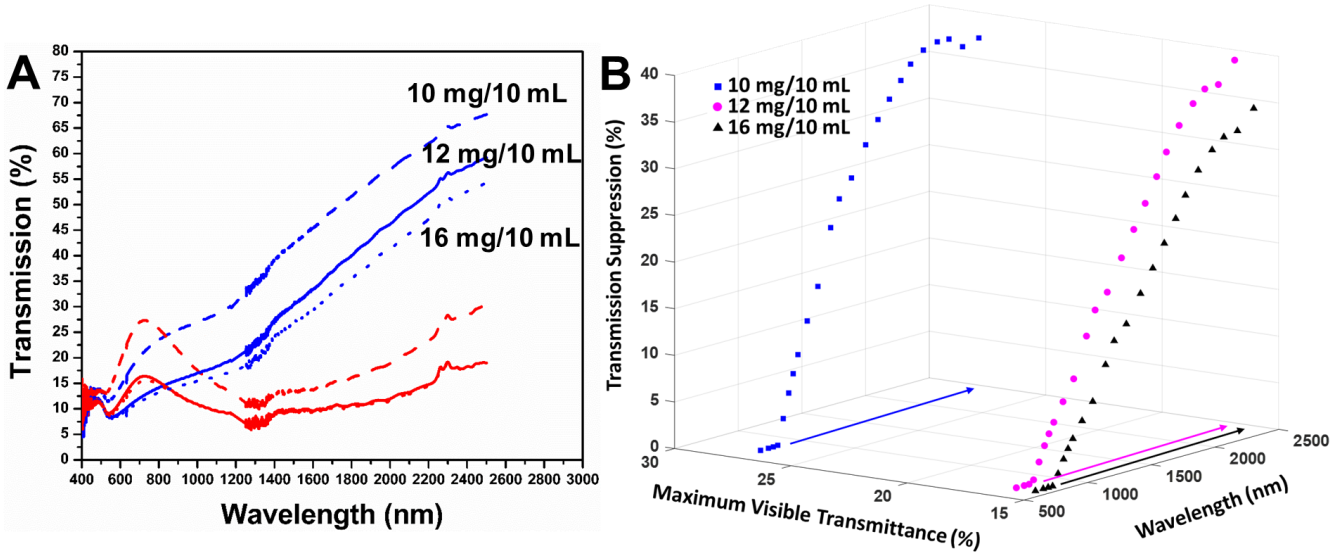

Figure A. 10 A) Absorption spectra acquired for three higher loadings of VO_2@-F nanocrystals. The plots correspond to 10 mg (dashed lines), 12 mg (solid lines), and 16 mg (dotted lines) dispersed in 10 mL of an aqueous dispersion of 1 wt.% (relative to 10 mL volume of water) methacrylic acid/ethyl acrylate copolymer cast onto borosilicate glass substrates. Spectra obtained at 30°C are displayed in blue, whereas spectra obtained at 85°C after equilibration for 10 min are shown in red. B) 3D representation of VO_2 optical data plots showing three nanocrystal loadings: 10 mg (blue squares), 12 mg (purple circles), and 16 mg (black triangles). Maximum visible transmission is the maxima in the visible region from each 85°C plot in A and is constant for each plot in B (represented by an arrow across the maximum visible transmittance/wavelength plane).

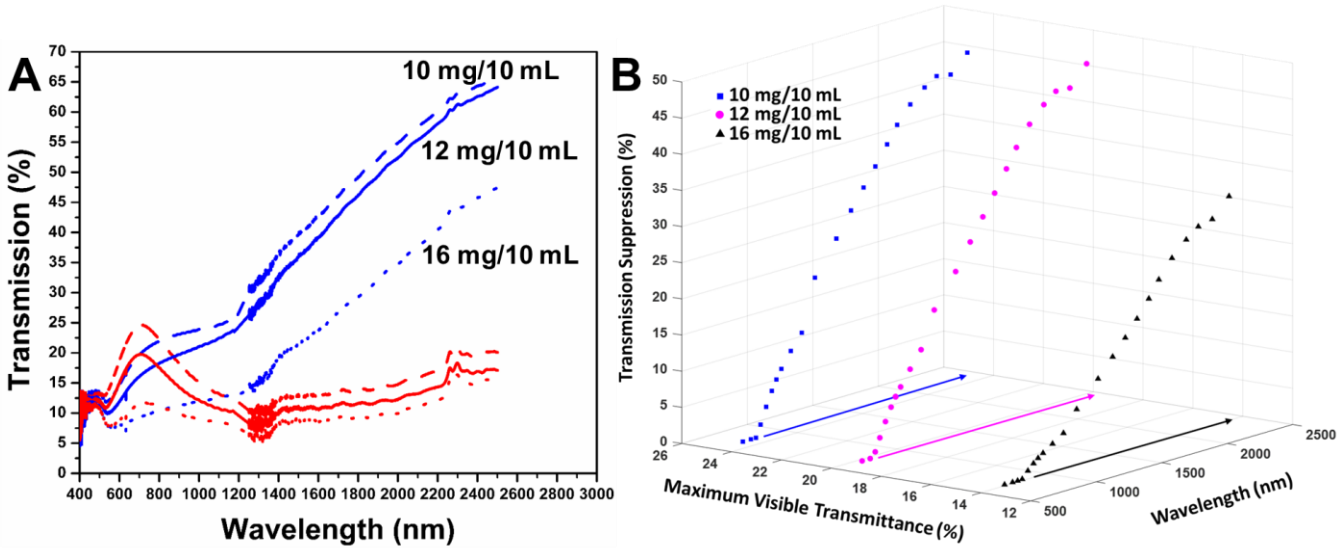

Figure A. 11 A) Absorption spectra acquired for three higher loadings of VO_2@SiO_2 nanocrystals. The plots correspond to 10 mg (dashed lines), 12 mg (solid lines), and 16 mg (dotted lines) dispersed in 10 mL of an aqueous dispersion of 1 wt.% (relative to 10 mL volume of water) methacrylic acid/ethyl acrylate copolymer cast onto borosilicate glass substrates. Spectra obtained at 30°C are displayed in blue, whereas spectra obtained at 85°C after equilibration for 10 min are shown in red. B) 3D representation of VO_2 optical data plots showing three nanocrystal loadings: 10 mg (blue squares), 12 mg (purple circles), and 16 mg (black triangles). Maximum visible transmission is the maxima in the visible region from each 85°C plot in A and is constant for each plot in B (represented by an arrow across the maximum visible transmittance/wavelength plane).

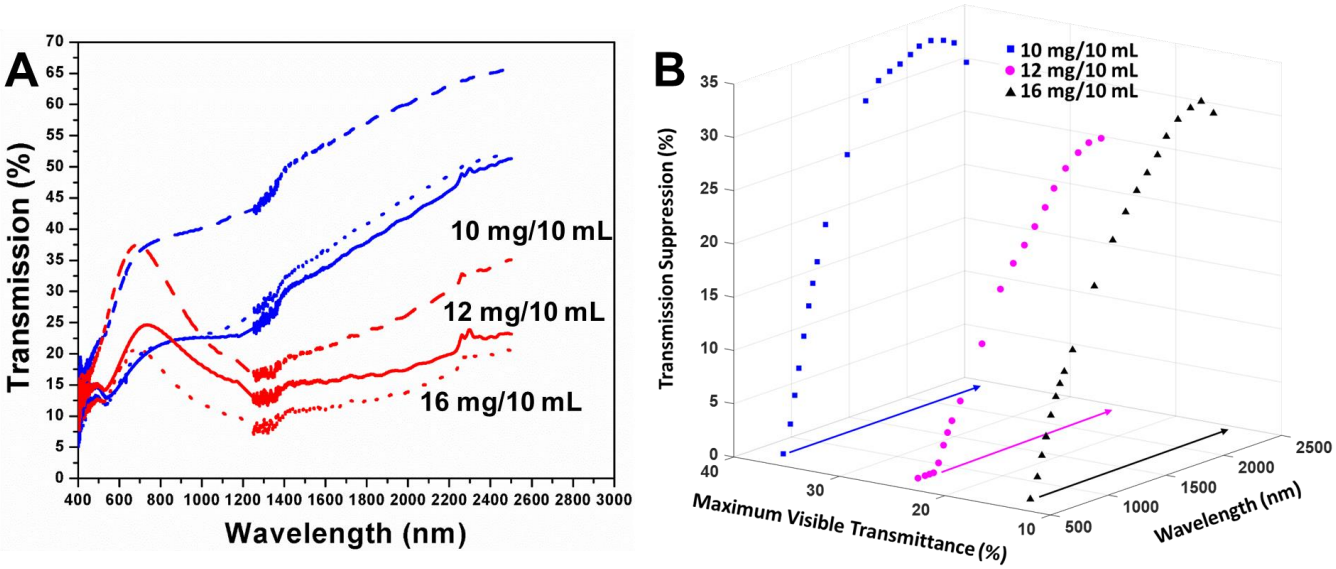

Figure A. 12 A) Absorption spectra acquired for three higher loadings of VO_2@SiO_2-F nanocrystals. The plots correspond to 10 mg (dashed lines), 12 mg (solid lines), and 16 mg (dotted lines) dispersed in 10 mL of an aqueous dispersion of 1 wt.% (relative to 10 mL volume of water) methacrylic acid/ethyl acrylate copolymer cast onto borosilicate glass substrates. Spectra obtained at 30°C are displayed in blue, whereas spectra obtained at 85°C after equilibration for 10 min are shown in red. B) 3D representation of VO_2 optical data plots showing three nanocrystal loadings: 10 mg (blue squares), 12 mg (purple circles), and 16 mg (black triangles). Maximum visible transmission is the maxima in the visible region from each 85°C plot in A and is constant for each plot in B (represented by an arrow across the maximum visible transmittance/wavelength plane).

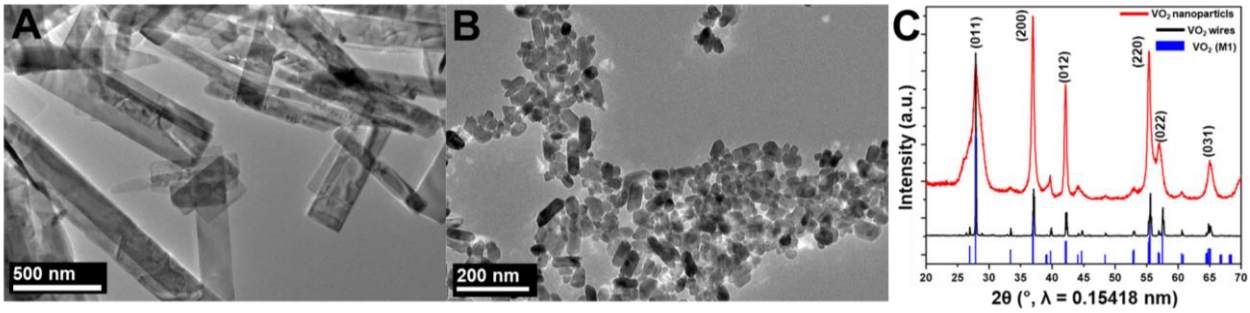

Figure A. 13 Characterization of VO_2 nanocrystals. TEM images of A) VO_2 nanowires prepared from the hydrothermal reduction of V_2O_5 by acetone and B) quasi-spherical VO_2 nanocrystals prepared by sol—gel condensation and hydrothermal treatment C) Powder XRD patterns of VO_2 nanowires (black) and ultrasmall VO_2 nanocrystals (red). The tick marks denote the reflections of the M1 phase of VO_2 (PDF: 43-1051).

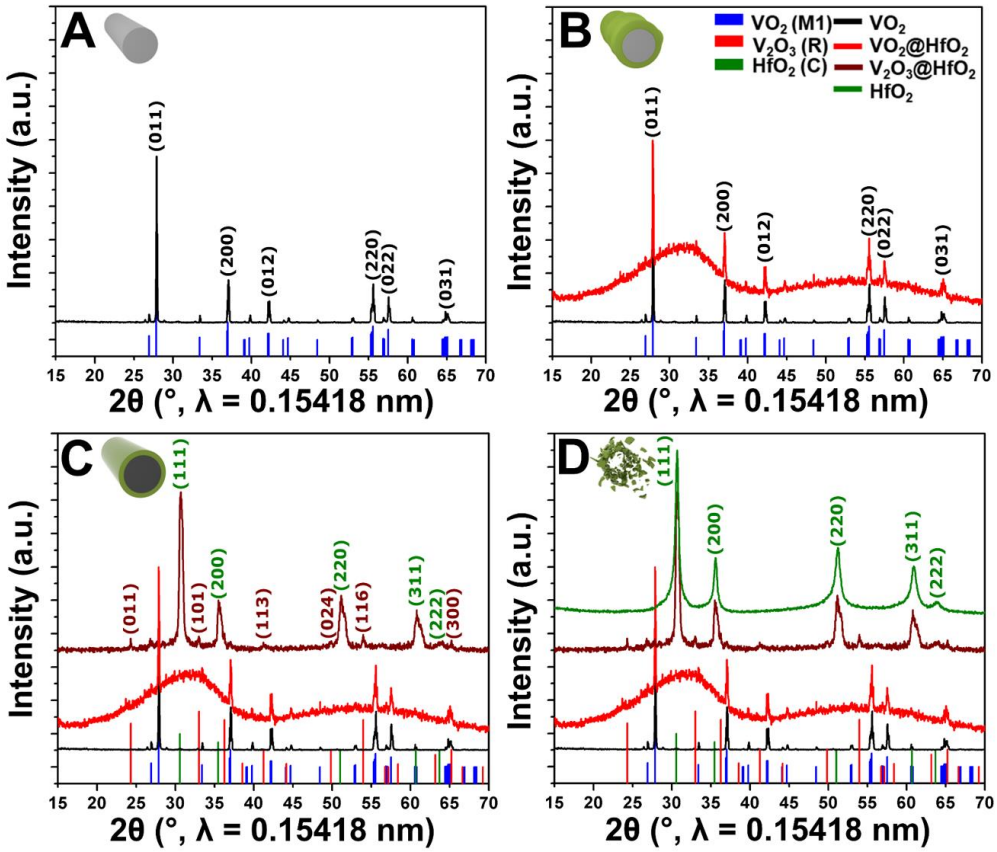

Figure A. 14 Indexed powder XRD patterns acquired at room temperature along the synthetic pathway. A) XRD pattern of VO_2 nanowires prepared by acetone reduction of V_2O_5 (black). B) XRD pattern of VO_2 nanowires coated with amorphous HfO_2 shell (red). The diffuse scattering background derived from amorphous HfO_2 is apparent. C) Powder XRD pattern acquired subsequent to annealing showing the presence of rhombohedral V_2O_3 and cubic HfO_2 (maroon). D) Powder XRD pattern after acid etching indicating the presence of cubic HfO_2 (green). An indexing and pattern legend is shown in the top right of panel B. The XRD patterns are indexed to the following phases: VO_2 (M1) = 43-1051 and V_2O_3 (R) = 85-1411.

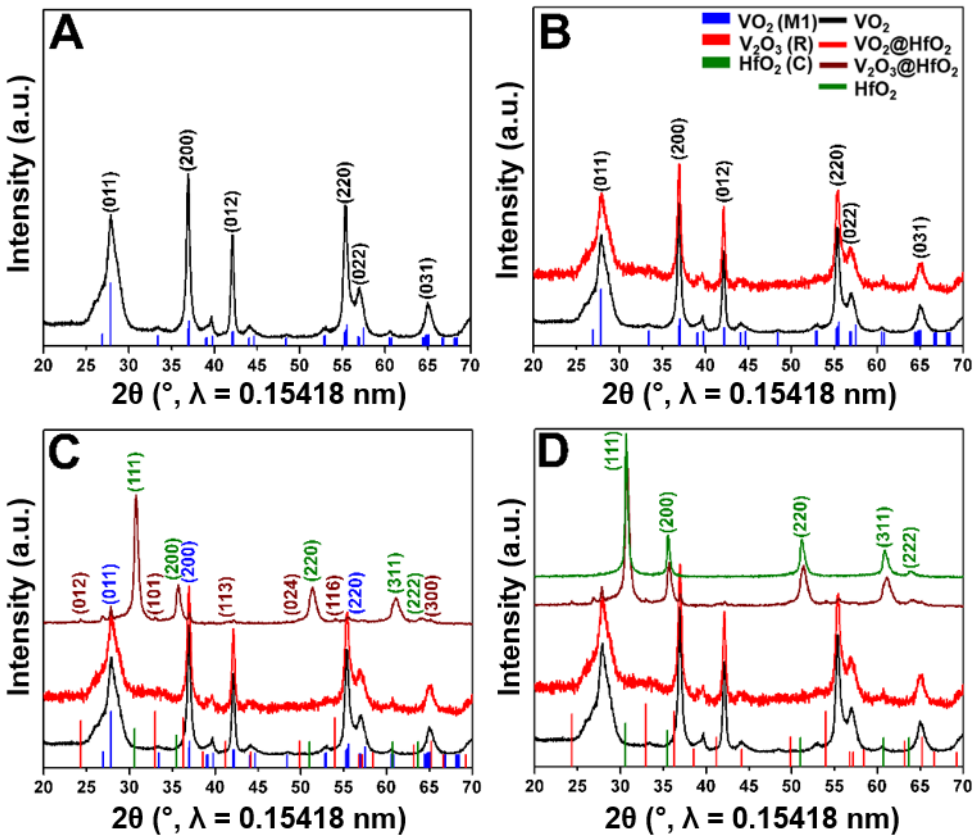

Figure A. 15 Indexed powder XRD patterns acquired at room temperature along the synthetic pathway. A) XRD pattern of VO_2 quasi-spherical nanocrystals prepared by sol—gel condensation and hydrothermal treatment (black). B) XRD pattern of VO_2 quasi-spherical nanocrystals coated with amorphous HfO_2 shell (red). The diffuse scattering background derived from amorphous HfO_2 is apparent. C) Powder XRD pattern acquired subsequent to annealing showing the presence of rhombohedral V_2O_3 and cubic HfO_2 (maroon). D) Powder XRD pattern after acid etching indicating the presence of cubic HfO_2 (green). An indexing and pattern legend is shown in the top right of panel B. The XRD patterns are indexed to the following phases: VO_2 (M1) = 43-1051 and V_2O_3 (R) = 85-1411.

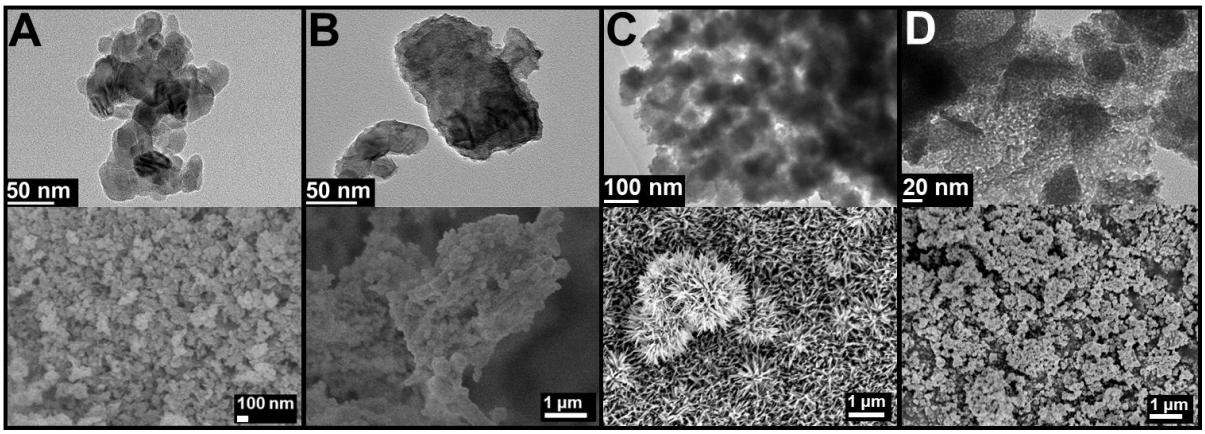

Figure A. 16 TEM and SEM images corresponding to synthetic steps involved in the stabilization of cubic HfO_2. A) TEM image (top) and SEM image (bottom) of M1-phase VO_2 quasi-spherical nanocrystals prepared by the sol—gel condensation and hydrothermal method. B) TEM and SEM images of VO_2 quasi-spherical nanocrystals coated with an amorphous HfO_2 shell. C) TEM and SEM images of V_2O_3@cubic-HfO_2 core—shell structures obtained upon annealing VO_2@amorphous-HfO_2 structures at 650°C. D) TEM and SEM image of cubic HfO_2 after acid etching of the V_2O_3 core.

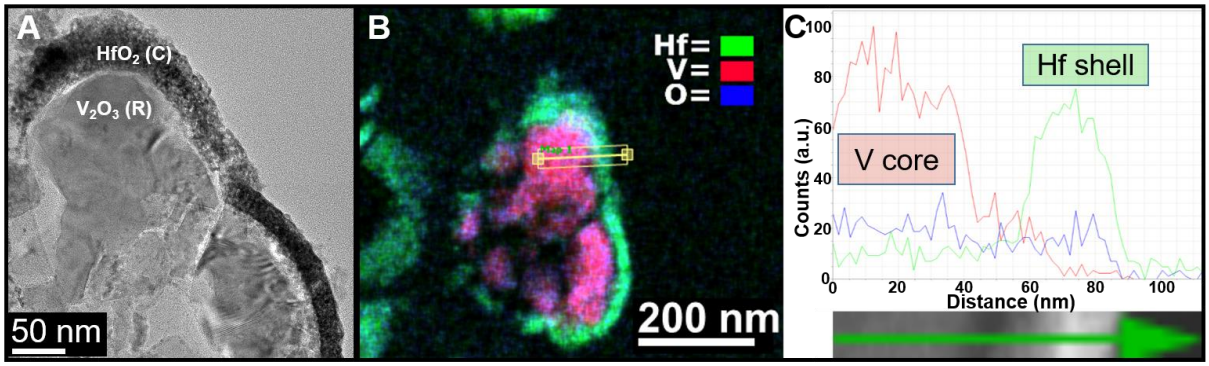

Figure A. 17 Cross-sectional TEM image and EDX line scan of an ultramicrotomed V_2O_3@HfO_2 core—shell nanowire. A) Cross-sectional TEM image of a V_2O_3@HfO_2 core—shell nanowire; B) corresponding EDX map of the V_2O_3@HfO_2 nanowire; and C) EDX line scan along the arrow in panel B. The vanadium signal (red) is highly concentrated within the core, whereas the Hf (green) signal derives predominantly from shell with oxygen (blue) distributed throughout the nanowire.

Table A. 1: Summary of maximum NIR modulation, transmission in the visible region, and onset of NIR modulation for each of the three nanocrystal loadings in Figure A. 9.

Sample: VO_2 /Nanocrystal Loading	Maximum NIR Modulation (%)	Maximum Transmittance in the Visible Spectrum (%)	Onset of NIR Modulation (nm)
10 mg	37.5	21.2	958
12 mg	35.7	18.4	978
16 mg	31.9	14.1	832

Table A. 2: Summary of maximum NIR modulation, transmission in the visible region, and onset of NIR modulation for each of the three nanocrystal loadings in Figure A. 10.

Sample: VO_2@-F/ Nanocrystal Loading	Maximum NIR Modulation (%)	Maximum Transmittance in the Visible Spectrum (%)	Onset of NIR Modulation (nm)
10 mg	38.6	27.4	835
12 mg	40.2	16.4	827
16 mg	35.1	15.6	845

Table A. 3 Summary of maximum NIR modulation, transmission in the visible region, and onset of NIR modulation for each of the three nanocrystal loadings in Figure A. 11.

Sample: VO_2@SiO_2 /Nanocrystal Loading	Maximum NIR Modulation (%)	Maximum Transmittance in the Visible Spectrum (%)	Onset of NIR Modulation (nm)
10 mg	45.7	24.6	805
12 mg	47.0	19.8	786
16 mg	31.9	14.1	832

Table A. 4: Summary of maximum NIR modulation, transmission in the visible region, and onset of NIR modulation for each of the nanocrystal loadings in Figure A. 12.

Sample: VO_2@SiO_2-F /Nanocrystal Loading	Maximum NIR Modulation (%)	Maximum Transmittance in the Visible Spectrum (%)	Onset of NIR Modulation (nm)
10 mg	34.1	37.5	720
12 mg	28.2	24.7	858
16 mg	32.3	20.8	722

Table A. 5 Rietveld refined values of HfO_2 (C). Also shown are fit quality statistics. Such as the goodness of fit (X^2), the weighted goodness of fit (wRp) and individual point residuals (Rp). These values demonstrate the high degree of agreement when comparing calculated and observed patterns.

HfO_2 (C) // a/b/c = 5.04793(22) Å // Space Group = $Fm\bar{3}m$ // $\alpha/\beta/\gamma = 90.0°$ // Vol. = 128.629(16) $Å^3$						
$X^2 = 4.712$		wRp = 6.68%		Rp = 5.08%		
Atom Label	Position	Mult.	*x*	*y*	*z*	Occupancy
Hf	a	4	0.00(0)	0.00(0)	0.00(0)	1.000(0)
O	c	8	0.25(0)	0.25(0)	0.25(0)	1.000(0)